

2017

Novel biomarker assays based on photothermal effects and nanophotonics

Yunfei Zhao
Iowa State University

Follow this and additional works at: <https://lib.dr.iastate.edu/etd>

 Part of the [Electrical and Electronics Commons](#), [Materials Science and Engineering Commons](#), [Mechanics of Materials Commons](#), and the [Optics Commons](#)

Recommended Citation

Zhao, Yunfei, "Novel biomarker assays based on photothermal effects and nanophotonics" (2017). *Graduate Theses and Dissertations*. 15477.
<https://lib.dr.iastate.edu/etd/15477>

This Dissertation is brought to you for free and open access by the Iowa State University Capstones, Theses and Dissertations at Iowa State University Digital Repository. It has been accepted for inclusion in Graduate Theses and Dissertations by an authorized administrator of Iowa State University Digital Repository. For more information, please contact digirep@iastate.edu.

Novel biomarker assays based on photothermal effects and nanophotonics

by

Yunfei Zhao

A dissertation submitted to the graduate faculty
in partial fulfillment of the requirements for the degree of

DOCTOR OF PHILOSOPHY

Major: Electrical Engineering

Program of Study Committee:

Meng Lu, Major Professor

Liang Dong

Santosh Pandey

Xinwei Wang

Jonathan Claussen

Xiaoli Tan

The student author and the program of study committee are solely responsible for the content of this dissertation. The Graduate College will ensure this dissertation is globally accessible and will not permit alterations after a degree is conferred.

Iowa State University

Ames, Iowa

2017

Copyright © Yunfei Zhao, 2017. All rights reserved.

TABLE OF CONTENTS

LIST OF FIGURES	iii
NOMENCLATURE	v
ABSTRACT.....	vii
CHAPTER 1. INTRODUCTION	1
1.1 Immunoassays and Biomarker Detection	3
1.1.1 Immunoassays and ELISA.....	3
1.1.2 Lateral flow assay	7
1.2 Photothermal Effects and Their Applications.....	10
1.2.1 Photoacoustic effect.....	10
1.2.2 Photothermal lens effect	12
1.3 Plasmonics and Photonic Crystals	15
1.3.1 Plasmonic nanoparticles.....	15
1.3.2 Synthesis of gold nanoparticles	18
1.3.3 Heat generation of nanoparticles	19
1.3.4 Photonic crystal.....	24
1.4 Acknowledgment	27
CHAPTER 2. PHOTOACOUSTIC IMMUNOASSAY	28
2.1 Principle of Photoacoustic Immunoassay	28
2.2 Simulation of Gold Nanoparticles	30
3.2.1 Plasmonic resonance of gold nanoparticles	30
3.2.2 Heat generation of gold nanoparticles	33
2.3 Instrumentation	36
2.4 Assay Protocols.....	37
2.5 Photoacoustic Detection of Protein.....	39
2.6 Photoacoustic Immunoassay of Protein Biomarker	43
2.7 Acknowledgment	46
CHAPTER 3. PHOTOACOUSTIC LATERAL FLOW ASSAY.....	47
3.1 Principle of Lateral Flow Assay	47
3.2 Development of Photoacoustic Detection Modality for LFA.....	48
3.3 Photoacoustic measurement of AuNPs on a Porous Substrate	54
3.4 Photoacoustic LFA Detection of Infectious Disease Biomarker	56
3.5 Acknowledgment	64

CHAPTER 4. PHOTONIC CRYSTAL ENHANCEMENT OF PA DETECTION.....	65
4.1 Structure of PC Substrates	65
4.2 FDTD Simulation of Near Field Distribution of AuNPs on PC	66
4.3 Instrumentation for PC Enhanced PA Measurement	68
4.4 Characteristics of PC Enhanced PA Detection	69
4.5 PC Enhanced PA Detection of an Absorbing Dye and AuNPs	71
4.6 Acknowledgment	74
CHAPTER 5. PHOTONIC CRYSTAL ENHANCED PHOTOTHERMAL LENS.....	75
5.1 Principle of PC-enhanced PTL	75
5.2 Characteristics of PC Enhancement.....	78
5.3 PTL Measurement of an Absorbing Dye	80
5.4 PTL Measurement of AuNPs.....	81
5.5 Acknowledgment	83
CHAPTER 6. CONCLUSIONS	85
REFERENCES	86
ACKNOWLEDGMENTS	98

LIST OF FIGURES

Figure 1	Colorimetric ELISA performed in 96-well microtiter plate	4
Figure 2	The assay protocol of sandwich ELISA.....	5
Figure 3	Structure of an LFA paper strip	8
Figure 4	Illustration for plasmonic resonance	16
Figure 5	Calculated rate of heat generation of Ag, Au, CdSe and CdTe NPs	23
Figure 6	Calculated temperature increase at the surface of a single Au NP in water as a function of illumination power at the plasmon resonance	24
Figure 7	Guided-mode resonance.....	26
Figure 8	PA immunoassay format.....	29
Figure 9	Optical setup for PA measurement	29
Figure 10	FDTD Simulated absorption spectrum of the AuNP	32
Figure 11	FDTD Simulated near field distribution of the AuNP	32
Figure 12	Temperature distribution of an AuNP under illumination of EM radiation.....	35
Figure 13	Optical setup for a PA immunoassay.....	36
Figure 14	ELISA and PA immunoassay protocols	39
Figure 15	PA signal plotted with respect to AuNP concentration	40
Figure 16	Schematic representation of the SA-measurement assay.....	42
Figure 17	PA signal plotted against the SA concentration.....	42
Figure 18	Colorimetric measurement results of the ELISA test for human IL-8	44
Figure 19	IL-8 titration curve generated using the PA immunoassay.....	44

Figure 20	PA LFA working principle	51
Figure 21	Optical setup for chop mode PA measurement.....	51
Figure 22	Optical setup for scan mode PA measurement	51
Figure 23	PA waveforms for AuNPs absorbed in a porous substrate measured using chop mode	53
Figure 24	PA waveforms for AuNPs absorbed in a porous substrate measured using scan mode.....	53
Figure 25	Comparison between PA-based detection methods and colorimetric analysis for AuNPs on porous substrates	56
Figure 26	Photos of the LFA paper strip with 4 different analyte concentrations ...	58
Figure 27	Dose response curves for the chop mode, scan mode, and scattering intensity measurements.....	60
Figure 28	Effects of laser output on the PA signal of the LFA samples.....	62
Figure 29	Effects of laser wavelength on the PA signal of the LFA samples.....	62
Figure 30	Cross-sectional view of a 1-D PC.....	65
Figure 31	FDTD simulation of the enhancement effect of a PC substrate on AuNPs dispersed on its surface	67
Figure 32	Calculated absorption spectra of AuNPs on acrylic and PC substrates.....	67
Figure 33	Optical setup for PC enhanced PA measurement	69
Figure 34	Incident angle dependence of the PA signals of organic dye Epolight 5262	70
Figure 35	Incident angle dependence of the PA signals of AuNPs.....	70

Figure 36 Enhancement of PA signals of an absorbing dye by GMR of PC substrates	72
Figure 37 Enhancement of PA signals of AuNPs by GMR of PC substrates	73
Figure 38 Schematic plot for PC enhanced PTL measurement.....	76
Figure 39 Characterizations of the PC sample	77
Figure 40 Photographs of the reflected probe beam.	79
Figure 41 Transmission of the probe laser through the PC substrate and the PTL signals.....	79
Figure 42 PTL measurement of light absorbing dye.....	81
Figure 43 SEM images of AuNPs dispersed on PC surfaces at three different concentrations	82
Figure 44 PTL signals of AuNPs plotted as a function of the AuNP concentration.....	82

NOMENCLATURE

1-D	One-dimensional
AuNP	Gold Nanoparticle
CCD	Charge Coupled Device
CMOS	Complementary Metal-Oxide-Semiconductor
CrAg	Cryptococcal Antigen
CT	Computed Tomography
ELISA	Enzyme-linked Immunosorbent Assay
FDTD	Finite Difference Time Domain
GA	Glutaraldehyde
GMR	Guided-mode Resonance
HRP	Horse Radish Peroxidase
LFA	Lateral Flow Assay
LOD	Limit of Detection
PA	Photoacoustic(s)
PC	Photonic Crystal
PT	Photothermal
PVAm	Polyvinylamine
PVDF	Polyvinylidene Difluoride
Streptavidin	SA
SEM	Scanning Electron Microscopy
SNR	Signal-to-Noise Ratio

TMB	Tetramethylbenzidine
UVCP	Ultraviolet Curable Polymer

ABSTRACT

The early diagnosis of some chronic and severe diseases such as cancer, tuberculosis, etc. has been a long-sought goal of the medicine community. Traditional diagnostic tools such as X-ray and fecal blood tests cannot detect the disease before the focus or tumor have grown to an appreciable size or before the number of pathogens or tumor cells has reached a considerable amount in body fluids. These drawbacks could significantly delay the diagnosis. To detect and diagnose such diseases at an early stage, people have sought to detect the biomarkers related to certain physical conditions so that the anomalies caused by the diseases can be detected before a significant tumor has developed or the onset of symptoms. Driven by the needs to detect and quantify biomarkers, immunoassays have been developed. Two representative formats of immunoassays are enzyme-linked immunosorbent assay and lateral flow assay. They have been widely used for medical and research purposes, yet they still have drawbacks such as costly instruments and lack of sensitivity. To improve their performance, I have developed photoacoustic-based detection schemes that can be easily integrated with commercial immunoassay formats and can increase the sensitivity as well as lower the costs. For both assay formats, limit of detection has been lowered by two orders of magnitude with low-cost and portable instruments. As a follow up of the photoacoustic detection schemes, a technique based on photothermal lens is also developed. In this work, one-dimensional photonic crystal substrates have also been exploited to enhance the photoacoustic and photothermal signals. Due to the guided-mode resonance, the photonic crystal substrate can enhance the photoacoustic or photothermal signals by 10 to 40 times, making it a promising tool for biomarker detection.

CHAPTER 1. INTRODUCTION

The early diagnosis of chronic and terminal disease, such as cancer and tuberculosis, is a long-sought goal of the medical community. However, due to lack of symptoms, traditional diagnostic tools can hardly diagnose such diseases at their early stage, causing misdiagnosis or late treatment and, ultimately, the death of patients in numerous cases. To tackle this challenge, various diagnostic methods have been developed to detect the subtle anomalies caused by the early development of a disease, including X-ray of various types, such as computed tomography (CT) [1] and mammography [2], sigmoidoscopy [3], colonoscopy [4], pap tests [5] and fecal occult blood tests [6], etc. All these methods are aimed at detecting the early stage tumor, cancer cells, or the slight symptoms caused by them. The main drawback of such methods is that they are unable to detect cancer or some other diseases before the tumor or focus grows to a visible size or the number of cancer cells or pathogens reaches a significant number. To detect and diagnose such diseases at an even earlier stage, another type of method has been developed, i.e., to detect certain biomarkers the tumor cells secrete [7]. Such biomarkers are often characteristic of certain types of tumors, therefore they can not only help detecting the existence of cancer but also its type. Given that different types of cancer should be treated differently, this is an important advantage that helps the treatment of cancer compared with the aforementioned methods [8]. To ensure the specificity of the biomarker detection and minimize the chance of misdiagnosis or false positive, a type of assay called immunoassay has been developed that utilizes antibodies specific to the biomarkers in question to detect and quantify them [9]. Such antibodies are usually labeled with certain kinds of labels that are easy to detect, such as

fluorescent dyes, enzymes, radioactive isotopes, etc. [10]. There are also label-free immunoassays that usually employ the measurement of change in surface plasmon resonance or electrical resistance as the binding between unlabeled antibodies and antigens occurs [11]. Such methods benefit from the simplicity of equipment and short assay duration, but their sensitivity and accuracy are not yet comparable to label-based assays. Label-based assays are very sensitive, with LODs in the range of pg/mL, yet they also have their disadvantages, such as being very complicated and expensive, which limits their use in resource-limited settings; they are usually laboratory-based and the assay durations are very long. For most of the commercially available immunoassays with analytic accuracy, the reporters are either colorimetric, or fluorescent or chemiluminescent, which require specific instrumentation to read out the assay results. These instruments, such as the ELISA readers, are usually bulky and costly. These shortcomings of commercially available immunoassays limit their use as point-of-care diagnostic methods. The samples of immunoassays also introduce a problem. They are in liquid form for most assay formats and are thus chemically unstable, therefore they cannot be stored for a long time, which in some cases could be problematic for the study of the course of chronic diseases.

The aforementioned shortcomings of commercialized immunoassays have limited their use as point-of-care systems in resource-limited settings. The motivation of this work, therefore, is to overcome these drawbacks and develop simple, inexpensive, and rapid immunoassays suitable for point-of-care use. In this work, I developed immunoassay formats based on photoacoustic and photothermal detection. These assay formats are able to dramatically increase the sensitivity of the assays while retaining much of their simplicity.

In the following sections, the background of two formats of immunoassays, i.e. ELISA and LFA, are introduced. PA and photothermal lens (PTL) effects and their applications are also elaborated. Plasmonic nanoparticles and photonic crystal-based enhancement method. are also introduced, as they are used in the assays developed in this work.

1.1 Immunoassays and Biomarker Detection

1.1.1 Immunoassays and ELISA

The ability to detect and quantify disease-related biomarkers at trace concentrations is deeply desired, for it enables diagnosis of the corresponding disease at an early stage [8, 12-14]. The predominant methods used for biomarker detection rely on immunoassays. An immunoassay is a biomedical procedure that detects the presence or measures the concentration of a biomolecule in a solution by using antibodies or immunoglobulins. In an immunoassay, the target molecule is recognized by antibodies that specifically bind to it. Immunoassays can target specific biomarkers and measure their concentrations with very high sensitivity and specificity. Most immunoassays employ some type of labeling materials, such as enzymes, fluorescent dyes, or radioactive isotopes, to generate a detectable signal [15-19]. The intensity of the signal generated by the labels can indicate the presence or concentration of the target molecule. The target molecule is often referred to as an “analyte” and is in most cases a protein. Analytes in serum and urine are often measured for medical or research purposes. Immunoassays can be divided into different categories. Some assays require multiple steps to carry out. They are called “heterogeneous immunoassays”. Others can be carried out by simply mixing all the reagents and samples and making a physical

measurement. These assays are called “homogeneous immunoassays”. In immunoassays, a calibrator solution that contains a known concentration of the analyte is often used to relate the signal strength to the analyte concentration. Among the various types of immunoassays, enzyme-linked immunosorbent assays (ELISAs) are considered the gold standard, where enzymatic tags are used to generate colorimetric signals in liquid substrates. Usually, the enzyme used in this assay triggers a color-changing reaction (named as a colorimetric reaction) and such ELISA is called colorimetric ELISA. ELISA is often used as a diagnostic tool in medicine and plant pathology. ELISA is carried out in microtiter plates which contain little wells where the reagents are mixed and are allowed to react. Figure 1 shows a colorimetric multiplex ELISA that is used to measure 3 analytes in a single test. There are various formats for ELISA, one is called direct ELISA, in which only one antibody is used. Other formats include indirect ELISA, sandwich ELISA, and competitive ELISA, in which multiple antibodies are used to identify the target molecule. In this work, we used the sandwich format, because it is very sensitive (usually 2 to 5 times more sensitive than direct or indirect ELISA), and the samples need not be purified before the assay. The analyte we chose was human interleukin-8 (IL-8), a biomarker indicative of diseases such as inflammation, obesity, and cancer [20, 21].

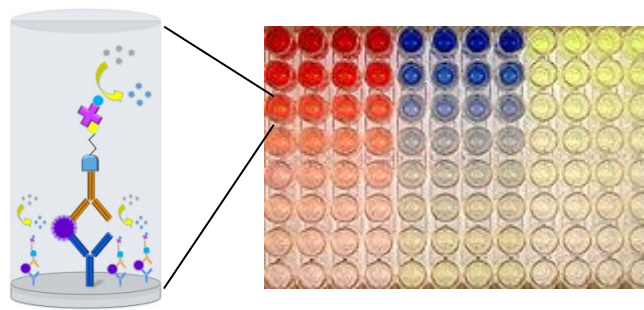


Figure 1. Colorimetric ELISA performed in 96-well microtiter plate [22].

The sandwich ELISA, as shown in Figure 2, involves the following steps. The assay starts with a pre-treated microtiter plate, with capture antibody adsorbed on the bottom of each well. Then, samples with the analyte, a solution with biotinylated detection antibody, a solution of SA conjugated horseradish peroxidase (SA-HRP), tetramethylbenzidine (TMB) substrate and stop solution are sequentially added, with incubation after each addition and washing steps before the next addition of each reagent. In this assay, the analyte is first specifically bound to the capture antibody during the first incubation, and then the sample is washed away in order to eliminate non-specific bindings. Then the same procedure is repeated for the biotinylated detection antibody and SA-HRP so that they can sequentially and specifically bind to the antibody-antigen complex. After that TMB substrate is added and the microtiter plate is incubated for 30 minutes. In this step, the TMB substrate undergoes a colorimetric reaction under the catalysis of HRP. After 30 minutes of incubation, a stop solution is added to stop the reaction. Since the reaction rate is related to the concentration of HRP, which is in turn related to the analyte concentration, a strong color after the assay indicates a sample with high analyte concentration, and a weak color indicates a low

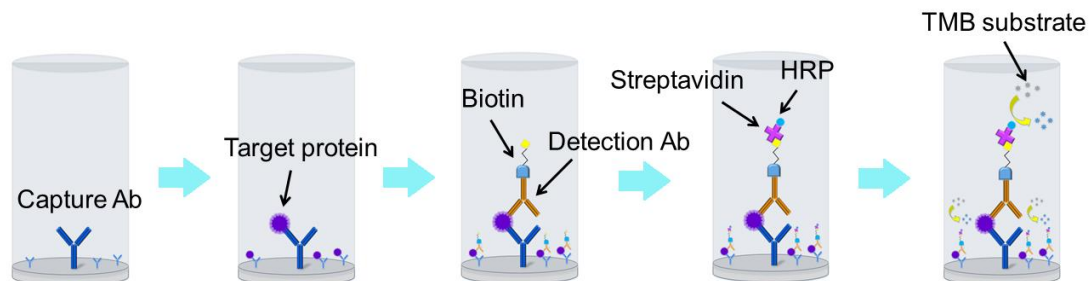


Figure 2. The assay protocol of sandwich ELISA. Capture antibody (Ab) is pre-coated onto the bottom of each well in the microtiter plate, and sample, detection antibody, SA-HRP, TMB substrate and stop solution is sequentially added. At the end of the assay, the microtiter plate is inserted into an ELISA reader to read out the results.

concentration. This concentration is quantified using an ELISA reader that measures the difference of optical absorption of the liquid phase product in each well between 550 nm and 450 nm.

Apart from colorimetric ELISA, other forms of immunoassays have also been developed, for example, chemiluminescence- and fluorescence-based immunoassays have become popular for protein analysis, owing to their capabilities of achieving improved sensitivities [23, 24]. However, their drawbacks include the need for catalysts or enhancers, a long incubation time before reaching a stable output signal, the degradation of labels, and the use of expensive optical detectors and filters [25, 26]. An ideal biomarker detection assay should offer high sensitivity, high specificity, low-cost instrumentation with high throughput, and long-term stability of the labels for future analysis.

The development of nanomaterials and nanoparticles during the past decade provides tremendous opportunities to address existing challenges in biomarker detection on a nanoscale [27-29]. In particular, the interaction of light with a metal nanoparticle results in the collective oscillation of free electrons within the nanoparticle, which is known as localized surface plasmon resonance (LSPR) [30, 31]. LSPR is associated with a strongly localized and greatly enhanced evanescent field, which has been utilized in several areas of research, including photovoltaics, photocatalysis, biomolecule sensing, cell imaging, and photothermal therapy [32-36]. Here, we utilized the photothermal effect of gold nanoparticles (AuNPs) to develop a new type of immunoassay, referred to as the photoacoustic (PA)-immunoassay. AuNPs were chosen for three main reasons. First, AuNPs can effectively convert photons into heat owing to non-radiative resonant absorption. The strong photothermal effect of AuNPs has been successfully utilized to selectively kill target cells

and to serve as a signal enhancer for photoacoustic tomography [37, 38]. Second, surface AuNPs can be conjugated with various types of ligands that recognize target biomarkers with high specificity [39]. Third, owing to their excellent physical and chemical stabilities, AuNPs can generate reproducible signals. By quantifying the PA signal, which is directly proportional to the amount of AuNPs, the nanoparticle-based immunoassay enables a sensitive, repeatable, and inexpensive approach for analyzing biomarkers.

1.1.2 Lateral flow assay

Lateral flow assays (LFAs), or lateral flow tests, are simple and rapid tests aimed at detecting the presence (or absence) of certain target molecules in samples without the need for specialized and expensive equipment. This kind of assays enables the simple and rapid analysis of biomolecules in complex biological samples, such as human body fluids [41]. Thanks to their simplicity and rapidness, LFA tests require minimal effort for sample preparation and are thus desirable for point-of-care testing at home and in clinics [42-44]. LFA is well known for the home pregnancy testing. It can also be used in the lab with higher accuracy if needed [45]. Robust, inexpensive, and portable LFA tests have been successfully used for food safety monitoring, disease diagnostics, and drug tests [46]. The core component of most LFA sensor strips is a nitrocellulose substrate. As illustrated in Figure 3, it is composed of a sample pad on one end, a conjugation pad, a capillary bed and an absorbent pad on the other end. During a test, the sample pad is dipped onto a small amount of liquid sample, or a drop of liquid sample is dropped onto the sample pad. Owing to the capillary force, liquid samples are transported to the conjugation pad, where analyte (or antigen) in the sample binds to the corresponding antibody, which is usually labeled with an AuNP [47].

The fluid continues to wick up to the capillary bed and gets to the test line, where capture antibody immobilized at the test line captures the antigen-antibody complex if there is any. This will cause a dark line to develop at the test line, and the depth of its color is measured for the purpose of qualitative or semi-quantitative analysis of the analyte. There is also a control line on the capillary bed that develops a dark line regardless of whether there is analyte present in the sample. The purpose of the control line is to indicate the proper flow of the fluid sample and thereby validating the test. The absorbent pad on the other end acts as a waste container, as well as maintaining the flow of the sample liquid. Among the different types of detection mechanisms, including colorimetry, fluorescence, and chemiluminescence, colorimetric sensing using colloidal gold nanoparticles (AuNPs) or enzymatic dyes is the most often used for LFA tests [48]. The colorimetric analysis allows a read-out with the naked eye but has the drawback of poor sensitivity compared with laboratory-based molecular techniques. On the other hand, high detection sensitivity is critical for some

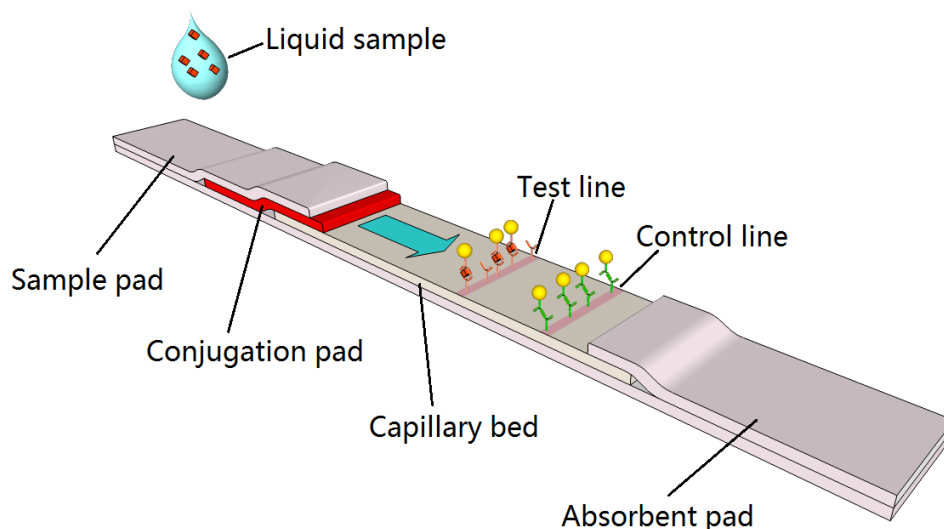


Figure 3. The structure of an LFA paper strip. It is composed of a sample pad, a conjugation pad, a capillary bed and an absorbent pad [49].

disease-relevant analyses, particularly in cases where the analyte concentration is extremely low. For example, a protein biomarker expressed by cancer cells may be present at concentrations below 100 pg/mL in a blood sample [16].

The commercialized lateral flow test is qualitative or semi-quantitative, whose sensitivity is much lower than lab-based analytic assays. To improve the sensitivity of LFA tests several approaches have been investigated, including paper-based microfluidics for signal amplification [50], novel schemes for concentrating analytes [51-54], and new detection strategies, such as surface enhanced Raman scattering and temperature-humidity control [55, 56]. There are also some devices that can measure the intensity of the test line by illumination of certain wavelengths of light and measurement through CMOS or CCD cameras. Recently, Bischof's group demonstrated a significant improvement of LFA sensitivity using the photothermal signals generated by AuNP [57]. Photothermal detection exploits the strong light absorption of AuNPs due to localized surface plasmon resonance (LSPR), which represents the oscillation of free electrons in metal nanoparticles and results in a strong interaction of AuNPs with excitation light [58]. Recently, AuNPs have been devised for many biomolecular applications, such as photothermal therapy [59], nanoscale biosensors [60-63], and enhanced Raman and fluorescence spectroscopies [64, 65]. In this study, we exploited AuNPs for the development of a photoacoustic (PA) detection mechanism to achieve a highly sensitive and quantitative LFA test while retains much of its simplicity.

1.2 Photothermal Effects and Their Applications

1.2.1 Photoacoustic effect

Photoacoustic effect was discovered in 1880 by Alexander Graham Bell when he was experimenting on long-distance sound transmission. He used what he called a “photophone” to transmit vocal signals by reflecting sunlight from a mirror, whose motion was modulated by the vocal signals, to a selenium solar cell receiver [66]. In his experiment, he inadvertently discovered that sound waves were directly generated from a solid sample when it was exposed to sunlight that was rapidly and periodically interrupted by a rotating slotted wheel [67]. He also discovered the dependence of this acoustic signal on the material of the sample and correctly reasoned that this PA effect was caused by the absorption of the optical energy of a modulated light source. The optical energy subsequently turned into heat and the thermal expansion and contraction of the sample itself or the surrounding medium, producing a pressure wave that propagated out as an acoustic signal.

The PA effect can be used for various applications. Since the intensity of the PA signal is proportional to the optical absorption, this effect can be used to measure the absorption spectrum of a material when the wavelength of incident light is changed, whereas traditional spectroscopies usually measure the reflection or extinction spectrum. In traditional absorption spectroscopy, absorption is measured by comparing the difference of the intensity of a light beam before and after its passage through a sample. It has two disadvantages, one is that the measurement result is not strictly absorption spectrum, but extinction spectrum that involves both absorption and scattering; the other is that it is not applicable when the absorbent concentration is extremely small. PA spectroscopy does not have such limitations [68]. The PA signal can be amplified by amplifiers or by increasing the incident light

intensity when measuring trace amounts of absorbent, and it strictly reflects the absorption, instead of the extinction of the sample. The PA method can also measure samples that are completely opaque, which traditional absorption method cannot handle. Due to the fact that the thermal diffusion length is very small, usually in the order of several microns [69], this allows the analysis of the surface rather than the bulk [70]. Depth profiling and PA imaging are also possible due to the fact that the thermal diffusion length is related to modulation frequency and excitation wavelength [71].

Another application is the measurement of chemical energy related to photochemical reactions. When light is incident upon photochemical reactants, reactions occur and part of the optical energy is absorbed. This causes the reduction of heat produced and can cause a reduction in the PA signal that can be quantitatively measured. Photosynthesis is a major field where this method is applied [72]. Another application is the study of the conversion of optical energy to electrical energy in solar cells [73].

In this work, the PA method is chosen for the following reasons: first, the PA method can measure the surface of a sample rather than the bulk, which makes it possible to have small solid samples instead of liquid samples which are currently used in commercialized immunoassays. These solid samples are easier to handle and chemically stabler. Second, the detection instruments for PA detection are relatively simpler, smaller and less expensive than the readout systems of traditional immunoassays. The instruments include a PA unit of hand-held size, which is a small air-tight chamber that has a microphone enclosed in it, a light source (in this work we mainly used lasers) and a data acquisition device such as an oscilloscope or a lock-in amplifier. The detection of a disease at its very early stage requires the detection of trace amounts of biomarkers characteristic of the disease in question;

therefore a strong PA signal for a very low concentration of the analyte in the sample is desired. To fulfill this requirement, one must find a proper label that has a strong optical absorption. This leads us to the next part of the introduction, the plasmonic nanoparticles.

1.2.2 Photothermal lens effect

The generation of PA signals involves optical, thermal and acoustic properties of a sample. These properties can in some cases complicate the interpretation of the signal considerably. Photothermal (PT) effects, on the other hand, involves only optical and thermal properties of a sample and is, therefore, simpler for people to interpret the signal. Photothermal spectroscopy indirectly measures the sample absorbance through the detection of heat generation by samples [74, 75] under the illumination of a pump light. In contrast to conventional optical spectroscopy, with which the transmitted or scattered radiation is analyzed and compared to the incident radiation in order to extract information on the optical properties of the analyte, in photothermal techniques the absorbed optical energy is detected as radiation induced heating of the sample. This greatly facilitates the measurement of weakly absorbing samples, such as surfaces and thin films, in which case the difference between transmitted beam and incident probe beam is too small, or strongly absorbing samples, such as bulk materials, in which case there is little to no transmission at all [74]. In addition to the aforementioned advantages, PT effects have several other advantages, including zero-referenced measurements (signal output is zero without absorption), the sensitivity increases with pump light power, and is only limited by thermal fluctuation of the ambient environment [75], not affected by ambient light noise. As a result, the photothermal techniques are highly sensitive when applied to the quantitative determination of the sample absorption [76].

Photothermal techniques can be implemented in several formats, such as photothermal deflection (mirage effect) spectroscopy, photothermal lens technique, photothermal radiometry and photothermal interferometry. Of which, photothermal lens (PTL) [77, 78] and photothermal deflection [79, 80], have been successfully implemented for chemical analysis, microscopic study of nanoparticles, biomolecule sensor, etc. [81-84]. With photothermal deflection technique, a probe beam is set to be parallel and in close proximity to the sample surface. A pump beam heats a spot beneath the path of the probe beam on the sample surface and generates a temperature gradient in the surrounding medium (usually air) close to the heated spot. This temperature gradient, in turn, causes a refractive index gradient, thereby deflecting the probe beam. The position of the probe beam is monitored with a position-sensitive photodetector. The amount of the shift in probe beam position can be used to extract information about the properties of the sample or its concentration. In the case of photothermal lens technique, the refractive index gradient forms an optical element that acts as a scattering/collecting lens. Since most materials' refractive index decreases with an increase in temperature, a photothermal lens is usually concave and hence acts as a scatterer. As an analytic method, photothermal spectroscopy offers several important features for chemical analysis. For example, material absorption in the UV, visible, IR, and THz ranges can all be measured with minimum modifications of the detector. The thermodynamic changes of the sample or surrounding materials are highly proportional to the material absorption. In addition, the sample quantification can be performed over a substantial range of concentrations. In order to characterize optically thin samples, detection apparatuses, such as the attenuated total reflection [85], optical cavities [86, 87], and micromechanical devices [88], have been demonstrated. In this work, the schematics of the optical setup is similar to a

surface thermal lensing technique, in which the probe beam is directed towards the heated spot on the sample surface at an angle, and the reflection off the sample surface is observed. This configuration has several advantages over traditional deflection technique, one of them being a less stringent requirement on alignment. If the probe beam spot size exceeds that of the pump beam, there are no rigorous requirements on alignment. Another reason for choosing a reflection configuration is that in this way the probe beam can be easily coupled with a GMR of the PC substrate so that the shift of the GMR can be used to enhance the PTL signal. Here, to improve the sensitivity of PTL detection, a one-dimensional photonic crystal (PC) surface is exploited to magnify the change of the probe beam, and results in stronger PTL signals.

The PC slab, comprised of a nanostructured dielectric thin film, supports a leaky-mode resonance, which is also known as a guided-mode resonance [89-91]. When the PC surface is excited under resonance conditions, the PC resonance occurs and leads to narrowband optical resonances with an intensified local field. Several applications of PC-based devices have been demonstrated for optical filters, refractometric sensors, and fluorescence-based biosensors [16, 92-95]. Here, the PC surface is exploited to enhance the PTL for two main reasons. First, the PC structure can be engineered to exhibit the resonant wavelength from visible to mid-infrared [96], and thus the resonant wavelength can be easily matched to the light beams used in the PTL system. Second, it is inexpensive to fabricate PC structures over a large surface area using plastic materials with low thermal conductivity [97]. My previous work has successfully shown the PC-enhanced photoacoustic phenomena based on the strong near field of the PC resonance [98].

This part of my work focuses on the PC-enhanced PTL effect that is characterized using a pump-probe scheme. The light absorbing material coated on the PC substrate is heated by the pump beam and generates the thermal lens, which is monitored by the probe laser beam at a different wavelength. The probe laser beam is coupled to the resonant mode of the PC and its reflection from the PC is proportional to the PTL strength. The PC surface enhances the PTL signal via the following mechanisms. The narrowband resonance of the PC is sensitive to the thermal lens due to the heat-induced change in the refractive index. Without heating, the probe light is reflected by the PC with high reflectivity (R). In the presence of a thermal lens, the shift of the PC resonance significantly reduces the reflectivity. As a result, the PC substrate can magnify the change of reflectivity (ΔR) relative to an unpatterned surface. In this paper, two PTL experiments are carried out to demonstrate the PC-enhanced PTL analysis of organic dye molecules and metal nanoparticles.

1.3 Plasmonics and Photonic Crystals

1.3.1 Plasmonic nanoparticles

Plasmons are the collective oscillation of electrons induced by electromagnetic waves (Figure 4 (a)). Plasmonic nanoparticles are metal particles whose electron density can couple with electromagnetic waves (in most cases, infrared or visible light) of wavelengths far larger than the size of the particles, as shown in Figure 4 (b), unlike in the usual case where there is a limit of the wavelength that can be coupled to a piece of metal depending on its size. This is due to the properties of the metal-dielectric interface between the particles and the surrounding medium [99]. The plasmonic effect can occur only when the light frequency is lower than or equal to the plasma frequency of the nanoparticles. For the light of a higher

frequency than the resonance frequency, the destructive interference of electron oscillation will occur inside the particle and there will be no plasmonic effect.

The reason why plasmonic nanoparticles are important in this work is that they have a very strong optical absorption at the resonance wavelength. According to the Drude model, the absorbance cross section for spherical nanoparticles is described by the following equation [100]:

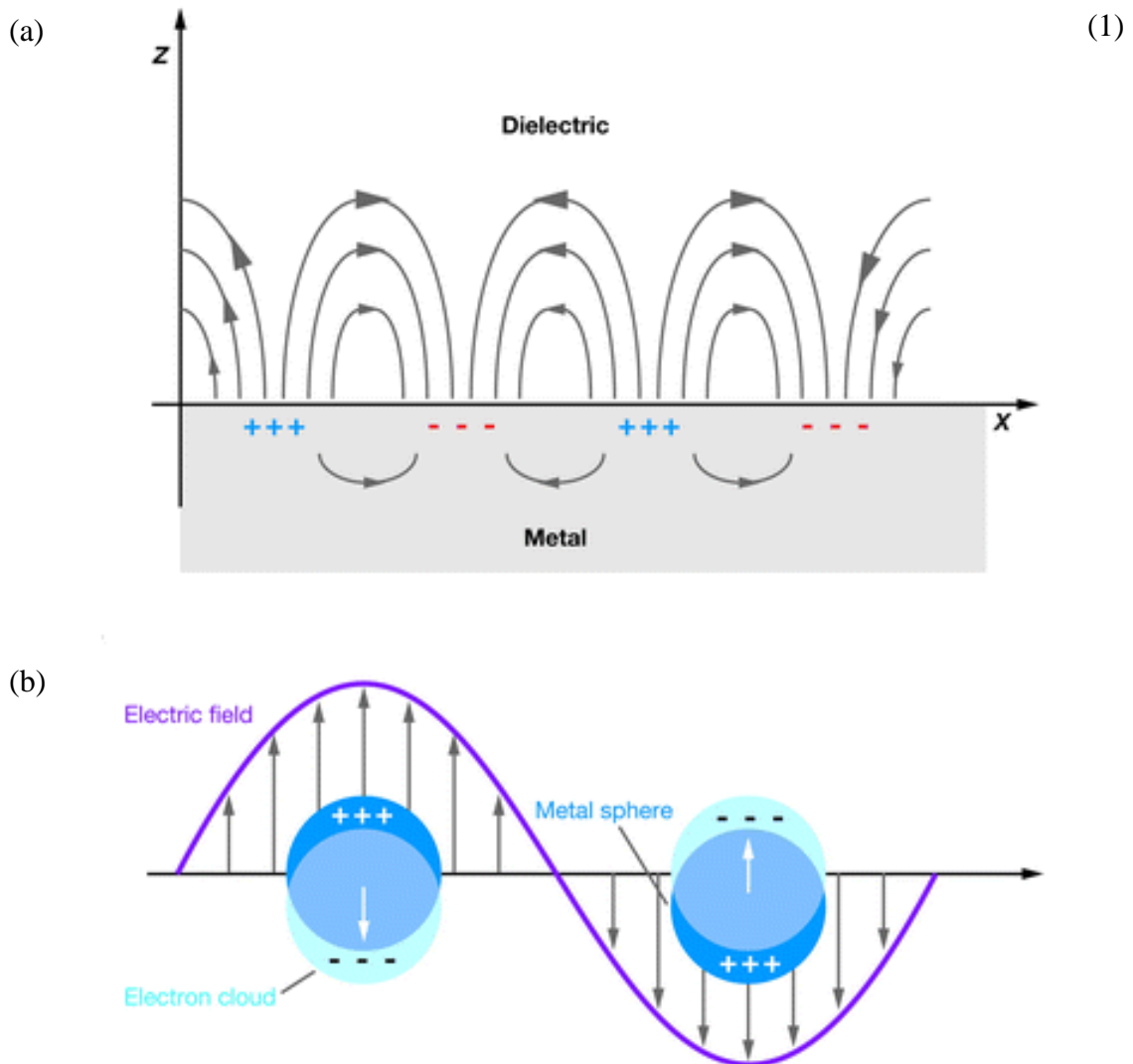


Figure 4. Illustration for plasmonic resonance. (a) Plasmonic effect and (b) localized surface plasmon resonance of metal nanoparticles. The electron cloud oscillates at the same frequency with the incident light wave [30].

$$\sigma_{abs} = 4\pi k R^3 \text{Im} \left| \frac{\varepsilon_{particle} - \varepsilon_{medium}}{\varepsilon_{particle} + 2\varepsilon_{medium}} \right|$$

where R is the particle radius, k is the wave vector, and ε is the permittivity. $\varepsilon_{particle}$ is the permittivity of the particles. According to Drude model [100],

$$\varepsilon_{particle} = 1 - \frac{\omega_p^2}{\omega^2} \quad (2)$$

where ω_p is the plasma frequency and ω is the frequency of the electromagnetic wave. The resonance condition is satisfied when the denominator approaches zero [100]:

$$\varepsilon_{particle} + 2\varepsilon_{medium} \approx 0 \quad (3)$$

The frequency ω that allows $\varepsilon_{particle}$ to satisfy the above equation is thus the resonance frequency of the particles in question.

In this work, functionalized gold nanoparticles (AuNPs) are chosen for the label of the biomarkers. AuNPs have several properties that are favorable for this application. One is that gold is very chemically inert and therefore samples labeled with AuNPs are very stable and have a very long shelf life; the other is that AuNPs have a very strong plasmonic resonance and hence strong absorption, making them ideal labels for PA detection. A third reason is that AuNPs can be easily functionalized so that they can specifically bind to the target biomarkers. This can ensure the specificity of the assay and reduce cross-binding and false positives. Since AuNPs have these advantages, we applied them to an immunoassay that is widely used in diagnostics, i.e. the ELISA.

1.3.2 Synthesis of gold nanoparticles

The synthesis of nanoparticles can be divided into two major categories: one is a top-down approach and the other is a bottom-up approach [101]. In a top-down approach, one starts with a bulk of gold and breaks it down to nanoscale pieces. It usually requires a pattern or matrix to control particle assembly and formation, such as an anodized aluminum oxide (AAO) or a track-etched polymer membrane, both known as the “hard-template method”. The AAO is formed by electrochemically oxidizing aluminum in an acidic electrolyte. The product of this reaction has a high density of parallel pores (as high as 10^{11} pores/cm²) regularly situated on a hexagonal lattice of high uniformity [102]. The track-etched polymer membrane is fabricated by exposing a polymer film to the bombardment of nuclear fission fragments, leaving damage tracks, and then chemically etched into pores [101]. Then, the materials of interest can be deposited into the pores via electrochemical deposition. The above top-down methods offer good control over particle size, size distribution, and shape, and are suitable for mass production of particles of specific shapes. Top-down methods have limitations in terms of the physical dimensions of the nanostructure they can achieve, therefore, in the past few decades, bottom-up methods have flourished, as this category of methods build up nanoparticles from atomic or molecular precursors, and do not have the same limitations as the top-down methods do [103]. Take the synthesis of gold nanoparticles as an example, bottom-up methods start with a liquid solution of individual molecules of gold compounds, then use reductant to reduce gold compound to elemental gold. The subsequent nucleation and growth will form gold nanoparticles of the desired size determined by the parameters of the solution, such as temperature, pH and the concentration of the stabilizer. One of such bottom-up methods is Turkevich-Frens method,

in which HAuCl_4 is reduced by citrate, tannic acid, etc. and the AuNPs are stabilized by citrate [104, 105]. The size of AuNPs obtained by this method typically ranges from 5 nm to 150 nm [106]. Another bottom-up method is Brust-Schiffrin method, in which NaBH_4 is used to reduce HAuCl_4 and thiolate is used to stabilize AuNPs [107]. This method is particularly advantageous when used to synthesize thiolate-liganded AuNPs. Since the strength of the reductant used in Brust-Schiffrin method is much stronger than those used in Turkevich-Frens method, the reaction rate, according to Marcus theory, is much higher. This results in a much smaller size of AuNPs than those synthesized using citrate reductant, usually in the range of 2 nm to 5 nm [106]. AuNPs can also be stabilized by various other chemicals or ligands, such as phosphorus ligand, amine, carbonyl, carboxyl and phenol groups, etc. [106].

The gold nanoparticles used in this work are functionalized gold nanorods. These gold nanorods are synthesized using one-dimensional surfactant-directed synthesis. Briefly, the gold nanorods are synthesized in aqueous solution with the presence of cetyltrimethylammonium bromide (CTAB), a surfactant that preferentially binds to certain crystal faces of gold. Therefore, it can inhibit the growth along certain directions and the gold nanoparticles will grow into nanorods [103]. The dimensions of the gold nanorods I used in my work are 25 nm in diameter and 71 nm in length, and functionalized with biotin or SA.

1.3.3 Heat generation of nanoparticles

When a substance absorbs light, the optical energy can be transformed into various forms of energy in the process. Although the final forms of energy may be different, the process usually involves a process known as electron excitation, in which electrons at lower

energy states are transferred to higher energy states (but not ionized). When the electrons fall back to lower energy states (electron relaxation), they release the energy in various forms. If they undergo radiative decay, they will release the energy in the form of photons. The photon energy is equal to the energy difference between the higher and lower energy states. Phenomena caused by radiative decay include spontaneous emission, such as fluorescence, phosphorescence, light emission during combustion, etc. There are also non-radiative transition mechanisms, i.e., transitions without emitting a photon. The energy difference between energy states is then released in some other forms – usually in the form of phonons, which are associated with lattice vibrations. Such vibrations manifest themselves as heat in our macroscopic world.

The optical absorption of metal nanoparticles (NPs) falls into the category of non-radiative transitions. Free electrons, driven by the electric field of the incident radiation, collectively oscillate within NPs and collide with the nuclei, transferring the energy into the vibration modes of the crystal lattice. The vibration of the lattice then manifests itself macroscopically as heat. The heating effect is dramatically intensified when the frequency of the incident radiation matches the natural oscillation frequency of the free electron under the restoring force of the positive nuclei. This effect is named as plasmon resonance.

The heating effect of metal nanoparticles can have several secondary effects. For instance, the heat generated by the NPs can destroy tumor cells that they attach to through biomolecular conjugation [108]. Another example is that the heat can alter the refractive index of the surrounding medium, creating a “photothermal lens” that can deflect probing light beams. This effect can be used to characterize the properties and concentration of a given substance on a substrate. In the case where the incident pump beam is modulated, the

heat generation will also be modulated. This can lead to modulated thermal expansion (and contraction), thus giving rise to a pressure oscillation or an acoustic wave. This effect is named as “photoacoustic effect”, which also can be used for characterization of optically absorbing samples. All the above phenomena and applications depend on one aspect of the heating effect, i.e. the temperature increase. The temperature distribution is directly related to the heat transfer from metal NPs to the surrounding medium, as described in Eq. 4 [108]:

$$\rho(\mathbf{r})c(\mathbf{r})\frac{\partial T(\mathbf{r},t)}{\partial t} = \nabla k(\mathbf{r})\nabla T(\mathbf{r},t) + Q(\mathbf{r},t) \quad (4)$$

where \mathbf{r} and t are spatial and temporal coordinates, ρ , c and k are density, specific heat and thermal conductivity considered as functions of \mathbf{r} , T and Q are local temperature and heat generation considered as functions of both \mathbf{r} and t , respectively. The heat generation Q can be further expressed as (Eq. 5) [108]:

$$Q(\mathbf{r},t) = \langle \mathbf{j}(\mathbf{r},t) \cdot \mathbf{E}(\mathbf{r},t) \rangle_t \quad (5)$$

where \mathbf{j} and \mathbf{E} are current density and excitation electric field of the pump light. In general, Eq. 4 can only be solved using numerical methods, but in the case of a single NP in a homogeneous and isotropic medium, it can be easily solved analytically. The steady state solution to Eq. 4 is described by Eq. 6 as follows [108]:

$$\Delta T(\mathbf{r}) = \frac{V_{NP}Q}{4\pi k_0 r} \quad (6)$$

where V_{NP} is the volume of the NP. From Eq. 6 we can conclude that the temperature change due to heating of the NP is inversely proportional to the distance to the NP. For a spherical metal NP, assuming that the wavelength of the incident radiation is much larger than the dimension of the NP, the heat generation Q can also be analytically solved as (Eq. 7) [108]:

$$Q = \frac{\omega}{8\pi} E_0^2 \left| \frac{3\varepsilon_0}{2\varepsilon_0 + \varepsilon_{NP}} \right|^2 \text{Im}\varepsilon_{NP} \quad (7)$$

where ε_0 and ε_{NP} are the permittivities of the medium and the NP, respectively, and E_0 is the optical field of the incident radiation. Combining Eq. 3.3 and 3.4 will yield the temperature at the surface of the NP, which is the maximal temperature in the surrounding medium (Eq. 8) [108]:

$$\Delta T_{\max}(I_0) = \frac{R_{NP}^2 \omega}{3k_0 8\pi} \left| \frac{3\varepsilon_0}{2\varepsilon_0 + \varepsilon_{NP}} \right|^2 \text{Im}\varepsilon_{NP} \frac{8\pi \cdot I_0}{c\sqrt{\varepsilon_0}} \quad (8)$$

where I_0 is the intensity of the pump beam. Note that the temperature change is proportional to the square of the NP radius at a given incident radiation intensity. Using Eq. 3.5, we can calculate the temperature change of various NPs with different chemical composition and radii.

Because of the importance of temperature change of the NPs, calculations have been made to compare nanoparticles of different composition and sizes. Heat generation rate of silver NP (AgNP), AuNP, CdTe and CdSe NPs are compared in Figure 5. It is worth noting that AgNP generates roughly 10 times as much as heat as AuNP does at its plasmon resonance wavelength. This is consistent with previous studies on plasmon resonance of Ag and Au. However, due to its chemical stability, Au is still favored in biomedical applications as agents for cancer therapy, or labels in photothermal and photoacoustic detections. The heat generation of CdSe and CdTe NPs is very low compared to AgNP and AuNP. This is because the heating mechanism for semiconductor NPs is the generation of electron-hole pairs and the subsequent non-radiative recombination, no collective motion of charge carriers exists. Therefore, no plasmon resonance exists, either.

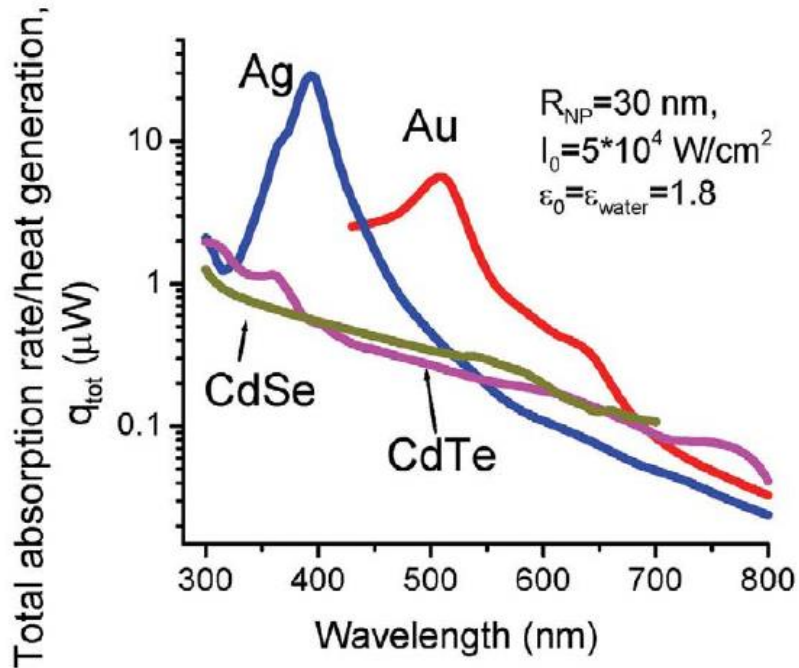


Figure 5. The calculated rate of heat generation of Ag, Au, CdSe and CdTe NPs [108].

Since AuNP is the most widely used NP in biomedicine, it is necessary to calculate the relation between temperature change and the radius of the AuNP. The relation between AuNP radius, light flux and temperature change at the NP surface is described in Figure 6. The temperature change is proportional to the light flux of the incident radiation, as expected. If we compare the temperature increase with the AuNP radius for a given light flux, we can find that the temperature change is proportional to the second power of AuNP radius as well. For example, at 900 W/cm^2 , a AuNP with a radius of 10 nm can generate a temperature increase of 0.04 K, while an AuNP with a radius of 100 nm can increase the temperature of its surface by 4 K at the same light flux, an increase of 100-fold with only a ten-fold increase in radius.

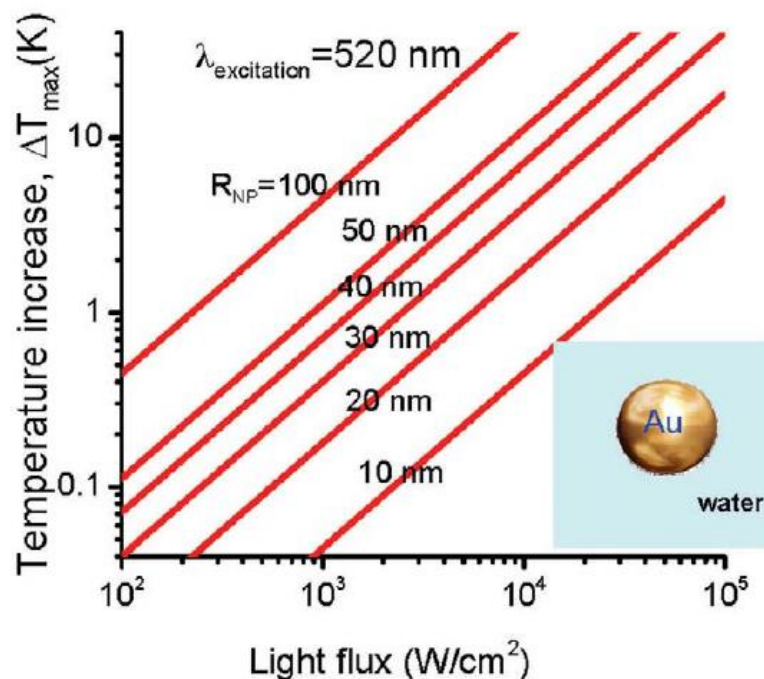


Figure 6. The calculated temperature increase at the surface of a single Au NP in water as a function of illumination power at the plasmon resonance [32].

The situation of one single NP in a homogeneous and isotropic medium is very easy to calculate. However, in the general case of photoacoustic and photothermal detections, usually multiple NPs are involved and they are located at the interface of two media. Therefore, we have to calculate the temperature distribution numerically. In the next chapter, I will elaborate on the simulation of the temperature distribution of NPs on a polystyrene substrate excited by incident radiation.

1.3.4 Photonic crystal

PA spectroscopy has attracted great interest since the mid-1970s due to its capability to non-invasively monitor light absorbing analytes over substantial ranges of concentrations [109-112]. PA detection is very advantageous when detecting samples with low analyte concentrations, as the absorption of the samples is too low for traditional absorption

spectroscopy to detect. Although laser-based PA detections exhibit a higher sensitivity as compared to optical absorption measured directly by transmission spectroscopy, it is always desirable to improve the signal-to-noise (SNR) ratio to accurately quantify trace amounts of molecules. To maximize the signal-to-noise ratio of PA measurements, a variety of approaches have been studied for the purpose of amplifying acoustic output and suppressing noise. The reported signal enhancements arise from two major effects: acoustic resonance and optical resonance [113-117]. Since utilizing acoustic resonance may require a large chamber whose size is comparable to the wavelength of sound, we favored the use of optical resonance as a means of signal enhancement. Notably, optical resonance-based methods utilize cavities, formed by high reflectivity mirrors or micro-/nanostructures, to increase optical path length and to result in enhanced absorption by the target molecule residing inside the cavity [118].

To address the challenge of measuring solid substance at low concentrations or with low absorption coefficient, we propose to use a one-dimensional photonic crystal (1-D PC) structure to increase light absorption and to generate a stronger PA output consequently. The PC substrate, comprised of a periodically nanostructured dielectric thin film, supports guided-mode resonance (GMR), also known as a leaky mode [96, 119, 120]. GMR (shown in Figure 7) is a phenomenon in which guided modes of a waveguide (in this case the high-refractive-index TiO_2 layer) can be excited or extracted through a phase-matching device, such as a grating or prism. As the mode can be coupled in as well as coupled out, the mode is also called a “leaky mode”. The effective refractive index n_{eff} of a waveguide in a 1-D PC is described by:

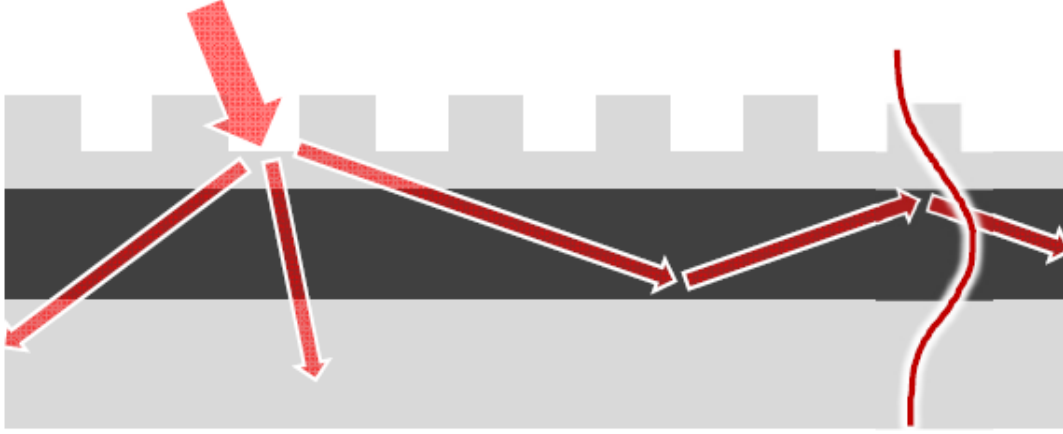


Figure 7. Guided-mode resonance. The phenomenon wherein a diffraction mode of a grating is coupled into a guided mode of the waveguide beneath it is called GMR. This can also be achieved by other phase-matching elements such as a prism [121].

$$n_{\text{eff}} = n_1 \sin \theta_{\text{in}} - m \frac{\lambda_0}{\Lambda} \quad (4)$$

where n_1 is the refractive index of the surrounding medium, θ_{in} is the incident angle of excitation light, λ_0 is the wavelength of the excitation light in free space and Λ is the period of the 1-D PC. n_{eff} represents a guided mode resonance when it satisfies the following condition:

$$\max[n_1, n_3] \leq n_{\text{eff}} < n_2 \quad (5)$$

where n_1 and n_3 are the refractive indices of the medium above and beneath the waveguide, respectively and n_2 is the refractive index of the waveguide. The GMR effect occurs when the PC substrate is illuminated under resonance conditions and leads to intensified local field with respect to the electric field strength of the incident light. By spectrally overlapping a GMR resonance wavelength with the absorption band of the analyte, one can obtain an increase in the optical absorption. Previous publications have demonstrated the application of a PC substrate for fluorescence-based detections [16, 97, 122, 123]. Several compelling features of the PC are of practical importance for the development of an enhanced detection

scheme to be used in PA analysis. The PC structure can be tailored to tune the GMR wavelength from visible to mid-infrared, and thus the GMR wavelength can align with the absorption bands of a wide variety of substances [124-126]. It is inexpensive to fabricate large surface areas of PC substrates using optically transparent materials and to incorporate them into a PA detection instrument. In addition, the PC substrate is made using polymer materials with low thermal conductivities that prevents heat dissipation and ensures strong PA signal output. This part of my work involves design and experimental characterization of a PC sensor for enhanced PA detection of organic dye molecules and metal nanoparticles.

1.4 Acknowledgment

Parts of this chapter have been modified from my previous publications:

Zhao, Y., Cao, M., McClelland, J. F., Shao, Z., & Lu, M. (2016). A photoacoustic immunoassay for biomarker detection. *Biosensors and Bioelectronics*, 85, 261-266.

Zhao, Y., Huang, Y., Zhao, X., McClelland, J. F., & Lu, M. (2016). Nanoparticle-based photoacoustic analysis for highly sensitive lateral flow assays. *Nanoscale*, 8(46), 19204-19210.

Zhao, Y., Liu, K., McClelland, J., & Lu, M. (2014). Enhanced photoacoustic detection using photonic crystal substrate. *Applied Physics Letters*, 104(16), 161110.

Zhao, Y., Liu, L., Zhao, X., & Lu, M. (2016). Enhanced photothermal lens using a photonic crystal surface. *Applied Physics Letters*, 109(7), 071108.

CHAPTER 2. PHOTOACOUSTIC IMMUNOASSAY

2.1 Principle of Photoacoustic Immunoassay

Since the mid-1970s, the PA detection has attracted considerable interest in the analytical community due to its capability of measuring optical absorption of samples in gaseous, liquid, and solid phases [40]. The PA detection method offers several compelling features. For example, PA measurements can be performed without difficulties in collecting and detecting photons, common to fluorescence and Raman spectroscopies; as a result, no expensive photodetectors or optical filters are required. In addition, the PA detection has several other advantages, including simple and low-cost instruments, solid samples with long shelf life and higher sensitivity and lower LOD, therefore the integration of PA detection scheme with currently available commercialized immunoassay formats is of great clinical significance. By replacing the SA-HRP with SA-conjugated AuNP and removing the steps for TMB substrate and stop solution, the ELISA format was adapted to meet the needs of PA measurement. The AuNP acted as a reporter for the concentration of the analyte. When illuminated by a modulated laser beam, the AuNP would generate a PA signal that can be measured to quantify the concentration of the analyte. The PA technique generates quantitative signals based on a 3-step process involving AuNP optical absorption, conversion of the absorbed energy into heat, and the subsequent heat-induced thermal expansion of the adjacent media, which produces pressure oscillations or propagating acoustic waves when the incident beam is modulated at an acoustic frequency. As illustrated in Figure 8, the PA-based detection of AuNP-labeled biomarker takes place inside a sealed sample chamber, which is relatively small compared to typical acoustic wavelengths used for PA measurements. A

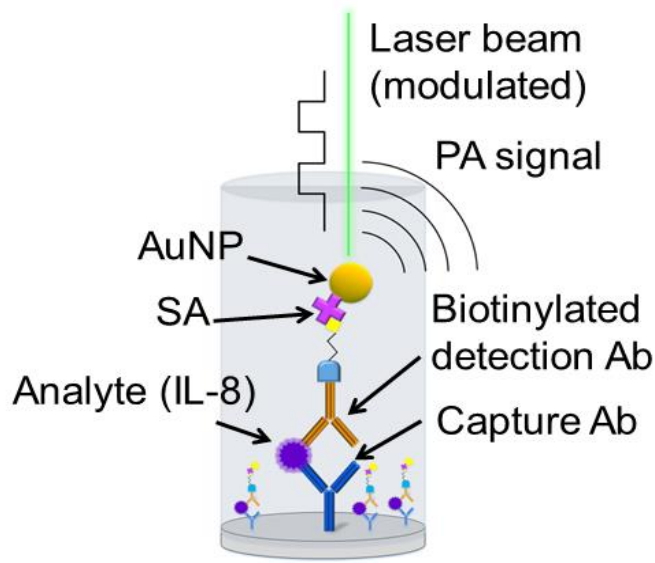


Figure 8. PA immunoassay format. A sandwich format is used for the immunoassay, wherein the analyte is immobilized by a capture antibody and tagged with a detection antibody, which is further tagged with a conjugated AuNP. The AuNPs generate a PA signal in the aforementioned setup, and the signal intensity reflects the concentration of the analyte [127].

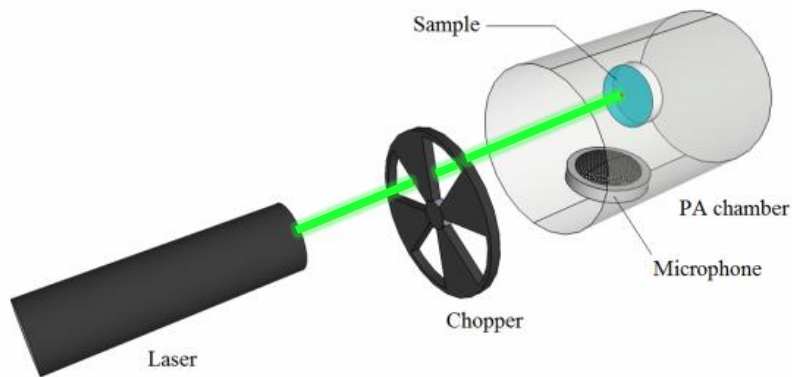


Figure 9. Optical setup for PA measurement. During a PA measurement, a chopper is used as the modulator, which periodically blocks the laser at 13 Hz. The sample placed in a sealed chamber is periodically heated and, therefore, periodically expands and contracts, generating a pressure oscillation that is detected by the microphone and displayed as a waveform on an oscilloscope [128].

modulated laser beam is used as the excitation source to generate pressure oscillations, and a microphone is installed inside the sample chamber to measure the signal, as shown in Figure 9.

Biotin-conjugated gold nanorods and SA-conjugated gold nanorods were purchased from Nanopartz, Inc. (Loveland, CO, USA). Polyvinylamine (PVAm; MW = 340 kDa) was obtained from BASF (New Jersey, USA) and diluted in water to obtain a 5% solid solution, which was used as the surface-functionalization material. Glutaraldehyde (GA), bovine serum albumin (BSA), SA (SA) protein, Tween-20, and phosphate buffered saline (PBS, 10 mM, pH = 7.4) were purchased from Sigma-Aldrich (St. Louis, MO, USA). The Human IL-8 ELISA Kit was purchased from Thermo Fisher Scientific (Waltham, MA, USA). The kit contained a monoclonal mouse anti-human IL-8 antibody (capture antibody), a recombinant human IL-8 protein standard, a human IL-8 biotinylated antibody (detection antibody), horseradish peroxidase-conjugated SA (SA-HRP), tetramethylbenzidine (TMB) substrate, and stop solution (0.16 M sulfuric acid).

2.2 Simulation of Gold Nanoparticles

2.2.1 Plasmonic resonance of gold nanoparticles

Finite difference time domain (FDTD) simulations were performed to characterize the optical responses of AuNPs on an acrylic substrate. FDTD simulation can be used to calculate the extinction spectrum and the near-field distribution at a spectral location for metal nanoparticles illuminated by the resonance wavelength [129]. In this work, the simulation domain included a single AuNP located on the surface of a flat polymer substrate. The optical properties of Au and acrylic substrate were taken from Palik's Handbook. The AuNP

was illuminated with a plane wave propagating in the z direction with the electric field polarized along the x -axis. The simulation region was truncated with periodic boundary conditions in the x and y directions, with perfectly matched layer boundary conditions in the z direction. Monitors were placed in close proximity to the boundaries to calculate the amount of reflected and transmitted power as a function of wavelength. A uniform fine mesh size of 1 nm (x , y , and z directions) was used around the AuNP region.

To generate a strong PA signal with AuNPs, the emission wavelength of the excitation laser should match the LSPR wavelength of the AuNPs. The LSPR of a single AuNP placed on top of a flat plastic substrate was numerically determined using FDTD simulation. The AuNPs used in this study had an axial diameter of 8 nm and a length of 12 nm and were immobilized at the air-substrate interface. The absorption spectrum of the single AuNP is shown in Figure 10, where the resonance peak was located at approximately 553 nm. At the resonance wavelength, the AuNP strongly absorbed the incident light and resulted in efficient heating of the surrounding air. To maximize the heating effect, a frequency doubled Nd:YAG laser ($\lambda = 532$ nm), whose wavelength was close to the resonance wavelength, was chosen as the excitation source. At the resonance wavelength, the near-field distribution across the AuNP was calculated, as shown in Figure 11, where the pseudo-color map represents the electric field intensity relative to the intensity of the incident field. The white line and the black ellipse indicate the surfaces of the plastic substrate and the AuNP, respectively. As shown, LSPR occurring in close vicinity to the AuNPs enhanced the near electric field by a factor of over 90-fold. The associated enhancement of optical absorption led to very strong heat generation that boosted the photothermal and photoacoustic effects.

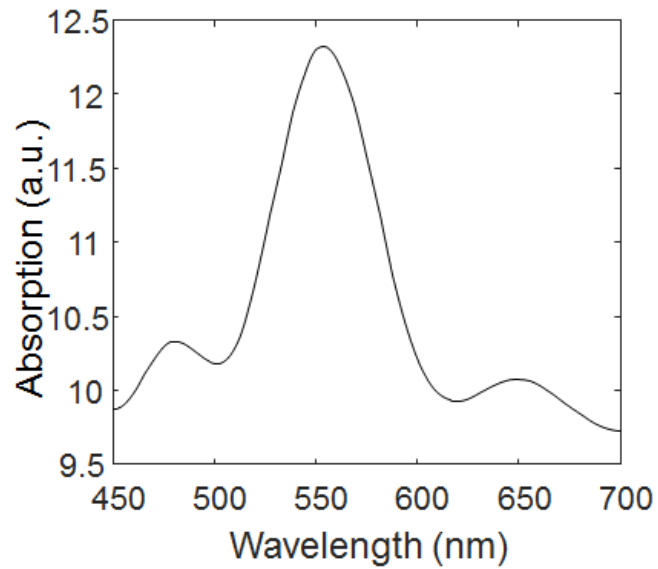


Figure 10. FDTD Simulated absorption spectrum of the AuNP. The localized surface plasmon resonance wavelength was around 550 nm, therefore a laser with a wavelength (532 nm) close to the resonance wavelength was chosen [127].

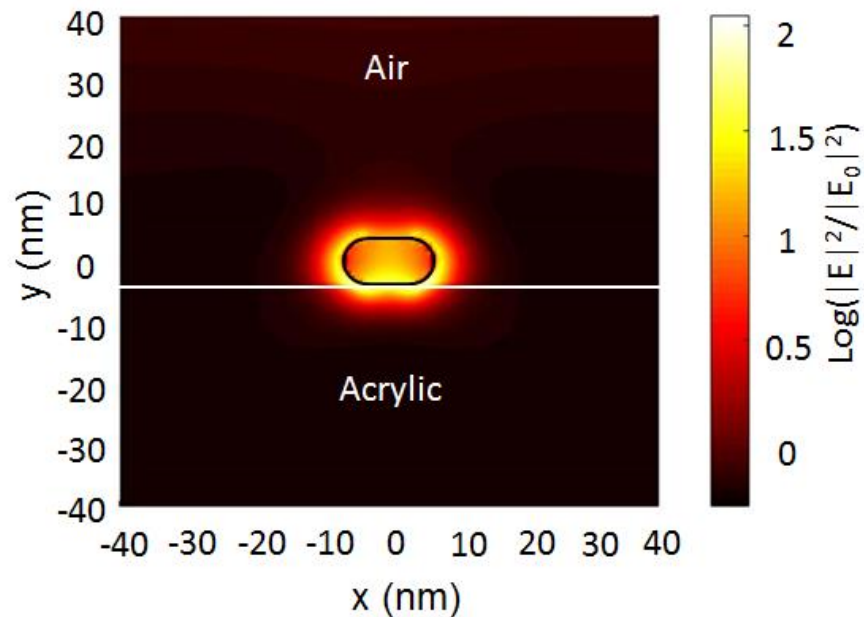


Figure 11. FDTD Simulated near field distribution of the AuNP. From the figure we can conclude that the near field intensity can be as high as 100 times higher than the incident optical field intensity [127].

2.2.2 Heat generation of gold nanoparticles

To quantitatively estimate the heat generation and temperature increase of AuNPs illuminated by radiation, we used COMSOL Multiphysics® to simulate the temperature distribution in the vicinity of an AuNP placed on a TiO₂ substrate in air. In this multiphysics simulation, the entire region of calculation is a rectangular cuboid. The dimension of x and y direction is 720 nm, from -360 to 360 nm, while the dimension for z direction is 900 nm, from -250 to 650 nm. A spherical AuNP with a radius of 100 nm is used in the simulation, its center located at the origin (0,0,0). At the top and bottom of the calculated region, we put perfect matching layers to completely absorb the electromagnetic (EM) radiation, with perfect electric conductor (PEC) condition set at planes $z = 400$ nm and $z = -400$ nm. The equation for the PEC is then:

$$\mathbf{n} \times \mathbf{E} = \mathbf{0} \quad (9)$$

where \mathbf{n} is the normal vector of the planes and \mathbf{E} is the electric field. At planes $x = 360$, $x = -360$, $y = 360$, $y = -360$, periodic boundary conditions are used, so that the simulation can be considered as a collection of AuNPs separated by a distance of 720 nm. The periodic boundary conditions can be expressed as:

$$\mathbf{E}_{\text{dst}} = \mathbf{E}_{\text{src}} e^{-ik_F(\mathbf{r}_{\text{dst}} - \mathbf{r}_{\text{src}})} \quad (10)$$

$$\mathbf{H}_{\text{dst}} = \mathbf{H}_{\text{src}} e^{-ik_F(\mathbf{r}_{\text{dst}} - \mathbf{r}_{\text{src}})} \quad (11)$$

An EM plane wave is set to be incident on the AuNP and the substrate from above along -z direction. The expression of the plane wave is described in Eq. 11:

$$\nabla \times (\nabla \times \mathbf{E}) - k_0^2 \varepsilon_r \mathbf{E} = \mathbf{0} \quad (12)$$

where ε_r is the relative dielectric constant of the medium. The wavelength of the radiation is set to be 569 nm, at the resonance wavelength of an AuNP with 100 nm in diameter. The

output power of the EM wave source is set at 7.776×10^{-5} W, and the surface area of the x-y plane in the calculated region is 360 by 360 nm, i.e. 5.184×10^{-7} mm². The power density is then 1.5×10^5 mW/mm², which corresponds to a 150 mW laser focused to a focal point of 34 μ m in diameter.

The aforementioned parameters and specifications have fully explained the EM part of the multiphysics simulation. The heat generation and transferring part of the simulation is as follows. A generalized heat transfer equation is a continuity equation containing heat source, thermal conduction, and flow of the substance:

$$\rho C_p \mathbf{u} \cdot \nabla T = \nabla \cdot (k \nabla T) + Q_e \quad (13)$$

where \mathbf{u} is the velocity of the substance, ρ is the density, C_p is the isobaric specific heat capacity, T is the absolute temperature, k is the thermal conductivity and Q_e is the heat source. Since the system is at steady state with nothing flowing, \mathbf{u} is zero everywhere, so Eq. 12 is reduced to:

$$0 = \nabla \cdot (k \nabla T) + Q_e \quad (14)$$

with $\nabla \cdot (k \nabla T)$ being the diffusion term and Q_e the heat source term. The heat source Q_e is generically expressed as:

$$Q_e = Q_{rh} + Q_{ml} \quad (15)$$

where Q_{rh} and Q_{ml} are contributions from electric current and magnetization, respectively:

$$Q_{rh} = \frac{1}{2} \text{Re}(\mathbf{J} \cdot \mathbf{E}^*) \quad (16)$$

$$Q_{ml} = \frac{1}{2} \text{Re}(i\omega \mathbf{B} \cdot \mathbf{H}^*) \quad (17)$$

Because there is no magnetic material in the simulation, \mathbf{B} and \mathbf{H} is always parallel, so Q_{mL} is zero, and contribution from electric current is the sole contribution to the heat generation.

The entire calculated region is thermally insulated from the environment:

$$-\mathbf{n} \cdot \mathbf{q} = 0$$

The simulation results are shown in Figure 12. The reference temperature is 293 K, therefore, the highest temperature change is $313 - 293 = 20$ K. Also from the temperature distribution, we can conclude that the TiO_2 substrate is a poor heat conductor because heat barely diffuses into the substrate. Almost all heat diffuses into the air. Such temperature distribution is very favorable for PA and PT detection, since air contributes to pressure oscillation and refractive index change much more greatly than the solid substrate at a given temperature, therefore, the diffusion of nearly all the heat into the air can cause a strong PA or PT signal.

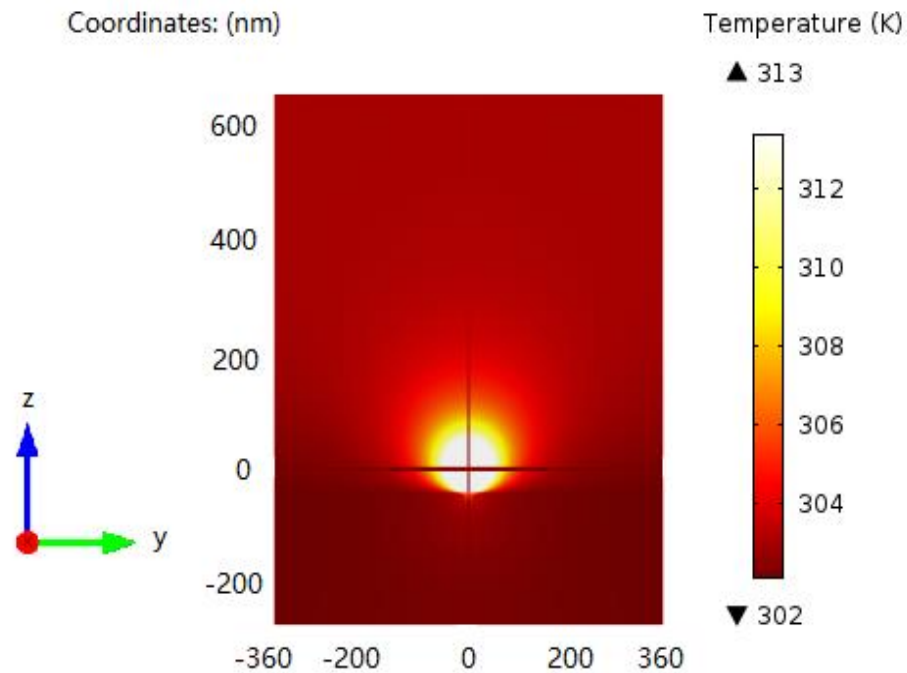


Figure 12. Temperature distribution of an AuNP under illumination of EM radiation. Nearly all the heat diffuses into the air, causing a strong PA or PT signal.

2.3 Instrumentation

The PA detection setup consisted of a frequency doubled Nd:YAG laser ($\lambda = 532 \text{ nm}$; $P_{\text{out}} = 50 \text{ mW}$), an optical chopper (SRS540, Stanford Research Systems), a PA detector (PAC 200, MTEC Photoacoustics, Inc.), and a data-acquisition device, as shown in Figure 13. The acrylic substrates were placed inside the PA chamber one at a time for PA measurements. After loading the sample, the chamber was sealed to eliminate ambient noises. For all PA measurements, the chopping frequency of the optical chopper was set at 13 Hz. The laser beam from the Nd:YAG laser passed through the optical chopper and a glass window in the PA chamber. The intensity-modulated laser beam was absorbed by the AuNPs on the acrylic substrate and caused periodic heating of the air inside the PA chamber. The thermal expansion and contraction cycles resulted in pressure oscillations within the PA chamber. An acoustic transducer, i.e., a microphone (4176, Brüel & Kjær A/S), was connected to the chamber to measure PA pressure oscillations. The output of the microphone was amplified by a preamplifier integrated inside the PA-detection system and was subsequently measured using an oscilloscope (TDS2014B, Tektronix) or a lock-in amplifier (SRS-850 DSP, Stanford Research Systems).

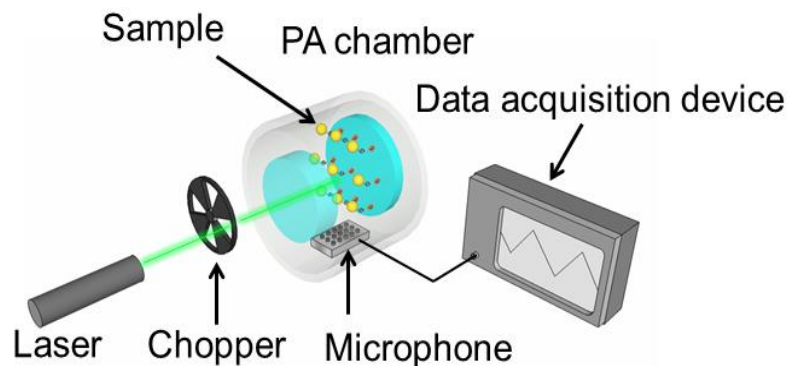


Figure 13. Optical setup for a PA immunoassay. The chopper modulated the laser in a square-wave manner, and a PA signal was generated and detected [127].

2.4 Assay Protocols

To validate PA detection as an effective method for protein analysis, we developed a proof-of-concept assay to measure SA concentrations (MW = 52.8 kDa). Acrylic windows were chosen as the substrate, owing to their low thermal conductivity and low cost. SA molecules were immobilized on an acrylic substrate and labeled using biotin-conjugated AuNPs to generate PA signals. The initial step in the assay was to coat the acrylic substrates using PVAm, which provided high-density amine functional groups on the plastic substrate. For the second step, the substrates were soaked in GA solution (25% in water) for 3 h, followed by a thorough wash with de-ionized (DI) water. GA molecules covalently attached to the PVAm. As a bifunctional linker, the GA treatment enabled the capture of protein molecules via their amine moieties. The third step of the protocol was to capture SA samples on the substrates. A series of SA samples with various concentrations were prepared in PBS buffer. The SA samples (50 μ L) were pipetted onto the acrylic substrates and incubated overnight, followed by 3 washes with PBS. Next, the unoccupied aldehyde functional groups were blocked by soaking the acrylic substrates in BSA solution (1 mg/mL) for 4 h, followed by a wash step. The final step of the assay was to label the immobilized SA using biotinylated AuNPs. The AuNP suspension was diluted to a concentration of 1×10^{12} NPs/mL and dispersed onto the acrylic substrates. After a 2-min incubation, the acrylic substrates were washed sequentially using DI with 0.05% Tween. The acrylic substrates were then dried under a stream of compressed air and placed in the measurement chamber for PA measurements.

As an example of biomarker analysis, the human IL-8 antigen was chosen as the target molecule because of its clinical significance, as it is related to inflammation, obesity,

and other diseases [21, 22]. Two sets of human IL-8 dilution series were measured using ELISA and PA immunoassays, respectively. The major steps involved in the immuno-sandwich assays are summarized in Figure 14. The assays were performed in a microtiter plate. The bottoms of the wells were coated with the IL-8 capture antibody and then blocked in a solution of BSA (1 mg/mL) in PBS for 1 h at room temperature. Colorimetric Standard curves were generated using a 2.5-fold dilution series of IL-8 antigen for a total of 7 antigen concentrations, from 1000 pg/mL to 4.096 pg/mL, and a blank (dilution buffer only). IL-8 samples (50 μ L) were incubated in microtiter plates at room temperature for 1 h. The substrates were then washed in PBS with 0.05% Tween (PBS-T), followed by an incubation with biotinylated IL-8-detection antibodies at 25 ng/mL in PBS-T for 2 h. Then, PBS-T was used to wash the samples and remove excess detection antibodies. For the ELISA measurements, 100 μ L of SA-HRP solution was added to each well for 30 min as the enzymatic label, followed by 3 washes with PBS-T. Next, 100 μ L of TMB substrate was added into each microwell, after which the TMB underwent a colorimetric reaction catalyzed by the HRP molecules. After a 30-min development, the reaction was stopped by the addition of 100 μ L of stop solution. The results were measured using a spectrophotometer (BioTek). To generate the standard curve, the difference between the absorbance at 450 nm and 550 nm was calculated for each antigen concentration. For the PA-immunoassay, the dilution series was extended down to 0.016 pg/mL and the detection antibody was labeled using SA-conjugated AuNPs, rather than the SA-HRP solution. After a 15-min incubation, the AuNP solution was removed, followed by 3 washes with PBS-T. Before the PA measurement, the samples were dried in air at room temperature.

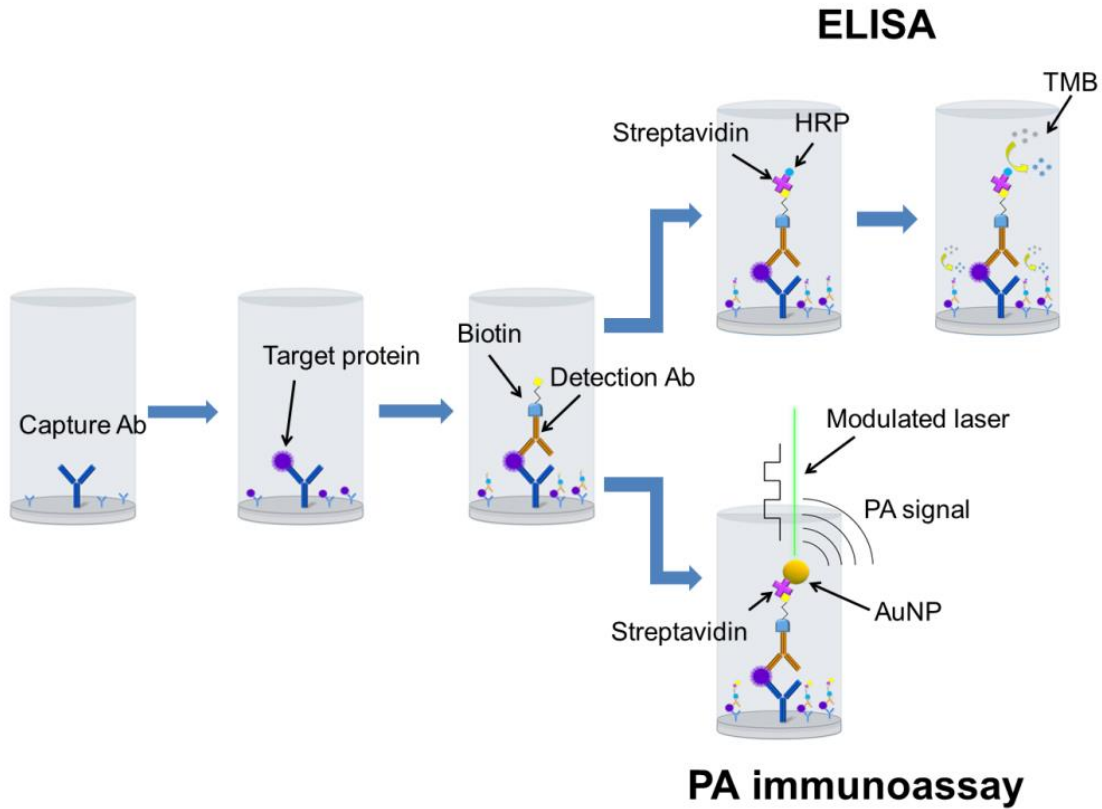


Figure 14. ELISA and PA immunoassay protocols. The PA immunoassay used SA-conjugated AuNP instead of SA-HRP and had no need to use a TMB substrate. The AuNP acted as the reporter of the concentration of the analyte [127].

2.5 Photoacoustic Detection of Protein

After identifying an optimal excitation wavelength, we performed a preliminary study of PA quantification of AuNPs absorbed on an acrylic substrate to demonstrate the feasibility of PA detection as an analytic method for plasmonic NPs. For this experiment, 7 AuNP suspensions were prepared by generating a dilution series, with AuNP concentrations of 1.0×10^{12} , 3.3×10^{11} , 1.0×10^{11} , 3.3×10^{10} , 1.0×10^{10} , 3.3×10^9 , and 1.0×10^9 NPs/mL. The AuNP samples (50 μ L) were pipetted onto the acrylic substrates and air-dried before PA

measurements were taken. Figure 15 shows the PA signals measured using an oscilloscope, as well as their fit to a logistic curve. The PA signal increased with the AuNP

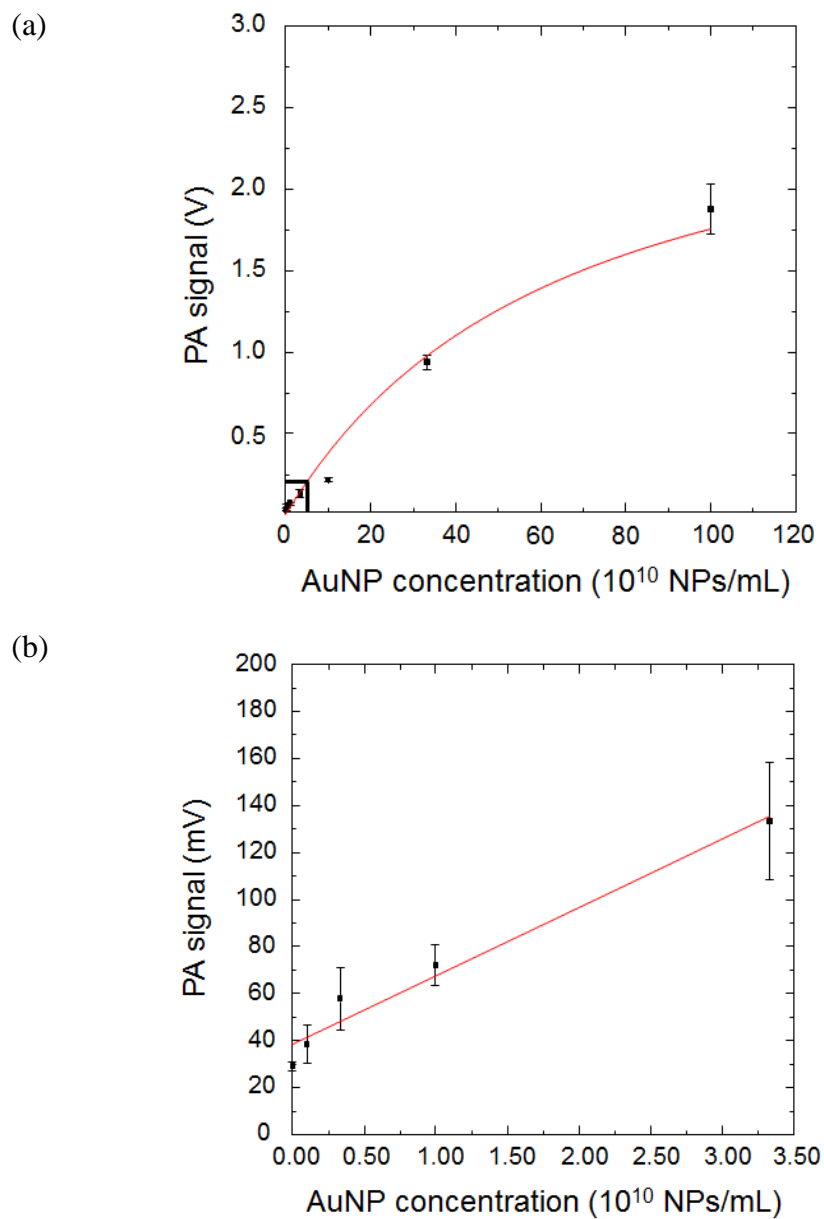


Figure 15. PA signal plotted with respect to AuNP concentration. (a) At higher concentrations, the PA signal started to saturate; (b) at lower concentrations, denoted by the black box in (a), the PA signal is largely linear to the AuNP concentration [127].

concentration. At lower concentrations, the PA signal showed a linear correlation with the AuNP concentration. At higher concentration levels, the PA signal became saturated. The noise level of these measurements was limited by the PA signal of the acrylic substrate (30 mV). As a proof-of-concept to demonstrate the utility of protein analysis using the PA method, a PA-based assay for the detecting SA was developed. To this end, PVAm-GA and biotinylated AuNPs were used as the SA receptor and the label, respectively. As shown in Figure 16, SA immobilization occurred on the PVAm- and GA-coated acrylic substrate. Then, SA samples were added to the substrates, using a series of SA concentrations (100, 25, 6.25, 4, 2, 0.8, or 0 $\mu\text{g/mL}$). The captured SA molecules were labeled using biotinylated AuNPs (1.0×10^{12} NPs/mL) through avidin-biotin binding, and thus, the PA signal generated by the AuNPs represented the SA concentration. The PA signals of the SA samples are shown in Figure 17. The linear range of the detection was in the range of 2–25 $\mu\text{g/mL}$. The PA signal approached saturation at an SA concentration of 100 $\mu\text{g/mL}$, because as the concentration of AuNPs gets higher, the distance between AuNPs gets closer and inter-particle interactions can no longer be neglected. These interactions may shift the localized surface plasmonic resonance peak and thereby decoupling the excitation laser from the resonance. There could also be agglomeration of AuNPs at high concentrations, and since the optical absorption properties these agglomerated AuNPs are very different from individual AuNPs, the resulting PA signal can be lower than expected from a linear trend. The LOD of the SA (2.7 $\mu\text{g/mL}$) was calculated as the PA background signal of the acrylic substrate plus 3 times its standard deviation. These results demonstrated the feasibility of the PA-based approach for protein quantification.

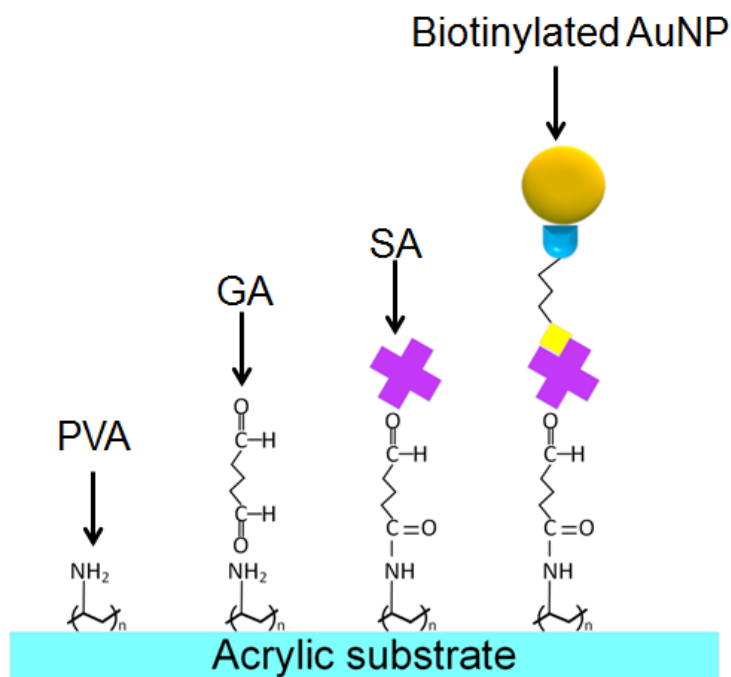


Figure 16. Schematic representation of the SA-measurement assay. SA was immobilized on an acrylic substrate pre-treated with PVAm and GA, after which it was labeled with biotinylated AuNPs [127].

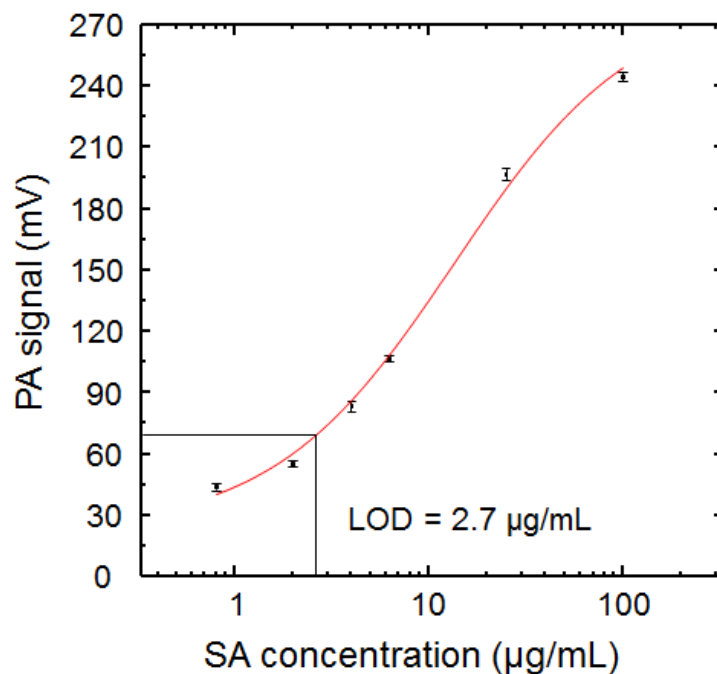


Figure 17. PA signal plotted against the SA concentration. The LOD was measured as 2.7 $\mu\text{g/mL}$ [127].

2.6 Photoacoustic Immunoassay of Protein Biomarker

To determine the performance of the PA immunoassay, the detection of a chemokine protein, human IL-8, was performed using the PA-immunoassay and the results were compared with those of the colorimetric ELISA. To generate a titration curve for IL-8, we prepared IL-8 samples at a series of 13 concentrations ranging from 1000 pg/mL to 0.016 pg/mL, with 2.5-fold dilutions. The colorimetric signals of the ELISA tests were measured using a spectrophotometer. Figure 18 shows the measured optical density as a function of the IL-8 concentration. The PA signals of the PA immunoassay test were measured using an MTEC detector and a lock-in amplifier. The lock-in amplifier effectively reduces random noise generated by the electronic components. The titration curve of the PA immunoassay is shown in Figure 19. The LOD of the PA immunoassay was approximately 0.16 pg/mL, which represents an improvement of more than two orders of magnitude compared with the ELISA result of 23 pg/mL.

According to clinical evaluations of serum IL-8 levels in healthy adults, the physiology concentration of IL-8 is approximately 30 pg/mL [130], which is just within the LOD capability of ELISA serum analyses, but the PA immunoassay developed in this study provides a lower LOD capability applicable to diseases such as bladder cancer. Data from a recent study suggested that the IL-8 secretion level is increased in patients with invasive bladder cancer, making IL-8 a potential biomarker for bladder cancer screening [131]. Urine analysis showed that the IL-8 concentration increased from 0 pg/mL to 128.43 pg/mL in samples from patients with bladder cancer. The sensitivity of the PA immunoassay for IL-8 detection is sufficiently high to enable accurate IL-8 determinations in either serum or urine samples.

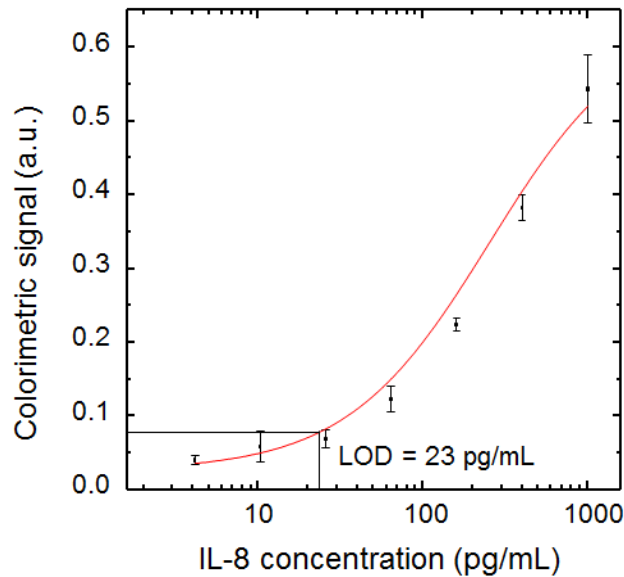


Figure 18. Colorimetric measurement results of the ELISA test for human IL-8. The colorimetric results were calculated based on differences between the optical densities at 450 nm and 550 nm. The data points were fitted using a logistic regression. The LOD of the ELISA measurement was calculated as 23 pg/mL [127].

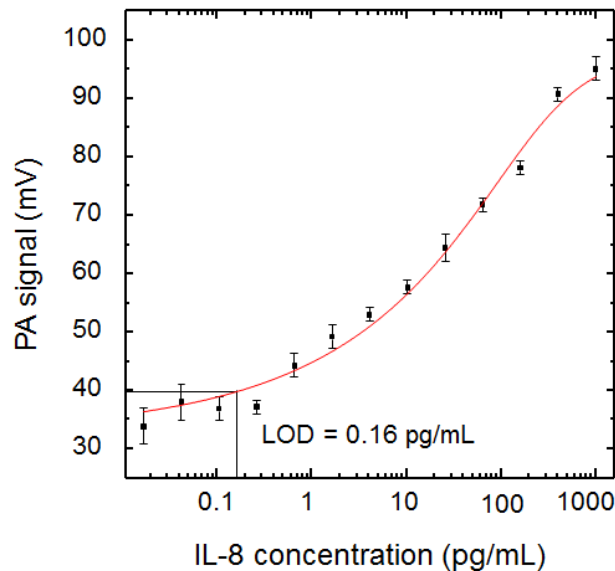


Figure 19. IL-8 titration curve generated using the PA immunoassay. The PA immunoassay showed a lower LOD (0.16 pg/mL) than did the ELISA [127].

In summary, to facilitate biomarker detection, we developed the PA immunoassay as a highly quantitative, sensitive, robust, and inexpensive analysis platform. The PA immunoassay can be used to quantify biomarkers, based on acoustic waves that are generated by the AuNP labels. The rationale for this approach lies in the advantages associated with efficient energy conversion that is enabled by the plasmonic nanoparticles, as well as the accuracy and simplicity of measuring acoustic signals. The use of photoacoustic detection also eliminates various types of noise, such as the leakage of excitation light through optical filters and the autofluorescence of commonly used materials, which can deteriorate the performance of most photon-based detection systems. The PA immunoassay was based upon the standard sandwich immunoassay, with AuNPs being used as the labeling material. An intensity-modulated laser beam at 532 nm was used to excite PA signal and the samples were measured in a sealed chamber. The PA-immunoassay results for human IL-8 detection demonstrated that the PA approach had significantly improved assay sensitivity (>2 orders of magnitude), compared to ELISA results (LODs of 0.16 pg/mL and 23 pg/mL, respectively). In addition to improved LOD, the PA immunoassay also offers advantages in terms of signal stability. The colorimetric signal of ELISA samples must be measured within 30 min after adding the stop solution. In contrast, the results of the PA immunoassay were stable over a long period of time, and multiple measurements can be taken without introducing problems such as bleaching or signal degradation.

The PA immunoassay is currently at an early stage and has great potential for further development. The PA immunoassay would be improved by further increasing the signal-to-noise ratio. This can be achieved by increasing the laser power to generate a stronger PA signal, optimizing the design of the PA chamber to better suit the purpose of PA

immunoassay, or using a compact microphone array to better collect the PA signal. Other means to improve the PA immunoassay would be to miniaturize the PA detection setup and to integrate the light source, PA chamber, and data acquisition and display into a single device that enables PA analysis for point-of-care testing. It may also be possible to reduce the LOD by reducing the background signal from the substrate and sample chamber. In addition, the PA immunoassay could be implemented using most existing protein-analysis formats, such as lateral and vertical flow assays, to become a versatile analytic tool.

The ELISA for human IL-8 is very accurate, with LOD around 25 pg/mL. However, it is a wet-lab type analytical assay that takes a long time, usually 4 hours, and requires a clean lab environment. It also requires a qualified professional to use for clinical purposes. Therefore it is not widely accessible to the public. To make such tests rapid and widely accessible, suitable for point-of-care analysis and home use, people have developed a simplified version of a sandwich immunoassay, called “lateral flow assay”. This assay is a paper-strip-based simple one-step assay that only takes about 15 minutes to finish, and it does not require a qualified professional to perform. The next section I will briefly introduce the background and working principle of LFA.

2.7 Acknowledgment

Parts of this chapter have been modified from my previous publication:

Zhao, Y., Cao, M., McClelland, J. F., Shao, Z., & Lu, M. (2016). A photoacoustic immunoassay for biomarker detection. *Biosensors and Bioelectronics*, 85, 261-266.

CHAPTER 3. PHOTOACOUSTIC LATERAL FLOW ASSAY

3.1 Principle of Lateral Flow Assay

Lateral flow assay provides rapid and simple detection of the presence or concentration of certain biomarkers. It is a low-cost and point-of-care assay. However, the sensitivity of currently available LFAs is far less than lab-based analytic immunoassays, such as ELISA. To overcome this drawback, we proposed the use of PA measurement of the intensity of the test line on the LFA paper strip.

To quantify the target analyte, PA detection relies on the light-induced acoustic signals [109, 132]. Regarding LFA tests, the PA method offers numerous compelling characteristics. For example, analytes in different phases over a substantial concentration range can be quantified. In addition, PA measurements can be performed without experiencing any difficulties with the collection and detection of photons that are common to reflection/transmission, fluorescence, and Raman spectroscopies; thus, expensive photodetectors and optical filters are not needed [110, 133]. When illuminated by a laser at the LSPR wavelength, AuNPs can efficiently heat the surrounding medium and generate acoustic waves [38, 134, 135]. One of my papers recently demonstrated that PA detection is capable of sensing less than 10 AuNPs within an area of $100 \mu\text{m}^2$ using an inexpensive instrument [98]. The implementation of PA detection for LFA tests using AuNPs as a label, where a laser-induced acoustic wave was employed as the sensing signal, is then a natural extension of the PA detection of AuNPs. The PA method benefits LFA tests in two aspects: the strong and reliable PA signal generated by the AuNPs and the reduced system noise due to the input and output signals residing in two different energy domains.

The LFA used in this work was for cryptococcal antigen (CrAg), which is an antigen indicative of cryptococcosis, a potentially fatal fungal disease, and is particularly fatal to patients with AIDS. Since the CrAg LFA used conjugated AuNPs as the labels, it could be easily quantified by PA measurements since AuNPs have strong optical absorption. As shown in Figure 20, in an LFA test, an aqueous sample is pipetted onto a paper strip, which contains antibody-conjugated AuNPs and other reagents (refer to the Experimental section). On the conjugation pad, the analyte binds to the AuNPs. The resulting analyte-AuNP complex wicks up the paper strip under the action of a capillary force and is captured at the test line, where the capture antibodies reside. The density of AuNPs at the test line reflects the concentration of the analyte. Meanwhile, a control line develops which indicates the proper flow of the sample. Currently, the colorimetric method is commonly used to estimate the density of AuNPs at the test line. Although the colorimetric analysis is simple, it is qualitative or semi-quantitative with a limited sensitivity and is, therefore, insufficient for the detection of some circulating disease biomarkers at low concentrations [136].

3.2 Development of Photoacoustic Detection Modality for LFA

To quantitatively measure the AuNPs in the test line, we used a PA-based approach. The PA technique generates quantitative signals based on a 3-step process involving the light absorption by a sample, conversion of the absorbed energy into heat, and the subsequent heat-induced thermal expansion of the adjacent media that generates pressure oscillations or propagating acoustic waves when the incident beam is modulated at an acoustic frequency. The intensity of the PA signal is proportional to

the concentration of the light absorbing material. PA spectroscopy has been successfully utilized to quantitatively analyze chemicals using thin-layer chromatography plates [137, 138]. One of the problems of PA detection of LFA is that the paper strip itself has an appreciable optical absorption, it will increase the background signal. And since this background cannot be consistent among different paper strips, it becomes a major source of noise that makes it difficult to measure low-concentration samples. To tackle this challenge, we implemented two different PA detection schemes for the analysis of AuNPs in LFA strips. One is the chop mode and the other is the scan mode. For both modes, the sample was first sealed in an MTEC PAC 200 PA unit to mitigate the influence of ambient noise. A microphone in the PA unit transformed the pressure oscillation generated by the sample to an electronic signal. The AuNPs I used in the verification test and those used in the CrAg LFA paper strips had a plasmonic resonant wavelength near 532 nm, so we chose a Mingnuo Optoelectronic NdYAG laser that had an output power of 50 mW at 532 nm. In the chop mode, the intensity of the laser beam was modulated by a chopper at a frequency of 13 Hz. This generated a square wave intensity modulation. The resulting PA waveform was a triangular wave at the same frequency, in which the rising edge corresponds to the on time of the square wave, and the falling edge corresponds to the off time of it. In the scan mode, the laser intensity was kept constant and the laser beam was scanned across the sample at a speed of 3 mm/s. The resulting waveform was an underdamped pulse.

Since the PA signal increases with the decrease of the modulation/scanning frequency, low values were chosen to enhance the signal-to-noise ratio of the

measurements. For both modes, the peak-to-peak amplitude value was defined as the PA signal. A Tektronix TDS 2014a oscilloscope was used to read out the PA signal. The scan mode can effectively eliminate the background PA signal generated by the substrate, therefore extend the limit of detection down to the pg/mL level. In the further study, a neutral density filter was used to test the influence of different laser intensities and a Melles Griot He-Ne laser at 632 nm was used to test the response of different wavelengths. In both cases the adjacent PA signal generation medium is air and PA signals, in the form of pressure oscillations, are detected by a microphone within a small volume (less than 1 cc) sealed chamber. The first scheme, i.e. the “chop mode”, employed an optical chopper to modulate the intensity of the excitation laser as shown in Figure 21. The resulting PA signals appeared as triangular waveforms, and the peak-to-peak value was used as the PA signal amplitude (Figure 23). We hypothesize that the amplitude of the PA signal reflects the concentration of AuNPs at the test line, which is proportional to the concentration of the analyte in the sample. As mentioned earlier, one of the problems of the chop mode is that the paper strip itself has an appreciable optical absorption that can generate a background signal (blue trace of Figure 23). And since this background generally varies from strip to strip, it becomes a major source of noise that makes it difficult to measure low-concentration samples. To tackle this challenge, we developed a new detection scheme called “scan mode” detection.

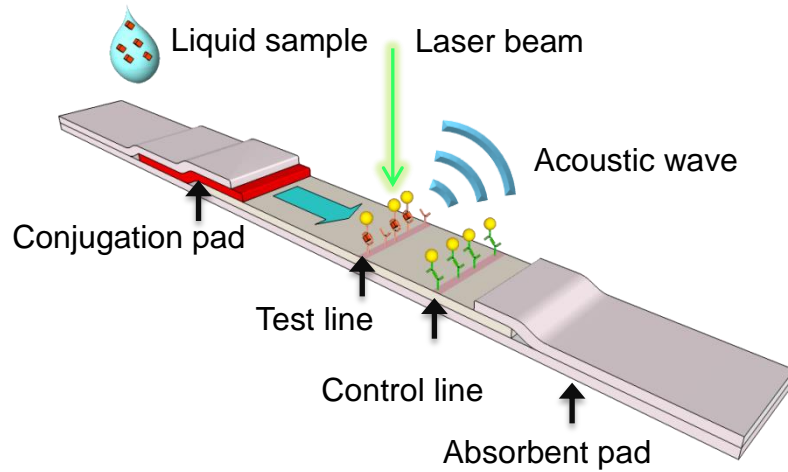


Figure 20. PA LFA working principle. The aforementioned LFA test procedures are followed by a PA measurement of the test line [49].

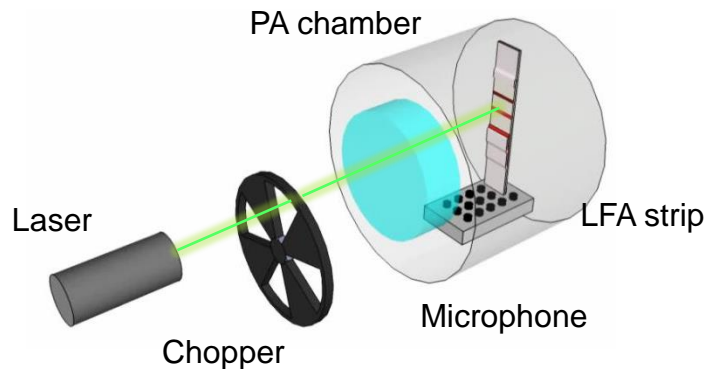


Figure 21. Optical setup for chop mode PA measurement [49].

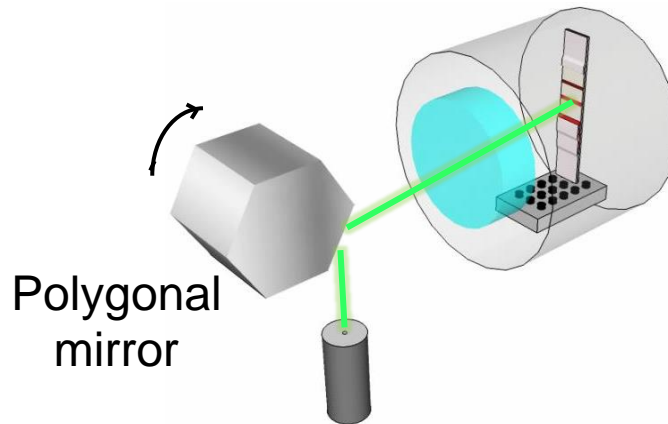


Figure 22. Optical setup for scan mode PA measurement [49].

In contrast to the traditional chop mode that is commonly used in most PA measurements, continuous wave laser beam is used in scan mode (Figure 22). The laser beam is scanned across the test line of the paper strip. Since the optical absorption of the paper substrate is nearly constant, as material properties within one strip can be considered as uniform, it barely generates a PA signal. This greatly reduced PA background signal (blue trace of Figure 24) from the paper strip. On the other hand, the optical absorption of the AuNPs at the test line is transient, meaning that it will experience a sudden illumination of the laser when the laser beam reaches it and a sudden termination of illumination after the beam has scanned across it. This results in a sudden heating and cooling of the AuNPs, hence a PA signal that contains only the contribution from the AuNPs is generated. Figure 21 and 22 shows the working principle as well as the optical setups for both chop mode and scan mode PA detection. In chop mode, the laser is modulated by a chopper, which is the same as in most PA applications; whereas, in scan mode, the laser is scanned across the test line by using a rotating polygonal mirror, as shown in Figure 22.

To test the performance of the newly proposed scan mode PA detection, we compared the PA signals obtained using chop mode and scan mode measurements for three concentrations of AuNPs dispersed on a porous substrate. Figure 18 shows the results of the measurements. The three concentrations used were 1×10^{11} NPs/mL, 3.3×10^{10} NPs/mL, and a control sample with a concentration of 0. A CW Nd:YAG laser ($P = 50$ mW, $\lambda = 532$ nm) and a commercial PA chamber (PAC-200, MTEC Photoacoustics Inc.) were used for both modes of PA signal detections. In the chop mode, a modulation frequency of 13 Hz was used. For the scan mode, the scanning speed of the laser beam was fixed at 3 mm/s.

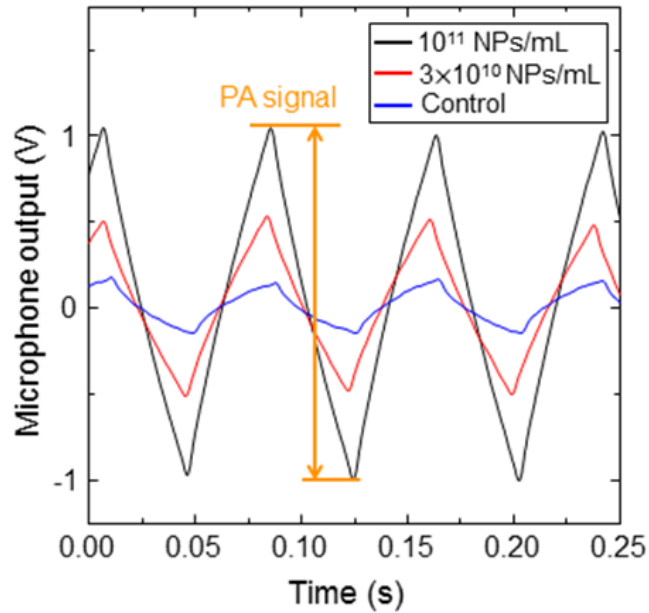


Figure 23. PA waveforms for AuNPs absorbed in a porous substrate measured using chop mode. The chopping frequency was 13 Hz and the peak-to-peak values were used as the PA signals. A background signal of 0.3 V for the control sample is observed [49].

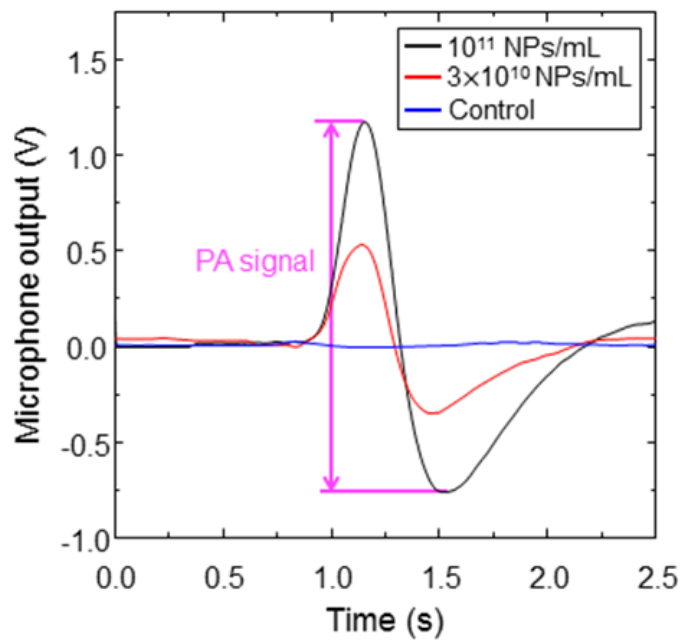


Figure 24. PA waveforms for AuNPs absorbed in a porous substrate measured using scan mode. The scanning speed was 3 mm/s and the peak-to-peak values were used as the PA signals. The background signal is almost zero [49].

The waveform of the chop mode detection is a triangular wave whose amplitude is related to the concentration of the sample. The peak-to-peak value is defined as the PA signal. The waveform of the scan mode, however, is an underdamped pulse, whose peak-to-peak value is also defined as the PA signal. From the comparison, we can see that the PA signal of the control sample differs significantly between these two methods. In the chop mode, the control sample has a background signal as strong as 0.3 V, which is equivalent to the PA signal generated by a 1×10^{10} NPs/mL sample of AuNPs when measured in scan mode. This makes the chop mode unable to yield a credible result when measuring samples whose concentrations are less than 1×10^{10} NPs/mL. The scan mode, on the other hand, can effectively suppress the background signal generated by the LFA paper strip, therefore minimize the background noise.

3.3 PA measurement of AuNPs on a Porous Substrate

Before the measurement of CrAg concentration, a preliminary test was run to validate the effectiveness of PA quantification of AuNPs dispersed on porous substrates made of polyvinylidene difluoride (PVDF). The preparation of AuNP samples was as follows: We used AuNP suspension in water from Nanopartz and made a dilution series that contains the following concentrations (in NPs/mL): 1×10^{12} , 3×10^{11} , 1×10^{11} , 3×10^{10} , 1×10^{10} , 3×10^9 , 1×10^9 and 0 (control). Each concentration had three duplicates. The size of the colloidal AuNPs is 40 nm with the size distribution of $CV < 10\%$. In this work, 20 μL of each sample was dipped onto a piece of PVDF membrane and dried for 15 minutes. After drying the samples were ready for further measurement. Images of the AuNPs dipped on PVDF membranes were taken by a digital camera without flash light, as shown in Figure 25 (a). The

images were analyzed using ImageJ (an open source image processing program). The type of the images was RGB color. The images were first split into three channels, i.e. red, green and blue. In the substrate, the AuNPs exhibits a strong absorption in the range of 500 - 600 nm. Since the absorption peak of the AuNP used in this work is in the green color wavelength range, we chose the green channel to analyze visual contrast. The brightness of each pixel in the green channel is represented by a number from 0 to 255, with a larger number representing a brighter pixel. To analyze a sample, we first selected an area within the region where AuNPs were present on its corresponding image, and used the “Measure” function to get the average brightness; then we did the same for an area on the substrate (where there was no AuNP present). Then the visual contrast of the sample was calculated as the difference between the average brightness of the substrate and the average brightness of the AuNPs. We repeated the above steps for all the samples and got a visual contrast for each sample. The results of the test are shown in Figure 25 (b), where the results of chop mode PA, scan mode PA and scattering intensity obtained by analyzing the photos of the samples with the software ImageJ are plotted against the AuNP concentration. The results show that the dynamic range for visual contrast measurement was found to be from 3×10^{10} NPs/mL to 10^{12} NPs/mL for AuNPs on PVDF membranes. The scan mode PA detection has the largest linear range, from 1×10^9 to 1×10^{12} NPs/mL, due to the elimination of background signal of the PVDF membrane; while the performance of the scattering intensity measurement is the lowest, because the ImageJ analysis is very susceptible to ambient light noise, which lowers the accuracy dramatically at low analyte concentrations. The large linear range of the scan mode PA detection indicates the potential of achieving high sensitivity and low LOD if this method is applied to LFA measurements.

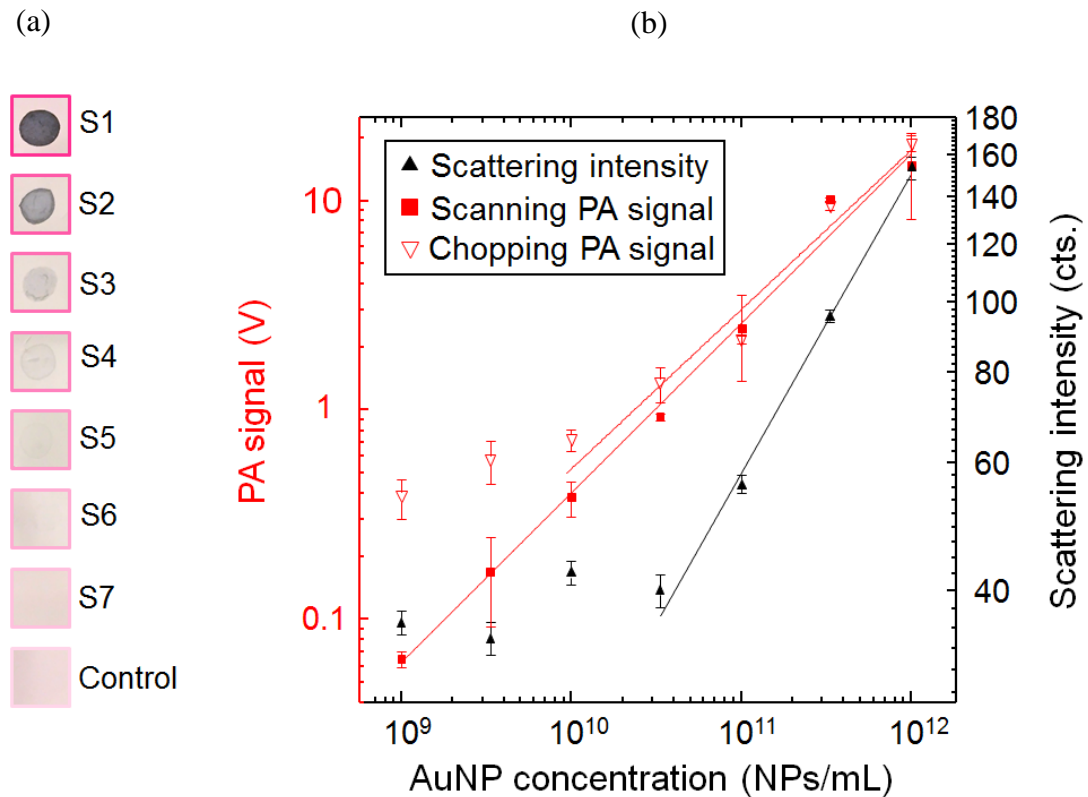


Figure 25. Comparison between PA-based detection methods and colorimetric analysis for AuNPs on porous substrates. (a) Optical images of the AuNP coated PVDF porous membranes with AuNPs in a two-fold dilution series. (b) Dose response curves of AuNPs on a PVDF membrane, obtained using three different detection methods. Both the signal response and the AuNP concentration are plotted on a logarithmic scale. Within the proper sensitivity ranges, the data points were fitted using a linear function for three data sets [49].

3.4 PA LFA Detection of Infectious Disease Biomarker

Assured by the feasibility study, the PA-based LFA tests were demonstrated by using cryptococcal antigen (CrAg) as an example. For patients infected with human immunodeficiency virus (HIV), cryptococcosis is a fatal fungal disease. The detection of CrAg in a human body fluid sample can enable a definitive diagnosis of the cryptococcosis [139].

Here, PA-based detections are applied to quantify CrAg using a Food and Drug Administration (FDA)-approved LFA kit (IMMY Inc.). As shown in Figure 3, the lateral flow device is relatively simple in construction, composed of a dipstick-shaped membrane with (1) AuNP-conjugated, anti-*Cryptococcus* monoclonal antibodies and AuNP-conjugated, control goat IgG antibodies deposited at one end of the membrane, (2) a control line with immobilized bovine anti-goat IgG antibodies deposited near the other end of the membrane, and (3) a test line with immobilized anti-*Cryptococcus* monoclonal antibodies in between. The analysis is done by placing an LFA dipstick in a centrifuge vial, with the end deposited with AuNP-conjugated antibodies submerged in the specimen, allowing the wicking up of the specimen together with the AuNP-conjugated antibodies. If *Cryptococcus* antigen is present in the specimen, it will bind to the AuNP-conjugated, anti-*Cryptococcus* monoclonal antibodies. The complex will continue to wick up the membrane until it reaches the test line. A sandwich of the AuNP-conjugated *Cryptococcus* antibody-antigen complex and the immobilized anti-*Cryptococcus* antibody is created, thereby capturing the complex, causing the accumulation of AuNPs and the development of a visible line at the test line. If proper flow occurs and the reagents are active at the time of use, the wicking of any specimen, whether it contains CrAg or not, will result in the AuNP-conjugated control antibody to wick up to the control line, where it is captured by the immobilized anti-goat antibody, causing the development of a visible line at the control line that indicates the validation of the test. The final result of the test is that a positive specimen will create both a test line and a control line, and the blackness of the test line reflects the

concentration of the CrAg in the specimen; a negative specimen will create only a control line. If the control line fails to develop, then the test is invalid.

In our work, CrAg samples are prepared in a dilution series that contains the following concentrations (in ng/mL): 100, 50, 25, 12.5, 6.25, 3.125, 1.563, 0.781, 0.391, 0.195, 0.098, 0.049, 0.024, 0.012, and 0.006. Each concentration had three duplicates. In a test, an LFA paper strip was placed in each vial containing the samples and was incubated for 10 minutes at room temperature. Then the strips were taken out of the vials and dried at room temperature for 15 minutes. After drying the samples were ready to be measured.

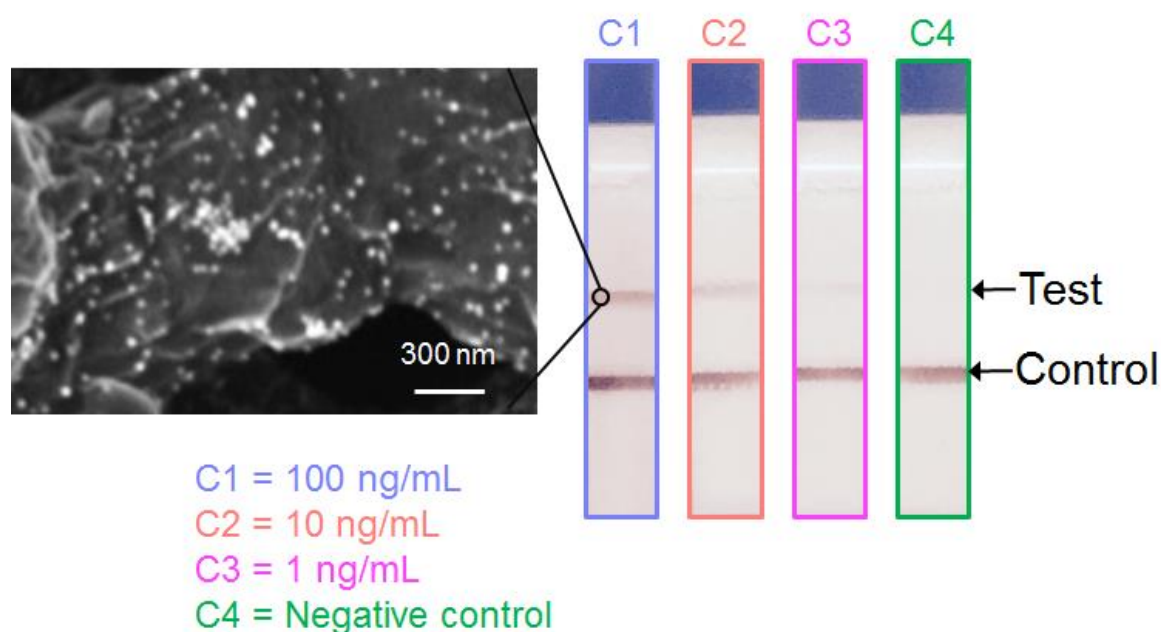


Figure 26. Photos of the LFA paper strip with 4 different analyte concentrations. The SEM image shows the presence of AuNPs at the test line [49].

Figure 26 shows the photos of four LFA paper strips after the control and test lines were fully developed. The colloidal AuNPs absorbed on the nitrocellulose fiber at the test line were illustrated by a scanning electron microscopy (SEM) image. For colorimetric

analysis, the pictures of the paper strip for each CrAg sample concentration were taken and analyzed using ImageJ. The PA signals from the test line on each paper strip were measured using the previously described system. The dose-response curves of the colorimetric analysis, the chop mode, and the scan mode PA detection are compared in Figure 27. To quantitatively evaluate the performance of each detection method, the measured dose response results are fitted using the 5-Parameter Logistic (5-PL) fitting formula:

$$y = A_{\min} + \frac{A_{\max} - A_{\min}}{\left(1 + \frac{x^{-h}}{x_0}\right)^s} \quad (18)$$

where A_{\min} is the lower asymptote, A_{\max} is the upper asymptote, x_0 is the dose where the response is halfway between bottom and top, h is the hillslope, and s is a control factor. The fitting was done using Origin 9.0.

The limits of detection (LODs), at which the signal intensity was equal to the control signal plus three times the standard deviation of its replicates, were identified using the fitting curves. The colorimetric method, chop-mode, and scan-mode PA detection exhibited the LODs of 1.1, 0.57, and 0.01 ng/mL, respectively. The results clearly show that both the PA-based methods provided a more sensitive and quantitative analysis than the conventional approach. In particular, the LOD of the scan mode PA measurement was approximately 100 times lower than that of the colorimetric method.

Two additional experiments were performed to study how the power and the wavelength of the excitation light affected the PA signals. Using the scan mode PA approach, the samples for the CrAg titer were measured again under a different excitation condition. First, the output power of the 532 nm Nd:YAG laser was reduced to 5 mW using a neutral density filter.

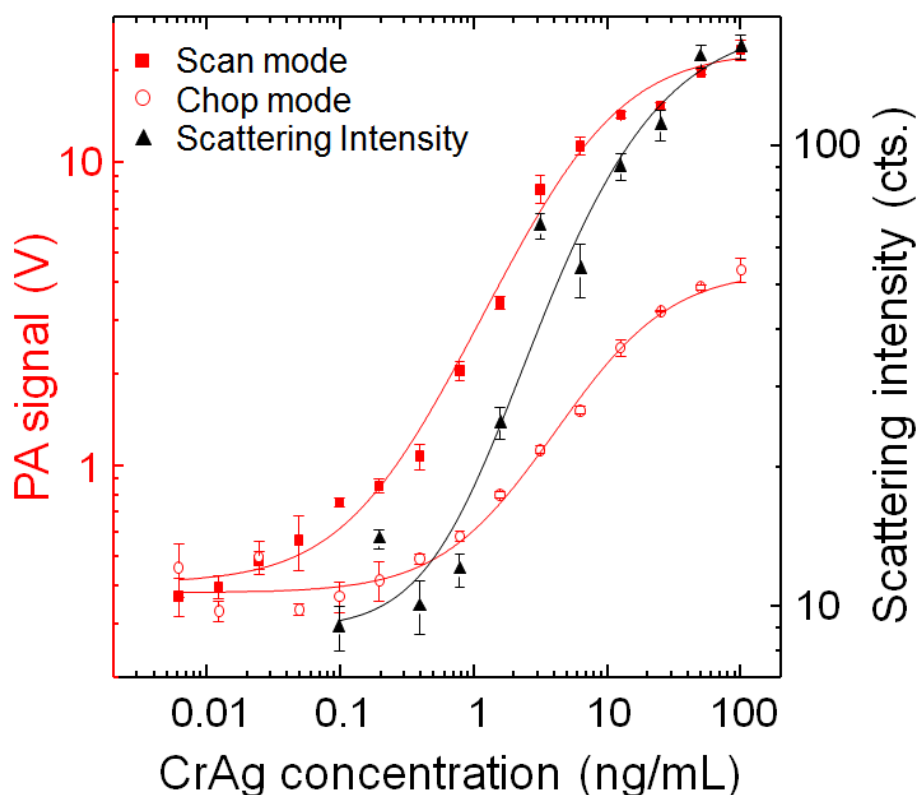


Figure 27. Dose response curves for the chop mode, scan mode, and scattering intensity measurements. The LODs for the colorimetric readout, the chop-mode and the scan-mode PA measurement, were calculated as 1.1, 0.57 and 0.01 ng/mL, respectively [49].

Figure 28 compares the dose-response curves for the CrAg titer measured using 50 and 5 mW outputs. The PA signals decreased approximately 10-fold when the excitation intensity was reduced by a factor of 10. The change was expected, as the PA signal should be proportional to the intensity of the excitation light. On the other hand, a 50 mW excitation does not produce a lower LOD. For the LFA test of CrAg, the detection sensitivity is limited by the assay, rather than the laser power in the 5 to 50 mW range.

The LSPR mode of AuNPs varies with their surrounding medium and their distribution. Therefore, the absorption capability of AuNPs is wavelength dependent.

Therefore the effect of the laser wavelength was investigated on the measurement of AuNPs embedded in a porous paper substrate. The same dilution series of LFA strips were measured using the green laser and a HeNe red laser at 632.8 nm; both lasers had an output power of 5 mW. The PA signals were measured in the scan mode. As shown in Figure 29, the PA signals did not change significantly with respect to the excitation wavelength. There were subtle differences between the results for the two lasers. At concentrations below 1 ng/mL, the PA signals excited by the green laser were stronger, as the LSPR mode of well-dispersed AuNPs has a resonance wavelength near 532 nm. On the other hand, the PA signals for the samples with concentrations over 1 ng/mL were stronger when the red laser was used. This was mainly caused by an increase in contribution from the inter-particle resonance coupling because the average distance between AuNPs was smaller at higher concentrations and hence the inter-particle resonance was stronger.

To summarize, a new PA detection method was demonstrated to improve the sensitivity of LFA tests. In contrast to the semi-quantitative colorimetric analysis, the PA method enabled the quantitative and sensitive detection of a low concentration analyte using LFAs, owing to the strong LSPR of AuNPs and the effective elimination of a PA background signal associated with ambient light noise. Two types of PA measurement schemes were implemented, that modulate the laser light absorption in different ways. With scan-mode PA detection, the light absorption was modulated spatially and was specifically designed to enhance the PA signal from the test line on standard LFA strips. This customized PA detection scheme effectively minimized the

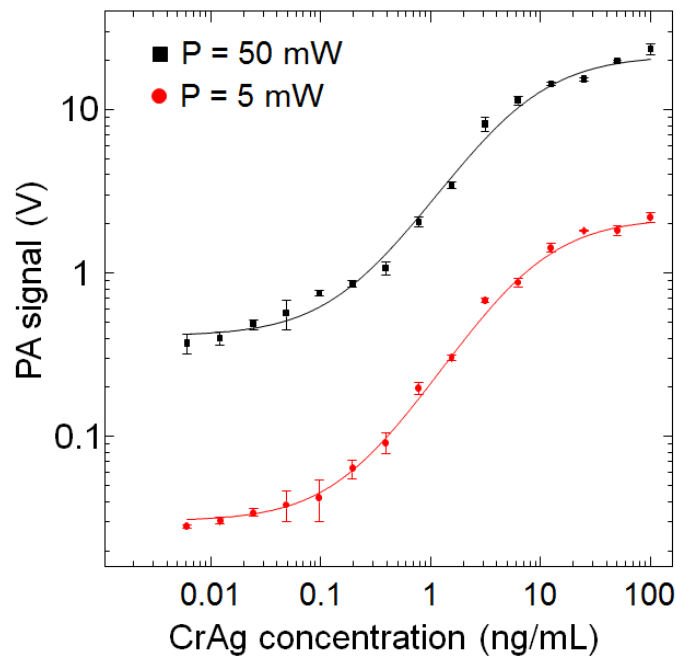


Figure 28. Effects of laser output on the PA signal of the LFA samples. PA signals have a linear relationship with the laser output [49].

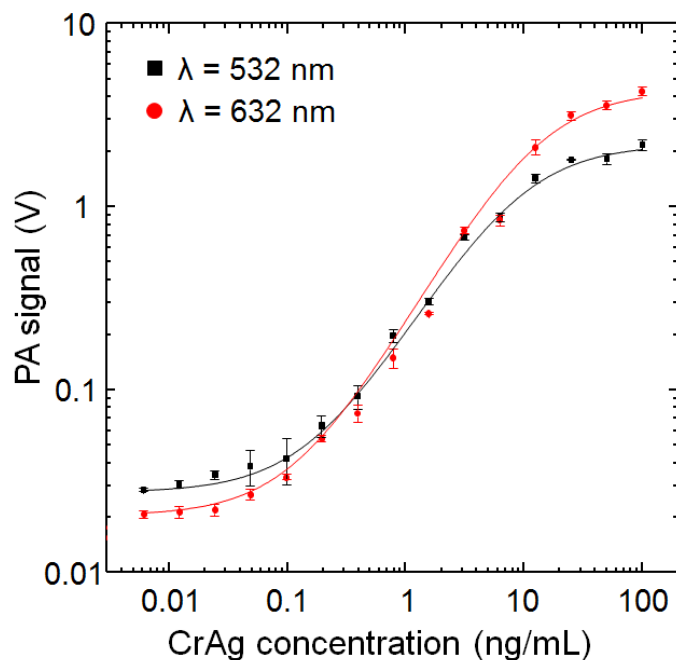


Figure 29. Effects of laser wavelength on the PA signal of the LFA samples. The red laser yielded a lower signal at low concentrations but a higher signal at higher concentrations than the green laser. Since we are more interested in detecting the biomarker at lower concentrations, we chose the green laser as our light source [49].

background signal arising from the paper substrate. The PA-based LFA was applied for the detection of CrAg using an FDA-approved LFA kit. The minimal detectable concentrations of the analyte for colorimetric measurements, chop-mode PA detection, and scan-mode PA detection were 1.1, 0.57, and 0.01 ng/mL, respectively. The PA method was capable of decreasing the detection limit of the CrAg detection by a factor 100. It is worth noting that this factor is characterized using standard CrAg samples. A follow-up research based on the current progress can be carried out by applying the PA-based LFA test to measure patient samples with the potential of reducing the LOD of paper-based sensors to the physiological concentration range of cytokine biomarkers in human serum [38]. The simple and low-cost PA-based LFA will be valuable for in-vitro diagnosis of early stage diseases using a drop of blood collected by a finger prick. Such a capability currently requires a laboratory-based approach, such as an enzyme-linked immunosorbent assay. Here, the PA apparatuses were developed using the off-the-shelf components. There is plenty of room to miniaturize the size and reduce the cost of the detection system for the application in resource-limited settings. For example, the laser source can be replaced using a LED that emits in the absorption band of the AuNP and the light source, microphone, and readout circuit can be fully integrated with the detection chamber into a palm-size box. The projected system cost will be below \$50 including the cost of a LED, a silicon MEMS microphone, a PA chamber, and a circuit board.

Furthermore, the tremendous progress in paper-based microfluidics enables the detection of multiple analytes [140]. A panel of biomarkers associated with a complex disease, such as cancer, can be simultaneously measured using one LFA strip, by

creating multiple lanes separated by hydrophobic barriers. In addition, recent developments in paper-based synthetic biology provide an alternative method to the antibody-antigen binding to deal with a wide variety of chemical and biological substances [141]. Together with these new advancements, PA-based LFA will enrich the applications of LFAs in the field of point-of-care disease diagnostics, food safety, and environmental monitoring.

3.5 Acknowledgment

Parts of this chapter have been modified from my previous publication:

Zhao, Y., Huang, Y., Zhao, X., McClelland, J. F., & Lu, M. (2016). Nanoparticle-based photoacoustic analysis for highly sensitive lateral flow assays. *Nanoscale*, 8(46), 19204-19210.

CHAPTER 4. PHOTONIC CRYSTAL ENHANCEMENT OF PA DETECTION

4.1 Structure of PC Substrates

A cross-sectional diagram (not to scale) of the PC structure adopted for the PA experiment is shown in Figure 30. The one-dimensional (1-D) PC, comprised of a linear grating surface structure, was fabricated using a nanoreplica molding process approach that has been described in detail previously [142]. Briefly, a silicon mold bearing a grating pattern was fabricated by electron-beam lithography and reactive ion etching, with a surface area of $2 \text{ mm} \times 2 \text{ mm}$. Liquid ultra-violet curable epoxy (UVCP, NOA 85, Norland Product Inc.) was squeezed between the silicon mold and a transparent acrylic film. Then it was solidified by exposing to UV light through the plastic substrate. Once separated from the silicon mold, the substrate film with the cured epoxy (refractive index, $n_{UVCP} = 1.46$) carried a grating pattern with a period of $\Lambda = 400 \text{ nm}$, a duty cycle of 60%, and a depth of $d = 60 \text{ nm}$. The grating surface was coated with a 100 nm titanium dioxide (TiO_2) dielectric film using an electron beam evaporator. The TiO_2 thin film (refractive index, $n_{\text{TiO}_2} = 2.0$) provided light confinement for the GMRs. The design parameters were chosen to maximize the strength of optical resonance at the excitation wavelength and to provide strong local field intensity at the PC surface.

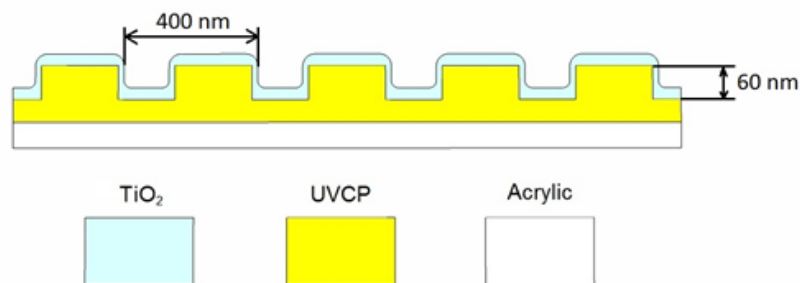


Figure 30. Cross-sectional view of a 1-D PC [98].

4.2 FDTD Simulation of Near-Field Distribution of AuNPs on PC

Having demonstrated the PA signal enhancement by PC substrate in the detection of organic light-absorbing molecules, we next exploited the PC resonance for the PA detection of metal nanoparticles (NPs) immobilized on the PC surface. Due to the localized surface plasmon resonance, the metal NPs exhibited tunable absorption in visible and near IR wavelength range [59]. Finite difference time domain (FDTD) simulation was utilized to calculate the near field distributions upon the PC sensor, which was coated with metal nanoparticles. The cross-sectional views of electric field intensity for a gold nanoparticle (AuNP) on a flat acrylic substrate, a blank PC sensor, and an AuNP on PC sensor are shown in Figure 31. The dimensions of the simulated PC structure are specified in Figure 30 and the gold nanoparticle has an axial diameter of 25 nm and length of 60 nm. In the FDTD simulation, the incident field was set as a plane wave propagating towards the PC surface at the resonant wavelength of $\lambda_r = 632$ nm and the coupling angle of $\theta_r = 0^\circ$. The periodic boundary conditions were used in the grating plane to define the computational region. The scale bars on the right side represent resonant electric field intensity ($|\mathbf{E}|^2$) levels normalized with respect to the incident electric field intensity. As shown in Figure 31, the evanescent resonance. Figure 32 compares the calculated absorption spectrum of AuNPs on PC and acrylic substrates. At the resonant wavelength, the absorption of AuNPs on the PC substrate becomes 60 times stronger than the same AuNPs on the planar acrylic substrate.

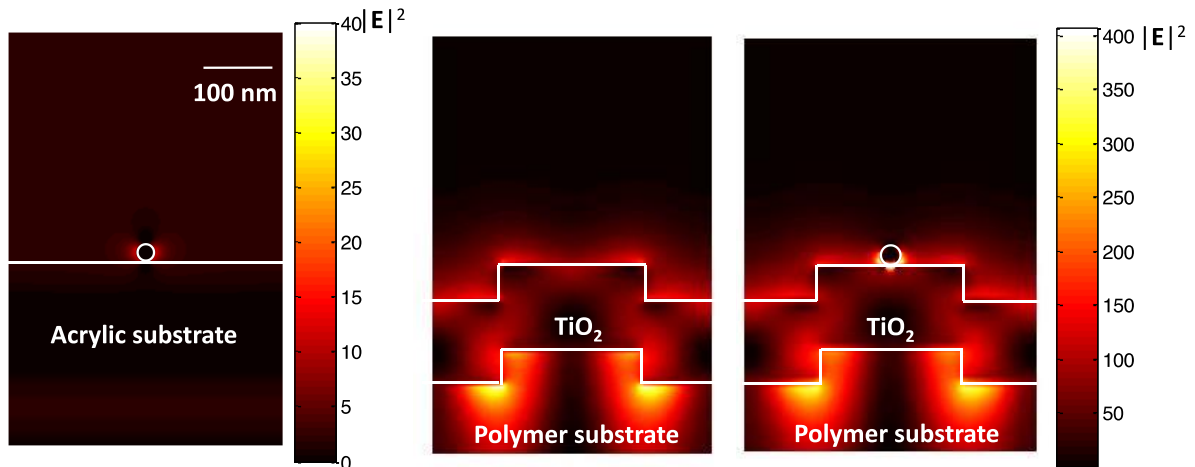


Figure 31. FDTD simulation of the enhancement effect of a PC substrate on AuNPs dispersed on its surface. From left to right: spatial distribution of the simulated near-field intensity within a single period of the PC grating, for an AuNP on a flat acrylic substrate, a blank PC substrate, and an AuNP on a PC surface, respectively. The upper horizontal white lines indicate the substrate surfaces and the white circles represent the surface of the AuNP [98].

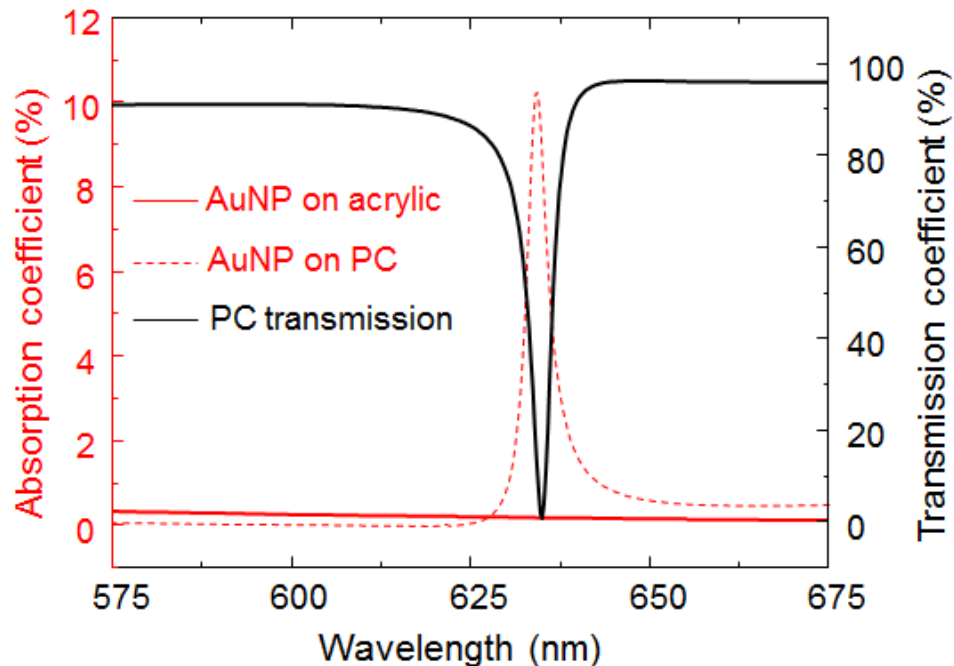


Figure 32. Calculated absorption spectra of AuNPs on acrylic and PC substrates. The modeled transmission spectrum shows the correlation between the GMR mode and the enhanced optical absorption of AuNPs on the PC sensor. The surface density of the AuNPs is $6.25 \text{ NPs}/\mu\text{m}^2$ [98].

4.3 Instrumentation for PC Enhanced PA Measurement

A schematic of the detection instrument is shown in Figure 33. The setup consists of a HeNe laser source with emission at $\lambda = 632.8$ nm, an optical chopper, a tunable mirror (M1) mounted on a translation stage, a convex lens, a second mirror (M2), and a PA analysis module (PAC 200 MTEC Photoacoustic Inc.) that incorporates the PC substrate. During the test, the output power of the HeNe laser was kept at 5 mW. The chopper modulated the laser emission with a square wave pattern at a frequency of 13 Hz. To excite a GMR at the desired wavelength (632.8 nm), the excitation light should illuminate the PC substrate at a specific angle of incidence. In the system, the mirror (M1) and the convex lens were utilized to tune the incident angle, defined in the direction perpendicular to the orientation of the grating. The convex lens with a focal length of 150 mm was fixed at a position so that its focal point was exactly on the sample. Translation of the M1 enabled adjustment of the incident angle from -7.2° to 7.2° . As the excitation light was efficiently coupled into the GMR, the intensified near field on the PC surface occurred and consequently generated a stronger photothermal effect.

The PA detection experiments require a sealed chamber to eliminate the ambient vibration noise. To combine the PC and the chamber, we attached the PC sensor onto an acrylic window that sealed the chamber with the PC facing the inside of the chamber. An acoustic transducer, a microphone (4176, Brüel & Kjær A/s), was connected to the chamber to measure photoacoustic pressure oscillations. During the experiments, light absorbing materials coated on the PCs absorbed light energy and generated pressure oscillations in the chamber due to absorption-induced heating. These pressure oscillations were converted to a voltage output by the microphone and were subsequently quantified using an oscilloscope

(TDS2000, Tektronix). In the experiment, PA outputs were calculated by averaging voltage amplitudes in the waveforms obtained from the oscilloscope.

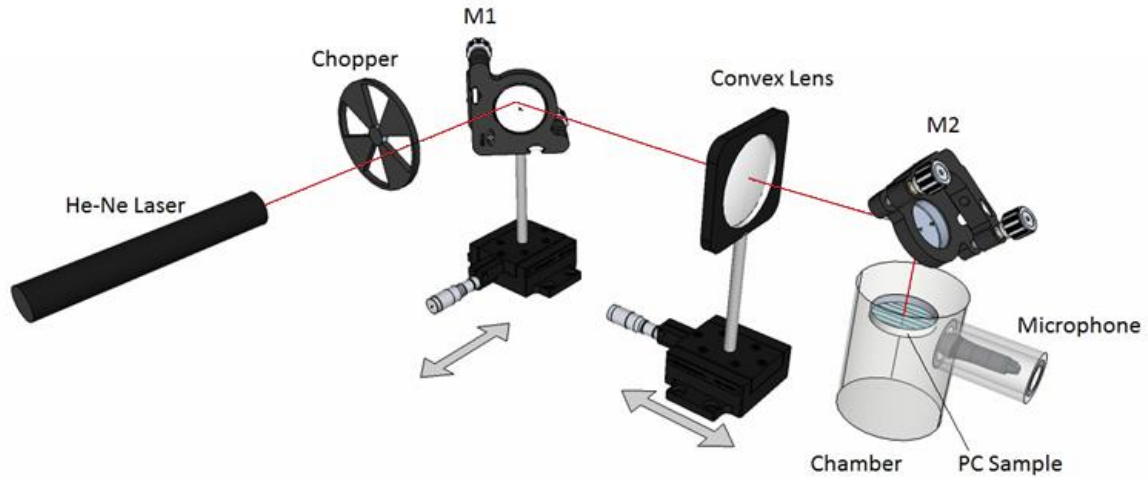


Figure 33. Optical setup for PC enhanced PA measurement. Linear polarized laser excitation at 632.8nm was intensity modulated by a mechanical chopper wheel and reflected by a mirror (M1) that is translated horizontally to adjust the angle of incidence. A long-focus lens was used to focus the laser beam onto the PC sensor located on the topside of the PA chamber. The diameter of the focused laser spot was around $80\ \mu\text{m}$ [98].

4.4 Characteristics of PC Enhanced PA Detection

In order to characterize the enhancement performance of the fabricated PC, a PA detection experiment using a light absorbing dye was carried out on the PC substrate. The PC substrate was cleaned with isopropyl alcohol, deionized water, and dry N_2 , and the organic dye (Epolight 5262, Epolin Inc.) was dissolved in methanol and made up to concentrations in the range from $50\ \mu\text{g/mL}$ down to $1\ \mu\text{g/mL}$. The dye solutions were drop-cast on the substrates and dried before use. To identify the resonant angle, we measured the laser transmission efficiency through the PC as a function of incident angle (θ_i) as shown in Figure 34, where the dip in the transmission curve corresponds to the resonant angle (θ_r), in this

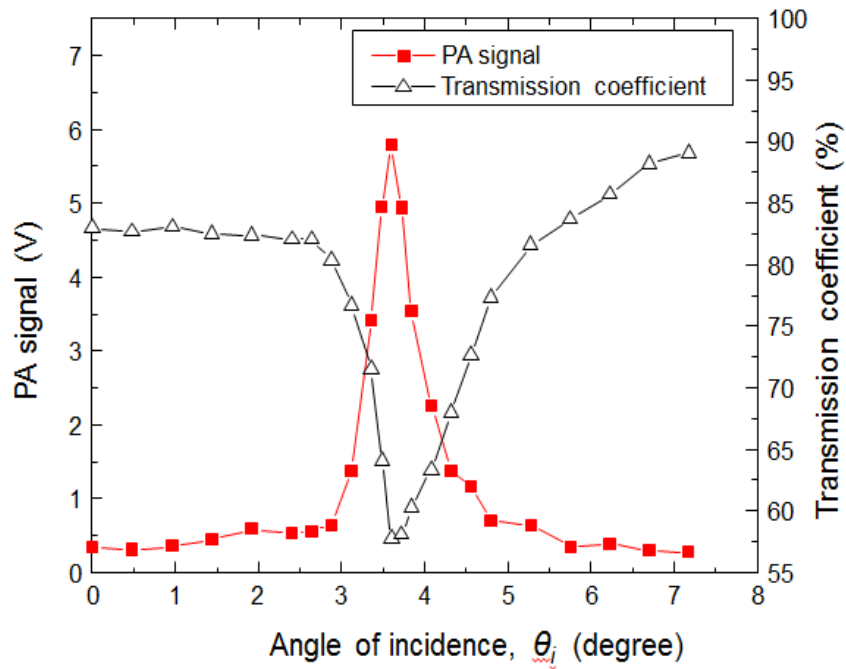


Figure 34. Incident angle dependence of the PA signals of organic dye Epolight 5262. The peak in PA signal coincides well with the transmission dip near 3.5, verifying the enhancement of PA signal by GMR [98].

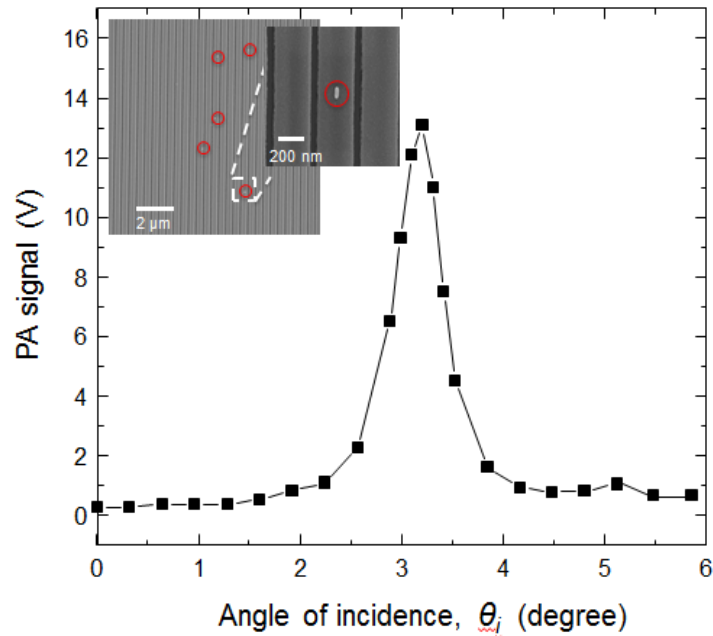


Figure 35. Incident angle dependence of the PA signals of AuNPs. It has a similar pattern as that of the absorbing dye. The inset SEM image shows the presence of AuNPs [98].

case, $\theta_r = 3.5^\circ$. Plotted as the red curve in the same figure is the PA signal from $5 \mu\text{g/mL}$ dye absorbed on the PC surface. Figure 34 clearly illustrates how the optical resonance (low transmission efficiency) results in a stronger PA output. After the subtraction of background signal, the PA signal at $\theta_r = 3.5^\circ$ is 5.8 V that is more than $10 \times$ higher than the PA signal measured away from this angle. The PA signals of AuNPs show similar results, as shown in Figure 35.

4.5 PC Enhanced PA Detection of an Absorbing Dye and AuNPs

A 2-fold dilution series of a total of six dye concentrations from $1 \mu\text{g/mL}$ to $50 \mu\text{g/mL}$ were measured under both on- and off-resonance conditions using the PA detection method. In Figure 36, the red curve represents PA signals measured under resonance condition, when the GMR was excited at the angle of incidence of $\theta_r = 3.5^\circ$. As a reference, the black curve in Figure 34 shows the PA signal outputs of the dyes when the HeNe laser illuminated the PC under “off-resonance” condition ($\theta_i = 7^\circ$). At the dye concentrations below $20 \mu\text{g/mL}$, both curves vary linearly in terms of dye concentration. In this linear range, the sensitivity is $1.25 \text{ V}/(\mu\text{g/mL})$ when the PC is on resonance as compared to $0.18 \text{ V}/(\mu\text{g/mL})$ when it is off resonance, resulting in an averaged enhancement of 7-fold. Figure 36 clearly demonstrates that the PC enhancement provided easily distinguishable PA outputs and an extended range of quantification for the dyes at low concentrations. At higher concentrations, the PA signal started to saturate and the enhancement factor was reduced to 5.3 because the loss induced by the absorption of dye molecules quenched the PC resonance and reduced the PC enhancement factor.

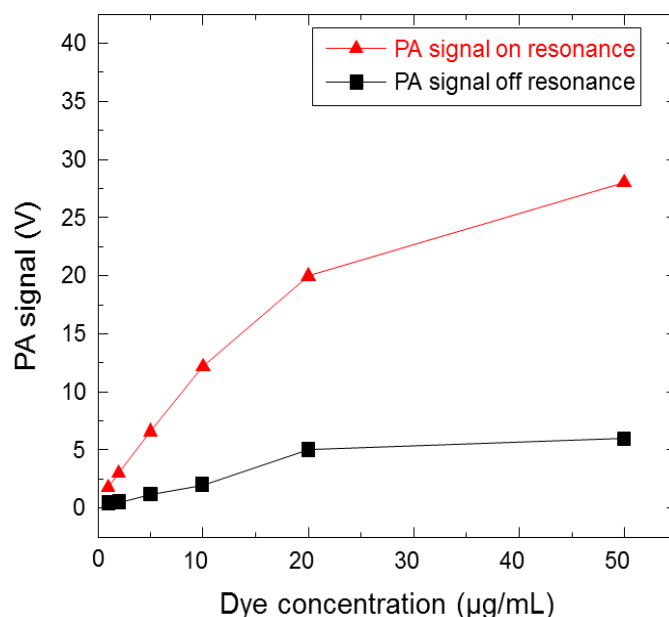


Figure 36. Enhancement of PA signals of an absorbing dye by GMR of PC substrates. The PA signal was increased 10-fold when measured under on-resonance conditions [98].

Detection of metal NPs was characterized by depositing gold nanorods onto the PC surface. Gold nanoparticle samples were prepared by suspending gold nanorods of approximately 25 nm axial diameter (A12-25-650, Nanopartz Inc.) in DI water. To deposit the AuNPs, 10 μL spots of these samples were pipetted onto PC substrates and allowed to dry in the air before measuring. A scanning electron microscopy image of PC coated with AuNPs at the concentration of 10^{10} NPs/mL is shown in the inset of Figure 35 where only a few nanorods are present within a $10 \mu\text{m} \times 10 \mu\text{m}$ area. Figure 35 illustrates the intensity of PA signal measured as a function of the incident angle of the excitation laser. The laser was scanned from $\theta_i = 0^\circ$ to 7.2° and coupled into the GMR at $\theta_i = 3.2^\circ$. Measured under resonant conditions, the intensity of PA signal is over 13 V that is 40 times stronger than the PA output (0.33 V) measured without utilizing the PC resonance.

The PC provides a substantial increase in the PA output of AuNPs and also a significant reduction in the PA detection limit. In order to demonstrate this, samples coated with AuNPs at a range of concentrations (10^{12} NPs/mL, 10^{11} NPs/mL, 10^{10} NPs/mL and 10^9 NPs/mL) are measured for the PC illuminated on-resonance ($\theta_i = 3.2^\circ$), off-resonance ($\theta_i = 7^\circ$), and for the control acrylic slides. The measured PA signals with background subtracted are compared in Figure 37. The lowest detectable concentration on an acrylic substrate (10^{10} NPs/mL) is reduced by one order of magnitude to 10^9 NPs/mL on a PC substrate. At higher

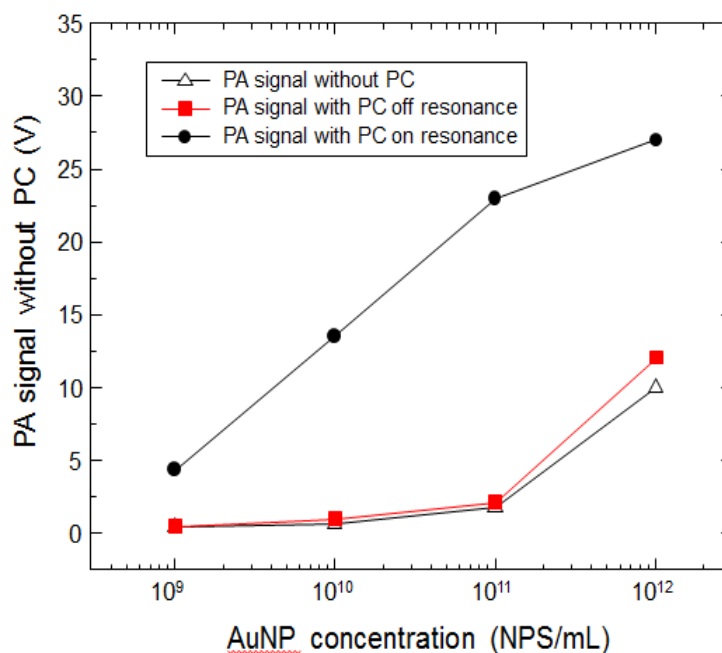


Figure 37. Enhancement of PA signals of AuNPs by GMR of PC substrates. The PA signal was increased 40-fold when measured under on-resonance conditions and at low concentrations that did not seriously deteriorate the quality factor (Q -factor) of the PC. At high concentrations however, the enhancement was lower due to the Q -factor being reduced by the excessive amount of AuNPs [98].

concentrations, the amplification factor becomes weaker due to the quench of optical resonance caused by the absorption of AuNPs. The PC sensor offers the capability to detect less than 10 nanorods within a $100 \mu\text{m}^2$ surface area.

In summary, a 1D PC substrate has been characterized for its capability to enhance the PA signal from light absorbers deposited onto the sensor surface. The PC sensor was incorporated into a PA measurement chamber and illuminated by a HeNe laser with the angle of incidence tuned to excite the GMR. The strengthened local field associated with the resonant mode increased the optical absorption of analytes deposited on the PC and resulted in an enhanced PA signal by factors of $10 \times$ and $40 \times$ for the organic light absorber and the gold nanorods, respectively. The enhanced PA signal consequently reduced the detection limit of metal nanoparticles by one order of magnitude. The PC substrate demonstrated here represents a powerful and practical approach for highly sensitive PA detection and would be improved further for sensors produced over a substantially large surface area with higher quality factors. In the future work, this technique will be exploited to facilitate the quantification of metal nanoparticles functionalized with recognition molecules, enabling a promising approach for diagnostic tests and environmental monitoring [30].

4.6 Acknowledgment

Parts of this chapter have been modified from my previous publication:

Zhao, Y., Liu, K., McClelland, J., & Lu, M. (2014). Enhanced photoacoustic detection using photonic crystal substrate. *Applied Physics Letters*, 104(16), 161110.

CHAPTER 5. PHOTONIC CRYSTAL ENHANCED PHOTOTHERMAL LENS

5.1 Principle of PC-enhanced PTL

The GMR induced strong near field of PC surface can greatly enhance the PA signal. In addition, it can also significantly enhance the PTL signal in the same manner. By coupling the probe beam to the GMR of PC, one can observe an enhanced PTL signal. The enhancement is due to the fact that the narrow band GMR of PC is very sensitive to the refractive index of surrounding medium. Figure 38 shows the optical setup of the PC enhanced PTL experiment. Before the pump beam is turned on, the probe beam's incident angle is tuned to a GMR peak. When the pump beam is turned on, the change in refractive index of the surrounding medium will change the resonance condition, thereby decoupling the probe beam from the GMR. This effect adds to the photothermal lens scattering effect and generates a sharp drop of the reflection of the probe beam that can be detected by the photodetector. Therefore, the PC substrate can increase the change of reflectivity (ΔR) relative to an unpatterned surface. The parameters of the optical components shown in Figure 38 are as follows: the wavelength of the pump laser (85-RCA-400, Melles Griot) is at $\lambda_{\text{pump}} = 660$ nm and the output power is $P_{\text{pump}} = 240$ mW. A convex lens ($f = 50$ mm) focuses the pump beam onto the PC surface. The probe laser (MingNuo OpticElectronc Co. Ltd.) has a wavelength of $\lambda_{\text{probe}} = 532$ nm and a power of $P_{\text{probe}} = 5$ mW, which is used to detect the pump-induced PTL. The probe beam is then reflected by a mirror (M1) and polarized to the TM mode of the PC by a linear polarizer, as TM mode has a narrower resonance peak than TE mode. A narrower resonance peak will result in a stronger PTL signal for a given concentration of the analyte, as a given amount of shift in resonance wavelength can produce a larger change in the reflectivity of the probe beam.

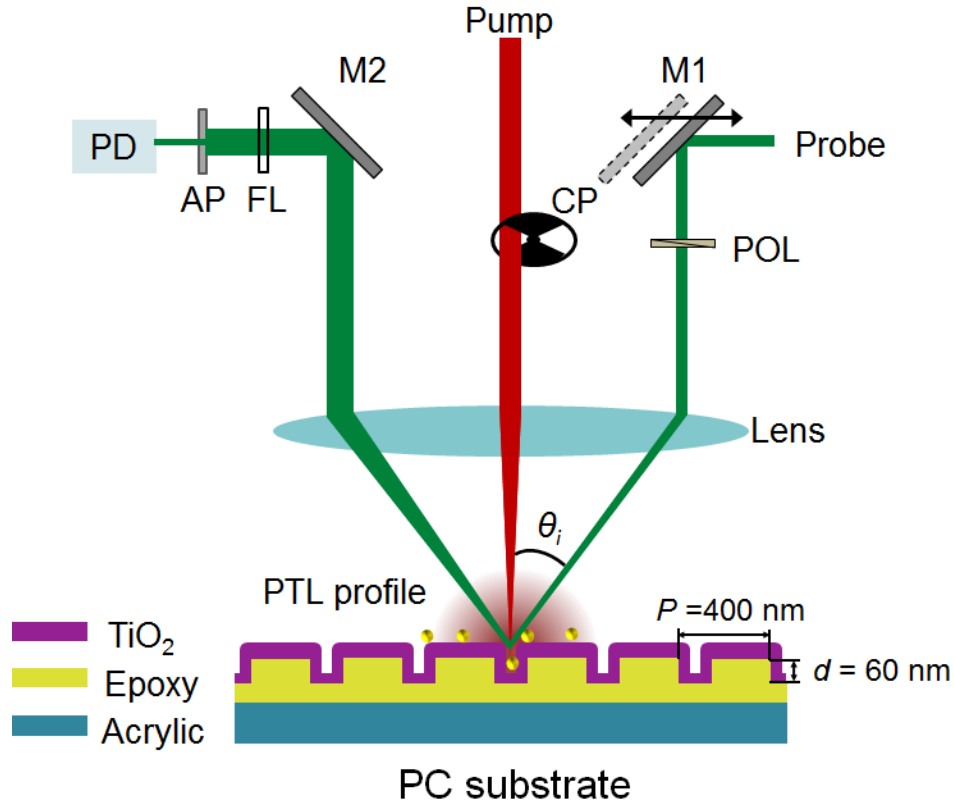


Figure 38. Schematic plot for PC enhanced PTL measurement. The schematic plot is not to scale. In the experiments, the PC sample is simultaneously illuminated with a pump beam at 660 nm and a probe beam at 532 nm. The pump beam is switched on and off by a chopper (CP) and focused onto the PC surface. The PTL generated by the sample is shown as the PTL profile. The probe laser is polarized by the linear polarizer (POL) to the TM mode of the PC surface and the incident angle is tuned by translating a mirror (M1). The reflected beam passes through the same focusing lens and is directed towards the photodetector (PD) through the mirror (M2), the laser line filter (FL) and the aperture (AP) [143].

To couple the probe beam into the resonance mode, the incident angle of the probe laser is precisely tuned by translating M1 using a linear translation stage (PT1B, Thorlabs Inc.) and passing it through a convex lens in order to couple it efficiently into a PC resonance mode. The reflected probe beam from the PC surfaces passes through a bandpass filter with a central wavelength of $\lambda_c = 532$ nm and a bandwidth of $\Delta\lambda = 5$ nm and an aperture with a

diameter of 2 mm before hitting the photodetector (PDA10A, Thorlabs Inc.). The photodetector's output was measured with an oscilloscope (TDS2014B, Tektronix).

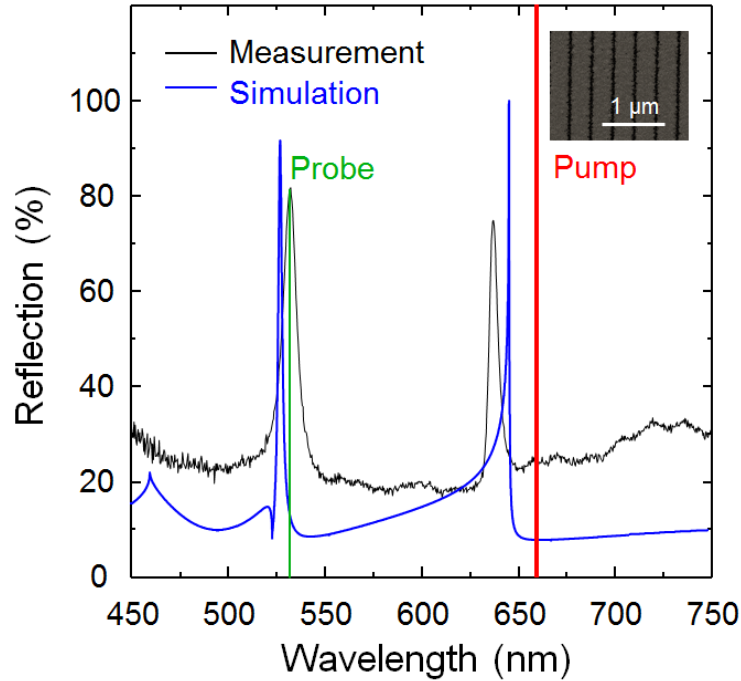


Figure 39. Characterizations of the PC sample. The simulation and experimental result of the PC reflection spectrum when the incident angle $\theta_i = 12^\circ$. The wavelengths of the probe and pump laser beams are represented by the green and red lines, respectively. The probe beam is coupled to the PC resonance at 532 nm, but the pump laser does not overlap with any PC resonance [143].

During a test, the pump beam was turned on and off using a chopper. The measurements were taken three seconds after the switching of the pump beam so that the sample could reach a stabilized thermal state before measurements. The ratio between the change in reflectance ΔR under these two circumstances (on and off) and the reflectance R measured without the presence of the pump beam, i.e. $\Delta R/R$, were recorded as the PTL signal. As illustrated in Figure 39, in a PTL experiment, the probe beam is coupled to one of the GMR modes of the PC substrate, but the pump beam is not. One reason for this arrangement is that the requirement on alignment can be less stringent. The other reason for choosing not

to couple the pump beam is that the PTL signal of this configuration is not sensitive to the pump wavelength, thereby allowing the measurement of PT spectrum of a sample. The inset of Figure 39 shows the surface of the PC.

5.2 Characteristics of PC Enhancement

To demonstrate the enhancement effect of the PC substrate, we measured the PTL signal of an absorbing dye Epolight 6661. This dye molecule has a strong absorption from 600 nm to 700 nm with the absorption peak located at 666 nm. The dye was dissolved in ethanol at a concentration of 1.0 mg/mL and dipped on the PC surface to absorb the pump beam. Figure 40 shows the pictures of the reflected probe laser spots when the pump beam was off (left panel) and on (right panel), respectively. A significant change in light intensity occurs at the center of the probe beam spot when the pump beam was switched on. This is because the heat generated by the optical absorption heats the surrounding air. The region of hot air has a lower refractive index than the surrounding cold air and acts as a thermal lens to diverge the probe beam. Meanwhile, the thermal lens also causes a shift of the PC resonance and decouples the probe beam from the GMR, thereby reducing the reflectivity of the probe beam. The reflected probe beam is masked with an aperture that only allows the region circled in red (Figure 40) to pass through and hit the photodetector. The percentage change in reflectivity ($\Delta R/R$) is calculated as the PTL signal. Figure 41 shows the measurement of PTL signal as a function of the incident angle of the probe beam. The transmission of the probe beam through the PC is also plotted in Figure 41 to mark the angular position of the PC resonance. For the transmission measurement, the PC was mounted on a rotation stage. The

probe beam (532 nm) was polarized with a linear polarizer and passed through the PC substrate. By rotating the PC, the incident angle was tuned from 4° to 16° with an increment

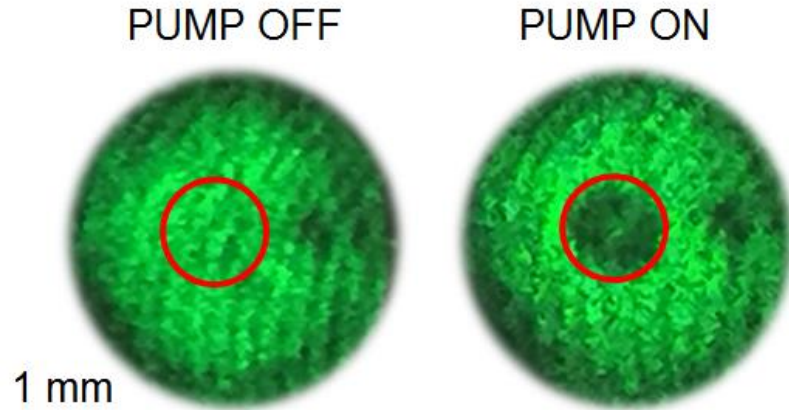


Figure 40. Photographs of the reflected probe beam. The two photographs were taken when the pump laser beam is switched off (left panel) and on (right panel), respectively [143].

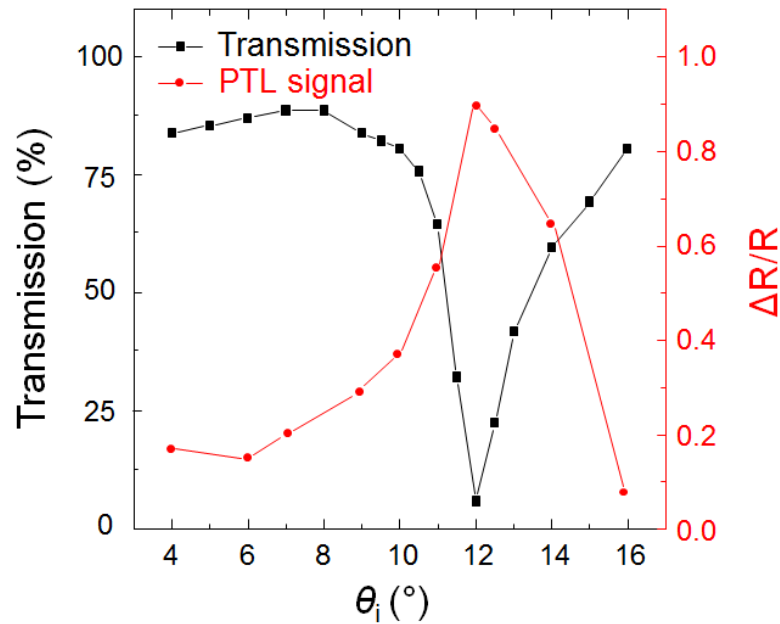


Figure 41. Transmission of the probe laser through the PC substrate and the PTL signals. Both curves were measured as a function of the incident angle of the probe beam [143].

of 1° , and 0.5° near the resonance peak. The transmitted beam was measured with a photodiode (PDA10A, Thorlabs Inc.). The transmittance was calculated as the measured power divided by the output power of the probe laser (5 mW). In the transmittance curve, the dip that represents the PC resonance appears at $\theta_i = 12^\circ$; the same angle as the peak is located, showing a good correlation between the PC resonance and the PTL signal peak. The PTL signal measured at $\theta_i = 12^\circ$ (on-resonance) is 10-fold stronger than the signal at $\theta_i = 16^\circ$ (off-resonance).

5.3 PTL Measurement of an Absorbing Dye

After the preliminary test, we moved on to measure the concentration of a dilution series of the dye. We made a 2-fold dilution series consisting eight concentrations (mg/mL): 1.0, 0.5, 0.25, 0.125, 0.062, 0.031, 0.016 and 0.0078. For each concentration, three 20- μ L droplets were pipetted onto one PC substrate, each serving as a replicate. After drying under ambient conditions for 20 minutes, the samples were measured with the aforementioned PTL setup. Figure 42 shows the PTL results of this series of Epolight/ethanol solutions. The black curve represents the PTL signals measured on the PC resonance, while the red curve shows the results for measurement carried out under off-resonance conditions. The on-resonance PTL signals are significantly stronger than the off-resonance ones. The PC resonance effectively extends the linear detection range. The key performance metrics for PTL analysis is the lowest distinguishable concentration of the dye.

As shown in Figure 42, the lowest distinguishable concentration of the on-resonance measurement is 0.031 mg/mL, whereas that of the off-resonance measurement is 0.25 mg/mL. Therefore, the PC resonance increases the sensitivity by a factor of 8. It is worth noting that

the curve for the on-resonance PTL signal saturated at 1 mg/mL due to deterioration of Q-factor of the PC caused by the excessive amount of organic dye.

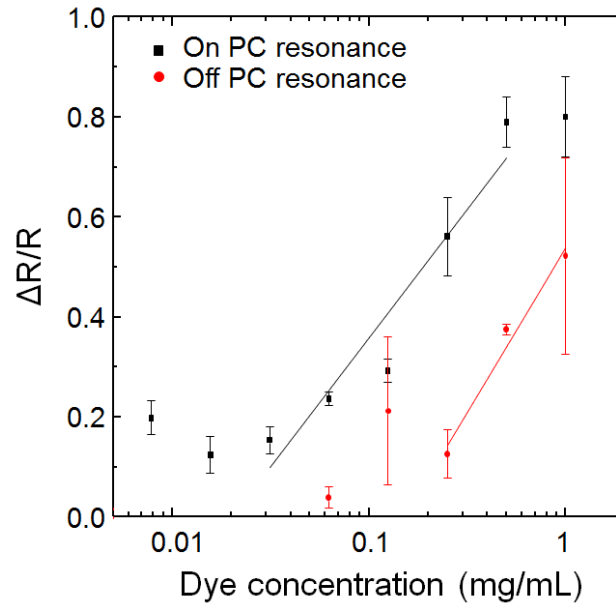


Figure 42. PTL measurement of light absorbing dye. The black and red curves correspond to the tests with the probe laser coupled to PC resonance at $\theta_i = 12^\circ$ and off the PC resonance ($\theta_i = 24^\circ$), respectively. The linear range of each measurement was fitted using a linear curve [143].

5.4 PTL Measurement of AuNPs

Apart from the absorbing dye, AuNPs were quantitatively measured in the same fashion. AuNPs with an axial diameter of approximately 25 nm (C12-10-700, Nanopartz Inc.) were suspended in DI water to make a dilution series that contained the following concentrations (in NPs/mL): 2.5×10^{11} , 1.0×10^{11} , 5.0×10^{10} , 2.5×10^{10} , 1.0×10^{10} , 5.0×10^9 , 2.5×10^9 , 1.0×10^9 , and 5.0×10^8 . For each concentration, three 20- μ L droplets were pipetted onto one PC surface. The samples were dried under ambient conditions for one hour, then measured with the same method as the absorbing dye. The SEM images of the AuNP coated

PC substrates with AuNP concentrations of 1.0×10^{11} , 2.5×10^{10} , and 5.0×10^9 NPs/mL are shown in Figure 43. From the images, we can conclude that at medium to low concentrations,

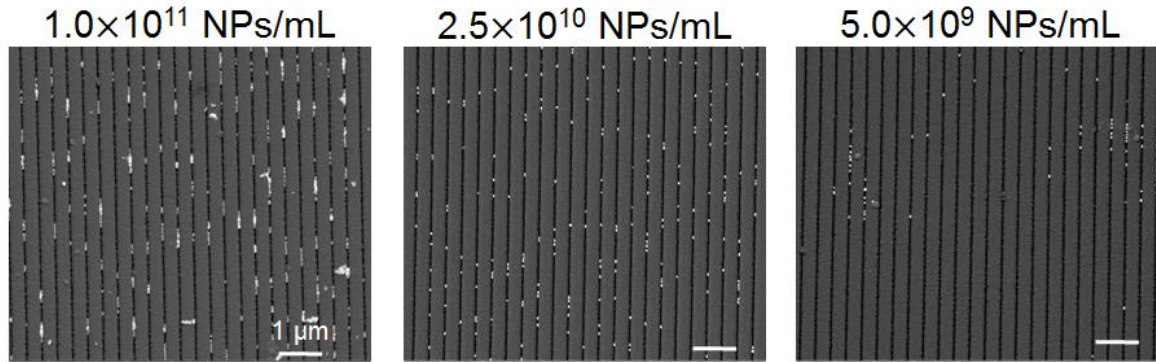


Figure 43. SEM images of AuNPs dispersed on PC surfaces at three different concentrations. The images indicate that the AuNPs tend to reside in the grooves on the PC surface [143].

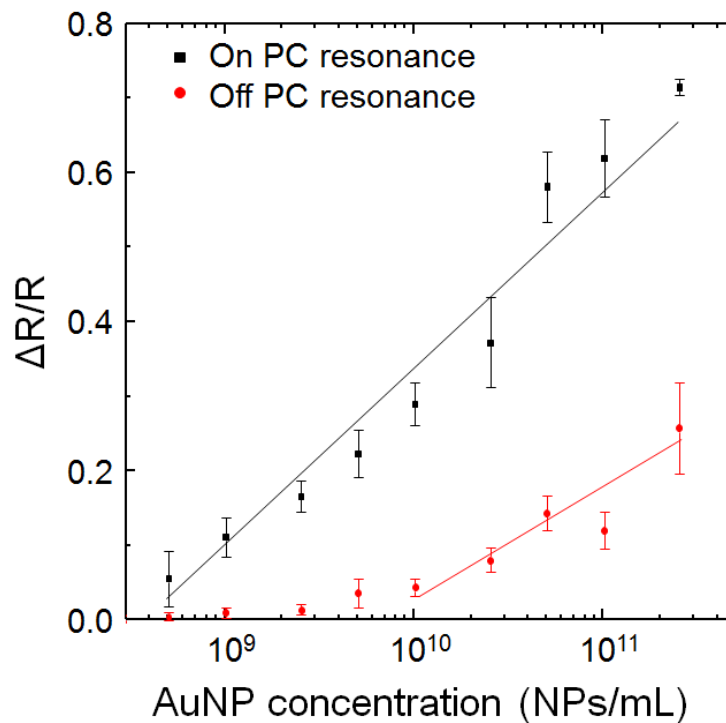


Figure 44. PTL signals of AuNPs plotted as a function of the AuNP concentration. The black and red curves correspond to the tests with the probe laser coupled to PC resonance ($\theta_r = 12^\circ$) and off the PC resonance ($\theta_i = 24^\circ$), respectively. The linear range of each measurement was fitted using a linear curve [143].

the AuNPs are dispersed largely uniformly. The measurement of these samples was conducted under both on-resonance ($\theta_i = 12^\circ$) and off-resonance ($\theta_i = 24^\circ$) conditions. The data are compared in Figure 44. Under on-resonance conditions, AuNPs at a concentration as low as 5.0×10^8 NPs/mL can be detected, which represented a detection limit 20 times lower than that of the off-resonance analysis. The dynamic range of on-resonance measurement is also larger than off-resonance measurement. As shown in Figure 44, the curve measured on-resonance shows a linear response range from 5×10^8 NPs/mL to 2.5×10^{11} NPs/mL, while the linear range of the off-resonance measurement is only from 1.0×10^{10} NPs/mL to 2.5×10^{11} NPs/mL. Therefore, the PC-enhanced PTL is capable of measuring AuNPs with greater detection sensitivity and a broader dynamic range.

The PC-enhanced PTL system demonstrated in this work is to the best of my knowledge the first demonstration using the GMR of 1-D PC to enhance the pump-probe PTL analysis of optically thin materials. While the PC design is sufficient to demonstrate the enhancement effect, its performance may be optimized further to enhance the PTL signal. For example, the measured linewidth of the PC resonance peak is 7.3 nm. This linewidth can be reduced according to previous studies [144]. A PC resonance peak with a narrower linewidth can enable a more prominent change in reflectance of the probe beam, thereby improving the sensitivity to the thermal lens. In addition, when the spectral information of the sample absorption is not required, it is possible to couple the pump beam into a PC resonance as well to take advantage of the strengthened local field. The near-field enhancement of the PC surface will increase the absorption of the pump beam and result in a stronger PTL effect.

5.5 Acknowledgment

Parts of this chapter have been modified from my previous publication:

Zhao, Y., Liu, L., Zhao, X., & Lu, M. (2016). Enhanced photothermal lens using a photonic crystal surface. *Applied Physics Letters*, 109(7), 071108.

CHAPTER 6. CONCLUSIONS

In summary, PA and PTL detection of AuNPs and biomarkers, and its enhancement by PC substrates, was studied using several methods and protocols for the detection of several biomarkers were developed. A PA immunoassay protocol was developed based on the ELISA format and human IL-8 was quantified using this method as an example. The method used AuNPs as a tag to label biomarkers and used a standard laser-based PA detection system to quantify the concentration of AuNPs. The LOD was improved by an order of magnitude using this method. A PA measurement for CrAg LFA was also developed so that CrAg could be quantitatively measured with a detection limit of 10 pg/mL, which was comparable to lab-based assays. The PA detection was further enhanced by using a PC substrate. The GMR of the PC substrate significantly enhanced the near field intensity compared to the input optical field intensity and a limit of detection of less than 10 AuNRs per 100 μm^2 was attained. The PTL effect was also studied in this work, and a technique for PC enhanced PTL detection of absorbing dye or AuNPs was developed. The technique achieved a detection limit of 0.031 mg/mL for absorbing dye, and 5.0×10^8 NPs/mL for AuNPs. In the future, a hand-held PA unit that can fit into a single well of the microtiter plate will be developed and the sensitivity will be improved even further, enabling a promising approach for point-of-care diagnostic system and environmental monitoring. As for the PTL detection, a PTL spectral measurement using a tunable infrared laser can also be developed and can be used to obtain surface optical properties of materials with high accuracy.

REFERENCES

- [1] Hsieh, J. (2003). *Computed tomography: principles, design, artifacts, and recent advances* (Vol. 114). SPIE press.
- [2] Nyström, L., Wall, S., Rutqvist, L. E., Lindgren, A., Lindqvist, M., Ryden, S., ... & Tabar, L. (1993). Breast cancer screening with mammography: overview of Swedish randomised trials. *The Lancet*, 341(8851), 973-978.
- [3] Selby, J. V., Friedman, G. D., Quesenberry Jr, C. P., & Weiss, N. S. (1992). A case-control study of screening sigmoidoscopy and mortality from colorectal cancer. *New England Journal of Medicine*, 326(10), 653-657.
- [4] Lieberman, D. A., Weiss, D. G., Bond, J. H., Ahnen, D. J., Garewal, H., Harford, W. V., ... & Nelson, D. B. (2000). Use of colonoscopy to screen asymptomatic adults for colorectal cancer. *New England Journal of Medicine*, 343(3), 162-168.
- [5] Fahey, M. T., Irwig, L., & Macaskill, P. (1995). Meta-analysis of Pap test accuracy. *American Journal of Epidemiology*, 141(7), 680-689.
- [6] Kronborg, O., Fenger, C., Olsen, J., Jørgensen, O. D., & Søndergaard, O. (1996). Randomised study of screening for colorectal cancer with faecal-occult-blood test. *The Lancet*, 348(9040), 1467-1471.
- [7] Liu, X., Dai, Q., Austin, L., Coutts, J., Knowles, G., Zou, J., ... & Huo, Q. (2008). A one-step homogeneous immunoassay for cancer biomarker detection using gold nanoparticle probes coupled with dynamic light scattering. *Journal of the American Chemical Society*, 130(9), 2780-2782.
- [8] Ludwig, J. A., & Weinstein, J. N. (2005). Biomarkers in cancer staging, prognosis and treatment selection. *Nature Reviews Cancer*, 5(11), 845-856.
- [9] Li, K., Chen, R., Zhao, B., Liu, M., Karu, A. E., Roberts, V. A., & Li, Q. X. (1999). Monoclonal antibody-based ELISAs for part-per-billion determination of polycyclic aromatic hydrocarbons: effects of haptens and formats on sensitivity and specificity. *Analytical Chemistry*, 71(2), 302-309.
- [10] Greene, R. A., & Kasila, P. A. (1992). *U.S. Patent No. 5,137,804*. Washington, DC: U.S. Patent and Trademark Office.
- [11] Stern, E., Vacic, A., Rajan, N. K., Criscione, J. M., Park, J., Ilic, B. R., ... & Fahmy, T. M. (2010). Label-free biomarker detection from whole blood. *Nature Nanotechnology*, 5(2), 138-142.

- [12] Fan, R., Vermesh, O., Srivastava, A., Yen, B. K., Qin, L., Ahmad, H., Kwong, G.A., Liu, C.C., Gould, J., Hood, L. & Heath, J. R. (2008). Integrated barcode chips for rapid, multiplexed analysis of proteins in microliter quantities of blood. *Nature Biotechnology*, 26(12), 1373-1378.
- [13] Hanash, S. M., Baik, C. S., & Kallioniemi, O. (2011). Emerging molecular biomarkers—blood-based strategies to detect and monitor cancer. *Nature Reviews Clinical Oncology*, 8(3), 142-150.
- [14] Rhea, J. M., & Molinaro, R. J. (2011). Cancer biomarkers: surviving the journey from bench to bedside. *MLO Medical Laboratory Observer*, 43(3), 10.
- [15] Gan, S. D., & Patel, K. R. (2013). Enzyme immunoassay and enzyme-linked immunosorbent assay. *Journal of Investigative Dermatology*, 133(9), 1-3.
- [16] Huang, C. S., George, S., Lu, M., Chaudhery, V., Tan, R., Zangar, R. C., & Cunningham, B. T. (2011). Application of photonic crystal enhanced fluorescence to cancer biomarker microarrays. *Analytical Chemistry*, 83(4), 1425-1430.
- [17] Lequin, R. M. (2005). Enzyme immunoassay (EIA)/enzyme-linked immunosorbent assay (ELISA). *Clinical Chemistry*, 51(12), 2415-2418.
- [18] Voller, A., Bartlett, A., & Bidwell, D. E. (1978). Enzyme immunoassays with special reference to ELISA techniques. *Journal of Clinical Pathology*, 31(6), 507-520.
- [19] Yingyongnarongkul, B. E., How, S. E., Diaz-Mochon, J. J., Muzerelle, M., & Bradley, M. (2003). Parallel and multiplexed bead-based assays and encoding strategies. *Combinatorial Chemistry & High Throughput Screening*, 6(7), 577-587.
- [20] Shahzad, A., Knapp, M., Lang, I., & Köhler, G. (2010). Interleukin 8 (IL-8)-a universal biomarker. *International Archives of Medicine*, 3(1), 11.
- [21] Azar Sharabiani, M. T., Vermeulen, R., Scoccianti, C., Hosnijeh, F. S., Minelli, L., Sacerdote, C., Palli, D., Krogh, V., Tumino, R., Chiodini, P. & Panico, S. (2011). Immunologic profile of excessive body weight. *Biomarkers*, 16(3), 243-251.
- [22] Medac-diagnostika-Protein-und Nukleinsäurenachweis-ELISA-ABTS Peroxidase Stop Soluion Kit, 2×100 ml, Artikel-Nr.: 5150-0017 Retrieved August 25, 2014 from http://www.medac-diagnostika.de/index.php?id_product=2468&controller=product&id_lang=1
- [23] Dodeigne, C., Thunus, L., & Lejeune, R. (2000). Chemiluminescence as diagnostic tool. A review. *Talanta*, 51(3), 415-439.

- [24] Mathias, P. C., Ganesh, N., & Cunningham, B. T. (2008). Application of photonic crystal enhanced fluorescence to a cytokine immunoassay. *Analytical Chemistry*, 80(23), 9013-9020.
- [25] Goldys, E. M. (2009). *Fluorescence applications in biotechnology and life sciences*. John Wiley & Sons.
- [26] Lakowicz, J.R. (1999). Principles of fluorescence spectroscopy, 2nd ed. Kluwer Academic/Plenum, New York.
- [27] Escosura-Muñiz, Alfredo De La, Parolo, C. & Merkoç, A. Immunosensing using nanoparticles. *Materials Today* 13.13(2010):24-34.
- [28] Huang, X., Neretina, S., & El-Sayed, M. A. (2009). Gold nanorods: from synthesis and properties to biological and biomedical applications. *Advanced Materials*, 21(48), 4880-4910.
- [29] Segev-Bar, M., & Haick, H. (2013). Flexible sensors based on nanoparticles. *ACS Nano*, 7(10), 8366-8378.
- [30] Willets, K. A., & Van Duyne, R. P. (2007). Localized surface plasmon resonance spectroscopy and sensing. *Annual Review of Physical Chemistry*, 58, 267-297.
- [31] Sagle, L. B., Ruvuna, L. K., Ruemmele, J. A., & Van Duyne, R. P. (2011). Advances in localized surface plasmon resonance spectroscopy biosensing. *Nanomedicine*, 6(8), 1447-1462.
- [32] Govorov, A. O., Zhang, W., Skeini, T., Richardson, H., Lee, J. & Kotov, N.A. (2006). Gold nanoparticle ensembles as heaters and actuators: melting and collective plasmon resonances. *Nanoscale Research Letters* 1(1), 84.
- [33] Awazu, K., Fujimaki, M., Rockstuhl, C., Tominaga, J., Murakami, H., Ohki, Y., Yoshida, N. & Watanabe, T. (2008). A plasmonic photocatalyst consisting of silver nanoparticles embedded in titanium dioxide. *Journal of the American Chemical Society*, 130(5), 1676-1680.
- [34] Cao, Y. C., Jin, R., & Mirkin, C. A. (2002). Nanoparticles with Raman spectroscopic fingerprints for DNA and RNA detection. *Science*, 297(5586), 1536-1540.
- [35] Nam, J. M., Thaxton, C. S., & Mirkin, C. A. (2003). Nanoparticle-based bio-bar codes for the ultrasensitive detection of proteins. *Science*, 301(5641), 1884-1886.
- [36] Stratakis, E., & Kymakis, E. (2013). Nanoparticle-based plasmonic organic photovoltaic devices. *Materials Today*, 16(4), 133-146.

- [37] Jaque, D., Maestro, L. M., Del Rosal, B., Haro-Gonzalez, P., Benayas, A., Plaza, J. L., Rodriguez, E.M. & Sole, J. G. (2014). Nanoparticles for photothermal therapies. *Nanoscale*, 6(16), 9494-9530.
- [38] Yang, X., Stein, E. W., Ashkenazi, S., & Wang, L. V. (2009). Nanoparticles for photoacoustic imaging. *Wiley Interdisciplinary Reviews: Nanomedicine and Nanobiotechnology*, 1(4), 360-368.
- [39] Sperling, R. A., & Parak, W. J. (2010). Surface modification, functionalization and bioconjugation of colloidal inorganic nanoparticles. *Therapeutic Innovation & Regulatoryence*, 368(1915), 1333.
- [40] McClelland, J. F., & Kniseley, R. N. (1976). Photoacoustic spectroscopy with condensed samples. *Applied Optics*, 15(11), 2658-2663.
- [41] Posthuma-Trumpie, G. A., Korf, J., & van Amerongen, A. (2009). Lateral flow (immuno) assay: its strengths, weaknesses, opportunities and threats. A literature survey. *Analytical and Bioanalytical Chemistry*, 393(2), 569-582.
- [42] Yetisen, A. K., Akram, M. S., & Lowe, C. R. (2013). Paper-based microfluidic point-of-care diagnostic devices. *Lab on a Chip*, 13(12), 2210-2251.
- [43] Sajid, M., Kawde, A. N., & Daud, M. (2015). Designs, formats and applications of lateral flow assay: A literature review. *Journal of Saudi Chemical Society*, 19(6), 689-705.
- [44] Gubala, V., Harris, L. F., Ricco, A. J., Tan, M. X., & Williams, D. E. (2011). Point of care diagnostics: status and future. *Analytical Chemistry*, 84(2), 487-515.
- [45] Corstjens, P. L., van Lieshout, L., Zuiderwijk, M., Kornelis, D., Tanke, H. J., Deelder, A. M., & van Dam, G. J. (2008). Up-converting phosphor technology-based lateral flow assay for detection of *Schistosoma* circulating anodic antigen in serum. *Journal of Clinical Microbiology*, 46(1), 171-176.
- [46] Anfossi, L., D'Arco, G., Calderara, M., Baggiani, C., Giovannoli, C., & Giraudi, G. (2011). Development of a quantitative lateral flow immunoassay for the detection of aflatoxins in maize. *Food Additives and Contaminants*, 28(2), 226-234.
- [47] Quesada-González, Daniel; Merkoç, Arben (2015). "Nanoparticle-based lateral flow biosensors". *Biosensors & Bioelectronics*, 15 (special), 47–63.
- [48] Rong-Hwa, S., Shiao-Shek, T., Der-Jiang, C., & Yao-Wen, H. (2010). Gold nanoparticle-based lateral flow assay for detection of staphylococcal enterotoxin B. *Food Chemistry*, 118(2), 462-466.

- [49] Zhao, Y., Huang, Y., Zhao, X., McClelland, J. F., & Lu, M. (2016). Nanoparticle-based photoacoustic analysis for highly sensitive lateral flow assays. *Nanoscale*, 8(46), 19204-19210.
- [50] Li, C. Z., Vandenberg, K., Prabhulkar, S., Zhu, X., Schneper, L., Methee, K., Rosser, C.J. & Almeida, E. (2011). Paper based point-of-care testing disc for multiplex whole cell bacteria analysis. *Biosensors and Bioelectronics*, 26(11), 4342-4348.
- [51] Wong, S. Y., Cabodi, M., Rolland, J., & Klapperich, C. M. (2014). Evaporative concentration on a paper-based device to concentrate analytes in a biological fluid. *Analytical Chemistry*, 86(24), 11981-11985.
- [52] Tang, R., Yang, H., Choi, J. R., Gong, Y., Hu, J., Feng, S., Pingguan-Murphy, B., Mei, Q. & Xu, F. (2016). Improved sensitivity of lateral flow assay using paper-based sample concentration technique. *Talanta*, 152, 269-276.
- [53] Pereira, D. Y., Chiu, R. Y., Zhang, S. C., Wu, B. M., & Kamei, D. T. (2015). Single-step, paper-based concentration and detection of a malaria biomarker. *Analytica Chimica Acta*, 882, 83-89.
- [54] Moghadam, B. Y., Connelly, K. T., & Posner, J. D. (2014). Isotachophoretic preconcentration on paper-based microfluidic devices. *Analytical Chemistry*, 86(12), 5829-5837.
- [55] Fu, X., Cheng, Z., Yu, J., Choo, P., Chen, L., & Choo, J. (2016). A SERS-based lateral flow assay biosensor for highly sensitive detection of HIV-1 DNA. *Biosensors and Bioelectronics*, 78, 530-537.
- [56] Choi, J. R., Hu, J., Feng, S., Abas, W. A. B. W., Pingguan-Murphy, B., & Xu, F. (2016). Sensitive biomolecule detection in lateral flow assay with a portable temperature–humidity control device. *Biosensors and Bioelectronics*, 79, 98-107.
- [57] Qin, Z., Chan, W. C., Boulware, D. R., Akkin, T., Butler, E. K., & Bischof, J. C. (2012). Significantly improved analytical sensitivity of lateral flow immunoassays by using thermal contrast. *Angewandte Chemie International Edition*, 51(18), 4358-4361.
- [58] Anker, J. N., Hall, W. P., Lyandres, O., Shah, N. C., Zhao, J., & Van Duyne, R. P. (2008). Biosensing with plasmonic nanosensors. *Nature Materials*, 7(6), 442-453.
- [59] Huang, X., El-Sayed, I. H., Qian, W., & El-Sayed, M. A. (2006). Cancer cell imaging and photothermal therapy in the near-infrared region by using gold nanorods. *Journal of the American Chemical Society*, 128(6), 2115-2120.
- [60] Bingham, J. M., Anker, J. N., Kreno, L. E., & Van Duyne, R. P. (2010). Gas sensing with high-resolution localized surface plasmon resonance spectroscopy. *Journal of the American Chemical Society*, 132(49), 17358-17359.

- [61] Xianyu, Y., Xie, Y., Wang, N., Wang, Z., & Jiang, X. (2015). A Dispersion-Dominated Chromogenic Strategy for Colorimetric Sensing of Glutathione at the Nanomolar Level Using Gold Nanoparticles. *Small*, 11(41), 5510-5514.
- [62] Guo, Y., Zhang, Y., Shao, H., Wang, Z., Wang, X., & Jiang, X. (2014). Label-free colorimetric detection of cadmium ions in rice samples using gold nanoparticles. *Analytical Chemistry*, 86(17), 8530-8534.
- [63] Zhu, K., Zhang, Y., He, S., Chen, W., Shen, J., Wang, Z., & Jiang, X. (2012). Quantification of proteins by functionalized gold nanoparticles using click chemistry. *Analytical Chemistry*, 84(10), 4267-4270.
- [64] Taton, T. A., Mirkin, C. A., & Letsinger, R. L. (2000). Scanometric DNA array detection with nanoparticle probes. *Science*, 289(5485), 1757-1760.
- [65] Chen, J., Jin, Y., Fahrudin, N., & Zhao, J. X. (2013). Development of gold nanoparticle-enhanced fluorescent nanocomposites. *Langmuir*, 29(5), 1584-1591.
- [66] Bell, A. G. (1880). On the production and reproduction of sound by light. *American Journal of Science*, 118, 305.
- [67] Bell, A. G. (1881). LXVIII. Upon the production of sound by radiant energy. *Philosophical Magazine Series 5*, 11(71), 510.
- [68] Harren, F. J. M., Cotti, G., Oomens, J. & te Lintel Hekkert, S. (2000) Environment: Trace Gas Monitoring. *Encyclopedia of Analytical Chemistry*, M. W. Sigrist and R. A. Meyers (eds.) 3, 2203.
- [69] Rosencwaig, A. (1976). Theory of the photoacoustic effect with solids. *Journal of Applied Physics*, 47, 64
- [70] Ryczkowski, J. (2007). Application of infrared photoacoustic spectroscopy in catalysis. *Catalysis Today*, 124, 11.
- [71] Yang, C. Q., Bresee, R. R., Fateley, W. G. (1987). Near-Surface Analysis and Depth Profiling by FT-IR Photoacoustic Spectroscopy. *Applied Spectroscopy*, 41(5), 889.
- [72] Fork, D. C. & Herbert, S. K. (1993). The Application of Photoacoustic Techniques to Studies of Photosynthesis. *Photochemistry and Photobiology*, 57, 207.
- [73] Cahen, D., Buchner, B., Decker, F., Wolf, M. (1990). Energy balance analysis of photovoltaic cells by voltage-dependent modulation photocalorimetry. *IEEE Transactions on Electron Devices*, 37(2), 498.

- [74] Coufal, H. (1990). Photothermal spectroscopy and its analytical application. *Fresenius' Journal of Analytical Chemistry*, 337(7), 835-842.
- [75] Skvortsov, L. A. (2013). Laser photothermal spectroscopy of light-induced absorption. *Quantum Electronics*, 43(1), 1.
- [76] Bialkowski, S. (1996). *Photothermal spectroscopy methods for chemical analysis* (Vol. 134). John Wiley & Sons.
- [77] Brusnichkin, A. V., Nedosekin, D. A., Proskurnin, M. A., & Zharov, V. P. (2007). Photothermal lens detection of gold nanoparticles: Theory and experiments. *Applied Spectroscopy*, 61(11), 1191-1201.
- [78] Snook, R. D., & Lowe, R. D. (1995). Thermal lens spectrometry. A review. *Analyst*, 120(8), 2051-2068.
- [79] Boccara, A. C., Jackson, W., Amer, N. M., & Fournier, D. (1980). Sensitive photothermal deflection technique for measuring absorption in optically thin media. *Optics Letters*, 5(9), 377-379.
- [80] Jackson, W. B., Amer, N. M., Boccara, A. C., & Fournier, D. (1981). Photothermal deflection spectroscopy and detection. *Applied Optics*, 20(8), 1333-1344.
- [81] Boyer, D., Tamarat, P., Maali, A., Lounis, B., & Orrit, M. (2002). Photothermal imaging of nanometer-sized metal particles among scatterers. *Science*, 297(5584), 1160-1163.
- [82] Gaiduk, A., Ruijgrok, P. V., Yorulmaz, M., & Orrit, M. (2010). Detection limits in photothermal microscopy. *Chemical Science*, 1(3), 343-350.
- [83] Li, Y., & Gupta, R. (2003). Detection of methane with high spatial resolution with photothermal deflection spectroscopy. *Applied Optics*, 42(21), 4396-4399.
- [84] Lu, S., Min, W., Chong, S., & Holtom, G. R. (2010). Label-free imaging of heme proteins with two-photon excited photothermal lens microscopy. *Applied Physics Letters*, 96(11), 113701-113701-3.
- [85] Shimosaka, T., Sugii, T., Hobo, T., Alexander Ross, J. B., & Uchiyama, K. (2000). Monitoring of dye adsorption phenomena at a silica glass/water interface with total internal reflection coupled with a thermal lens effect. *Analytical Chemistry*, 72(15), 3532-3538.
- [86] Horita, S., Miyagoshi, E., Ishimaru, M., & Hata, T. (1992). Improvement of sensitivity of photothermal deflection spectroscopy by a double pass method. *Review of Scientific Instruments*, 63(3), 1909-1913.

- [87] Schuessler, H. A., Chen, S. H., Rong, Z., Tang, Z. C., & Benck, E. C. (1992). Cavity-enhanced photothermal spectroscopy: dynamics, sensitivity, and spatial resolution. *Applied Optics*, 31(15), 2669-2677.
- [88] Barnes, J. R., Stephenson, R. J., Welland, M. E., Gerber, C., & Gimzewski, J. K. (1994). Photothermal spectroscopy with femtojoule sensitivity using a micromechanical device. *Nature*, 372, 79-81
- [89] Fan, S., & Joannopoulos, J. D. (2002). Analysis of guided resonances in photonic crystal slabs. *Physical Review B*, 65(23), 235112.
- [90] Wang, S. S., Moharam, M. G., Magnusson, R., & Bagby, J. S. (1990). Guided-mode resonances in planar dielectric-layer diffraction gratings. *JOSA A*, 7(8), 1470-1474.
- [91] Ding, Y., & Magnusson, R. (2004). Use of nondegenerate resonant leaky modes to fashion diverse optical spectra. *Optics Express*, 12(9), 1885-1891.
- [92] Uddin, M. J., & Magnusson, R. (2012). Efficient guided-mode-resonant tunable color filters. *IEEE Photonics Technology Letters*, 24(17), 1552-1554.
- [93] Wawro, D. D., Tibuleac, S., Magnusson, R., & Liu, H. (2000, May). Optical fiber endface biosensor based on resonances in dielectric waveguide gratings. In *BiOS 2000 The International Symposium on Biomedical Optics* (pp. 86-94). International Society for Optics and Photonics.
- [94] Cunningham, B., Li, P., Lin, B., & Pepper, J. (2002). Colorimetric resonant reflection as a direct biochemical assay technique. *Sensors and Actuators B: Chemical*, 81(2), 316-328.
- [95] Zhuo, Y., Hu, H., Chen, W., Lu, M., Tian, L., Yu, H., Long, K.D., Chow, E., King, W.P., Singamaneni, S. & Cunningham, B. T. (2014). Single nanoparticle detection using photonic crystal enhanced microscopy. *Analyst*, 139(5), 1007-1015.
- [96] Liu, J. N., Schulmerich, M. V., Bhargava, R., & Cunningham, B. T. (2014). Sculpting narrowband Fano resonances inherent in the large-area mid-infrared photonic crystal microresonators for spectroscopic imaging. *Optics Express*, 22(15), 18142-18158.
- [97] Chaudhery, V., George, S., Lu, M., Pokhriyal, A., & Cunningham, B. T. (2013). Nanostructured surfaces and detection instrumentation for photonic crystal enhanced fluorescence. *Sensors*, 13(5), 5561-5584.
- [98] Zhao, Y., Liu, K., McClelland, J., & Lu, M. (2014). Enhanced photoacoustic detection using photonic crystal substrate. *Applied Physics Letters*, 104(16), 161110.
- [99] Eustis, S., El-Sayed, M. A. (2006) Why gold nanoparticles are more precious than pretty gold: Noble metal surface plasmon resonance and its enhancement of the radiative

- and nonradiative properties of nanocrystals of different shapes. *The Royal Society of Chemistry*, 35, 209-217.
- [100] Plasmonic nanoparticles [Wikipedia entry]. Retrieved November 15, 2014, from https://en.wikipedia.org/wiki/Plasmonic_nanoparticles
- [101] Merkel, T. J., Herlihy, K. P., Nunes, J., Orgel, R. M., Rolland, J. P., & DeSimone, J. M. (2009). Scalable, shape-specific, top-down fabrication methods for the synthesis of engineered colloidal particles. *Langmuir*, 26(16), 13086-13096.
- [102] Martin, C. R. (1996). Membrane-based synthesis of nanomaterials. *Chemistry of Materials*, 8(8), 1739-1746.
- [103] Murphy, C. J., Sau, T. K., Gole, A., & Orendorff, C. J. (2005). Surfactant-directed synthesis and optical properties of one-dimensional plasmonic metallic nanostructures. *Mrs Bulletin*, 30(05), 349-355.
- [104] Turkevich, J., Stevenson, P. C., & Hillier, J. (1951). A study of the nucleation and growth processes in the synthesis of colloidal gold. *Discussions of the Faraday Society*, 11, 55-75.
- [105] Frens, G. (1973). Controlled nucleation for the regulation of the particle size in monodisperse gold suspensions. *Nature*, 241(105), 20-22.
- [106] Zhao, P., Li, N., & Astruc, D. (2013). State of the art in gold nanoparticle synthesis. *Coordination Chemistry Reviews*, 257(3), 638-665.
- [107] Giersig, M., & Mulvaney, P. (1993). Preparation of ordered colloid monolayers by electrophoretic deposition. *Langmuir*, 9(12), 3408-3413.
- [108] Govorov, A. O., & Richardson, H. H. (2007). Generating heat with metal nanoparticles. *Nano Today*, 2(1), 30-38.
- [109] Rosenzweig, A. (1980). *Photoacoustics and photoacoustic spectroscopy*. Wiley.
- [110] Ball, D. W. (2006). Photoacoustic spectroscopy. *SPECTROSCOPY-SPRINGFIELD THEN EUGENE THEN DULUTH*, 21(9), 14.
- [111] McClelland, J. F. (1983). Photoacoustic spectroscopy. *Analytical Chemistry*, 55(1), 89A-105A.
- [112] Zhang, H. F., Maslov, K., Stoica, G., & Wang, L. V. (2006). Functional photoacoustic microscopy for high-resolution and noninvasive in vivo imaging. *Nature Biotechnology*, 24(7), 848-851.

- [113] Miklós, A., Hess, P., & Boz ki, Z. (2001). Application of acoustic resonators in photoacoustic trace gas analysis and metrology. *Review of Scientific Instruments*, 72(4), 1937-1955.
- [114] Koskinen, V., Fonsen, J., Roth, K., & Kauppinen, J. (2008). Progress in cantilever enhanced photoacoustic spectroscopy. *Vibrational Spectroscopy*, 48(1), 16-21.
- [115] Hippler, M., Mohr, C., Keen, K. A., & McNaghten, E. D. (2010). Cavity-enhanced resonant photoacoustic spectroscopy with optical feedback cw diode lasers: A novel technique for ultratrace gas analysis and high-resolution spectroscopy. *The Journal of Chemical Physics*, 133(4), 044308.
- [116] Kachanov, A., Koulikov, S., & Tittel, F. K. (2013). Cavity-enhanced optical feedback-assisted photo-acoustic spectroscopy with a 10.4 μm external cavity quantum cascade laser. *Applied Physics B*, 110(1), 47-56.
- [117] Kosterev, A. A., Bakhrkin, Y. A., Curl, R. F., & Tittel, F. K. (2002). Quartz-enhanced photoacoustic spectroscopy. *Optics Letters*, 27(21), 1902-1904.
- [118] Lin, H., Yi, Z., & Hu, J. (2012). Double resonance 1-D photonic crystal cavities for single-molecule mid-infrared photothermal spectroscopy: theory and design. *Optics Letters*, 37(8), 1304-1306.
- [119] Wang, S. S., & Magnusson, R. (1993). Theory and applications of guided-mode resonance filters. *Applied Optics*, 32(14), 2606-2613.
- [120] Ding, Y., & Magnusson, R. (2004). Resonant leaky-mode spectral-band engineering and device applications. *Optics Express*, 12(23), 5661-5674.
- [121] Lecture 11 (EM21) – Guide-mode resonance. Retrieved March 2, 2014 from <https://www.youtube.com/watch?v=ZeSmxyTKkjg>
- [122] Neusch fer, D., Budach, W., Wanke, C., & Chibout, S. D. (2003). Evanescent resonator chips: a universal platform with superior sensitivity for fluorescence-based microarrays. *Biosensors and Bioelectronics*, 18(4), 489-497.
- [123] Lin, J. H., Tseng, C. Y., Lee, C. T., Kan, H. C., & Hsu, C. C. (2013). Guided-mode resonance enhanced excitation and extraction of two-photon photoluminescence in a resonant waveguide grating. *Optics Express*, 21(20), 24318-24325.
- [124] Pokhriyal, A. Lu, M. Huang, C. -S. Schulz, S. C. and Cunningham, B. T. (2010). External cavity laser biosensor arrangements *Applied Physics Letter*, 92(12), 121108.
- [125] Pokhriyal, A., Lu, M., Chaudhery, V., Huang, C. S., Schulz, S., & Cunningham, B. T. (2010). Photonic crystal enhanced fluorescence using a quartz substrate to reduce limits of detection. *Optics Express*, 18(24), 24793-24808.

- [126] Liu, J. N., Schulmerich, M. V., Bhargava, R., & Cunningham, B. T. (2011). Optimally designed narrowband guided-mode resonance reflectance filters for mid-infrared spectroscopy. *Optics Express*, 19(24), 24182-24197.
- [127] Zhao, Y., Cao, M., McClelland, J. F., Shao, Z., & Lu, M. (2016). A photoacoustic immunoassay for biomarker detection. *Biosensors and Bioelectronics*, 85, 261-266.
- [128] Zhao, Y., Huang, Y., McClelland, J. F., Zhao, X., & Lu, M. (2015, October). Photoacoustic immunoassay using plasmonic nanoparticles. In *Photonics Conference (IPC)*, 2015 (pp. 16-17). IEEE.
- [129] Tira, C., Tira, D., Simon, T., & Astilean, S. (2014). Finite-difference time-domain (FDTD) design of gold nanoparticle chains with specific surface plasmon resonance. *Journal of Molecular Structure*, 1072, 137-143.
- [130] Kleiner, G., Marcuzzi, A., Zanin, V., Monasta, L., & Zauli, G. (2013). Cytokine levels in the serum of healthy subjects. *Mediators of Inflammation*, 2013.
- [131] Urquidi, V., Chang, M., Dai, Y., Kim, J., Wolfson, E. D., Goodison, S., & Rosser, C. J. (2012). IL-8 as a urinary biomarker for the detection of bladder cancer. *BMC Urology*, 12(1), 12.
- [132] Tam, A. C. (1986). Applications of photoacoustic sensing techniques. *Reviews of Modern Physics*, 58(2), 381.
- [133] Posthuma-Trumpie, J. F., & Kniseley, R. N. (1976). Photoacoustic spectroscopy with condensed samples. *Applied Optics*, 15(11), 2658-2663.
- [134] Mallidi, S., Larson, T., Tam, J., Joshi, P. P., Karpouk, A., Sokolov, K., & Emelianov, S. (2009). Multiwavelength photoacoustic imaging and plasmon resonance coupling of gold nanoparticles for selective detection of cancer. *Nano Letters*, 9(8), 2825-2831.
- [135] Zhang, Q., Iwakuma, N., Sharma, P., Moudgil, B. M., Wu, C., McNeill, J., Jiang, H. & Grobmyer, S. R. (2009). Gold nanoparticles as a contrast agent for in vivo tumor imaging with photoacoustic tomography. *Nanotechnology*, 20(39), 395102.
- [136] Parolo, C., & Merkoç, A. (2013). Paper-based nanobiosensors for diagnostics. *Chemical Society Reviews*, 42(2), 450-457.
- [137] Castleden, S. L., Elliott, C. M., Kirkbright, G. F., & Spillane, D. E. M. (1979). Quantitative examination of thin-layer chromatography plates by photoacoustic spectroscopy. *Analytical Chemistry*, 51(13), 2152-2153.

- [138] White, R. L. (1985). Analysis of thin-layer chromatographic adsorbates by Fourier transform infrared photoacoustic spectroscopy. *Analytical Chemistry*, 57(9), 1819-1822.
- [139] Jarvis, J. N., Percival, A., Bauman, S., Pelfrey, J., Meintjes, G., Williams, G. N., Longley, N., Harrison, T.S. & Kozel, T. R. (2011). Evaluation of a novel point-of-care cryptococcal antigen test on serum, plasma, and urine from patients with HIV-associated cryptococcal meningitis. *Clinical Infectious Diseases*, cir613.
- [140] Martinez, A. W., Phillips, S. T., Whitesides, G. M., & Carrilho, E. (2009). Diagnostics for the developing world: microfluidic paper-based analytical devices.
- [141] Pardee, K., Green, A. A., Ferrante, T., Cameron, D. E., DaleyKeyser, A., Yin, P., & Collins, J. J. (2014). Paper-based synthetic gene networks. *Cell*, 159(4), 940-954.
- [142] Lu, M., Choi, S. S., Irfan, U., & Cunningham, B. T. (2008). Plastic distributed feedback laser biosensor. *Applied Physics Letters*, 93(11), 111113.
- [143] Zhao, Y., Liu, L., Zhao, X., & Lu, M. (2016). Enhanced photothermal lens using a photonic crystal surface. *Applied Physics Letters*, 109(7), 071108.
- [144] Block, I. D., Ganesh, N., Lu, M., & Cunningham, B. T. (2008). A sensitivity model for predicting photonic crystal biosensor performance. *IEEE Sensors Journal*, 8(3), 274-280.

ACKNOWLEDGMENTS

The completion of this undertaking could not have been possible without the participation and assistance of so many people whose names may not all be enumerated. Their contributions are sincerely appreciated and gratefully acknowledged. However, I would like to express my deep appreciation and indebtedness particularly to the following:

Dr. Meng Lu, my major professor, whose wise advice and endless support, kind and understanding spirit ensured the success and achievement of my work.

Dr. John F. McClelland, who provided invaluable assets and guidance for my research.

Dr. Wai Leung, who provided support, offered training and advice at Microelectronics Research Center.

To all my committee members, all group members of the Laboratory of Integrated Optical Sensors, relatives, friends and others who in one way or another shared their support, thank you.

Thanks for all your encouragement!